ABSOLUTE FLUX DENSITY MEASUREMENTS AT 111 MHZ.

A thesis submitted for the degree
of Master of Science
at the University of Sydney
by A.G.Wilson.

PREFACE

This thesis describes the measurement of the absolute flux densities for seven discrete radiosources at 111 MHz.

The radiosource observations were made at the Molonglo Radioastronomy Observatory which is operated by the Astrophysics Department of the School of Physics within the University of Sydney.

The work for the thesis was carried out from 1973 to 1976 inclusively.

I wish to thank my supervisor Professor B.Y.Mills for discussion concerning the overall direction of the experiment. I am indebted to Professor A.G.Little for many useful discussions concerning the setting up of the observing equipment and the overcoming of instrumental problems affecting the flux density measurements.

I was responsible for a major part in the selection of the particular variation upon the Little/Wyllie absolute flux density measurement method used and the setting up of the observing equipment. I was responsible for the detailed investigation of the observing equipment to locate departures from assumed behaviour.

I was completely responsible for the design of the observing procedure and data analysis. The observations were planned, executed and reduced solely by myself.

I was primarily responsible for the thermal calibration methods applied to the secondary noise temperature reference.

The Molonglo Radioastronomy Observatory is supported by the Australian Research Grants Committee, the Sydney University Research Grants Committee and the Science Foundation for Physics within the University of Sydney.

April 1977.

CONTENTS.

Page

Page

Page

Page

LIST OF FIGURES.

CHAPTER 1.

INTRODUCTION .

1.1 Prolegomena.

This thesis describes the absolute flux density measurements at 111 MHz made on seven sources PKS 0531+21, 0624-05, 0915-11, 1228+12, 1648+05, 1932-46 and 2211-17. The method used represents a slight variation on that used initially by Little (1958) at 85.5 MHz and Wyllie (1969a) at 408 MHz. The observations were made in conjunction with the East-West aerial of the Molonglo radiotelescope at Hoskinstown, N.S.W.

1.2 Absolute Flux Density Calibration Methods.

Wyllie (1968) presented a detailed review of absolute flux density measurement methods. The accuracy, limitations and suitability of existing techniques in the low, medium and high frequency ranges were discussed by Wyllie.

The absolute flux density experiments were grouped into three classifications.

A. Experiments using directly low gain standard antennas.

B. Experiments where a large aerial whose properties cannot be accurately directly calculated is calibrated by one of the following methods.

B.1 The use of a standard antenna. The aerial may be calibrated, using the standard antenna, by the simultaneous observation of a discrete radiosource sufficiently strong to be observed by the standard antenna. Alternatively, the powers received

by the standard antenna and the aerial under calibration from a transmitter on a testing range or suspended in the air may be compared.

B.2 The black disk method. The gain of the aerial is determined by observing the radiation from a black disk of known temperature placed in the main beam of the aerial.

B.3 Polar diagram integration.

C. Experiments based upon the Little (1958) experiment.

A fourth classification is the calibration of large very low frequency dipole arrays by a combination of theoretical calculation of far-field power patterns, careful consideration of and measurement of the various sources of loss within the array and adjustment of the theoretical array model parameters to fit the observed power pattern.

The essential feature of experiments based upon the Little (1958) absolute flux calibration at 85.5 MHz is the employment of a low gain aerial of known gain in combination with a much larger collecting area aerial or aerials of unknown gains.

Wyllie (1969a) details two variations upon Little's experiment. In the first variation, termed Wyllie method I, two large aerials are used together with the reference aerial in three interferometer pairs. In Wyllie method II an interferometer record using a large aerial and the reference aerial is taken

simultaneously with the large aerial's total power record.

For both Wyllie methods the recorded radiosource deflections are combined algebraically to express the absolute flux density of the source as a function of the collecting area of the reference aerial, the noise temperature of a calibration signal and calibration factors describing specified losses in the reference aerial and the receiving system. The unknown collecting areas of the large aerials are eliminated from the expression for the source's absolute flux density.

At 111 MHz the use of the Little/Wyllie method in conjunction with the East-West arm of the Molonglo radiotelescope for the measurement of absolute flux densities has considerable advantages over experiments using only standard low gain antennas in interferometer pairs or total power observation.

Measurements obtained by direct observation with standard low gain antennas are restricted to the strongest discrete sources, usually Cassiopeia A, Cygnus A and Taurus A. The use of very strong sources as calibration sources is unsatisfactory (Kellermann 1964a) for several reasons. Receiver non-linearity introduces inaccuracy to the measurement of the flux density ratios of the majority of sources relative to the very large flux densities of Cas A and Cyg A or alternatively, accurately known attenuators must be available. Further disadvantages of Cas A, Cyg A and Tau A are their angular sizes, the location of the sources near the galactic plane and the decrease with time of the flux density of Cas A. Only having a very low number of absolute flux density calibration sources increases the

possibility of systematic error in the flux density scale. Cas A and Cyg A are located too far north to be useful as flux density reference sources for relative measurements made in the southern hemisphere.

The advantages of absolute flux density measurements based upon the Little/Wyllie method are :-

a. The combination of a large aerial with the low gain reference aerial results in an improvement in sensitivity over methods involving the separate use of low gain antennas. The Little/Wyllie method enables flux density calibration sources to be selected having flux densities considerably lower than those of the very strong sources Cas A, Cyg A and Tau A.

b. The narrow beam provided by the large aerial reduces the effects of confusion due to irregularities in the galactic background and the presence of other discrete sources.

1.3 Organization of the Thesis.

Chapter 2 describes the East-West aerial of the Molonglo radiotelescope. Chapter 3 deals with the theory of the absolute flux density measurement technique used at 111 MHz and contains a description of the receiving system used for the flux density measurements.

The determination of the reference aerial's collecting area is discussed in Chapter 4. Chapter 5 details the methods used for

the thermal calibration of the receiving system's calibration noise signal.

Chapter 6 discusses the testing and checks of the receiving equipment, the origin and evaluation of instrumental corrections to the theory presented in Chapter 3. Details are provided on the selection of and partial resolution corrections applied to the flux density calibration sources, the observing and data reduction procedures and a discussion of confusion errors.

Chapter 7 deals with the problems present in obtaining relative flux density measurements between the absolute flux density calibration sources.

Chapter 8 discusses the absolute and relative flux density measurements. A comparison is made between the observed 111 MHz Molonglo absolute flux densities and the flux densities interpolated from spectra constructed in accordance with the low frequency flux density scale revision by Roger, Costain and Bridle (1973). A comparison is made also with flux densities on the scales of Conway, Kellermann and Long (1963), Kellermann (1964b) and Kellermann, Pauliny-Toth and Williams (1969).

CHAPTER 2.

THE 111.2 MHZ RADIOTELESCOPE.

2.1 The Aerials.

The East-West arm of the Molonglo Cross radiotelescope was designed to operate at two frequencies, 408 MHz and 111 MHz. The North-South arm of the Cross operates at the single frequency of 408 MHz. The design of the Cross at 408 MHz is given in detail by Mills et al (1963). The final form of the 111 MHz receiving system differs considerably from the projected design given by Mills et al. The planned design was to equip both the North-South and East-West arms with feed dipoles at 111 MHz to form a cross-type telescope at 111 MHz. The final system adopted uses only the East-West arm for 111 MHz reception. The East-West arm usually operates as a total power telescope at 111 MHz.

The East-West arm consists of two aerials. The aerials may operate jointly to form a 4.3 by 583 wavelengths cylindrical parabola at 111.2 MHz having a central gap of 4.7 wavelengths to allow the North-South arm of the Molonglo Cross to pass unbroken through the central intersection of the Cross.

A fan beam of half-power beamwidths of 5.5 min arc in right ascension and 23 degrees in declination is produced at 111.2 MHz. The telescope operates as a meridian transit instrument. The beam is moved in declination by mechanically tilting the East-West arm about its long axis. The driving rate of declination change is five degrees per minute. The declination coverage is + 19 to - 90 degrees.

Alternatively, the Eastern and Western arms may operate

independently as two separate aerials each of dimensions 4.3 by 289 wavelengths.

The East-West arm is constructed of modules 8.8 meters long (3.3 wavelengths at 111.2 MHz). The reflecting surface consists of continuous wire mesh. Each half aerial of the East-West arm consists of 88 modules.

2.2 The Feed.

The East-West aerial feed positioned along the line focus of the cylindrical parabola is similarly divided into 176 modules. Each module is rectangular in cross-section and forms resonant waveguide sections for the 408 MHz feed system. The 408 MHz half-wave feed dipoles are mounted on the plane reflecting surface of the feed module facing the mesh surface.

At 111 MHz half-wave folded dipoles are mounted on the outer face of the 408 MHz waveguide (i.e facing away from the mesh surface). The 111 MHz feed dipoles are polarized in the North-South direction. Six dipoles are employed per module, fed by a loaded twin wire line. The North-South width of the 408 MHz waveguide is 0.18 wavelengths at 111.2 MHz.

2.3 The R.F System.

The modules for the Eastern and Western arms are numbered from number one at the central intersection outwards to number eighty-eight at the Eastern and Western extremities of the East-West arm.

Figs 2.1 and 2.2 (adapted from diagrams by A.G.Little) show the manner by which the 111 MHz feed modules are interconnected. For modules 1 to 32 inclusive and 33 to 64 inclusive of both the Eastern and Western arms the interconnecting arrangement is given

in Fig 2.1. Commencing from module number 1 the signals from four consecutive modules are combined in phase by a four-way addition hybrid, followed by a pre-amplifier as diagramatically depicted. The 111 MHz pre-amplifier gain is 30 dB, bandwidth 9 MHz with a noise figure of 1 dB. Eight pre-amplifier outputs are formed per 32 modules. The set of 8 outputs is divided into two sets of 4 outputs, each of which is combined again by a four-way addition hybrid. The two resulting outputs are added in a two-way hybrid to form one output per 32 modules.

Fig 2.2 displays the interconnecting arrangement for feed modules 65 to 88 inclusive for both the Eastern and Western arms. The diagram is self-evident. Cable lengths of corresponding interconnections have the same values.

Thus the East-West arm is divided into six sections i.e four inner sections each with 32 modules and two extreme sections of 24 modules. The sections are identified by the numbering system in Table 2.1 and are shown in Fig 2.3.

Table 2.1

East-West Arm Section Identification System.

Module Numbers	Section Name	
	East Arm	West Arm
1 to 32	17 E	17 W
33 to 64	49E	49 W
65 to 88	81 E	81 W

The R.F system following the two-way hybrid is the same for all six aerial sections. The succeeding stages are image filter and converter. The local oscillator frequency is 116.77 MHz. The I.F signal then proceeds by a 0.8 kilometre cable to a building, called the phasing hut, located near the centre of the Molonglo Cross.

Fig 2.4 shows the local oscillator system. The output from the crystal oscillator is amplified, divided by a two-way hybrid and distributed by equal length cables to amplifiers located at the 49 E and 49W aerial sections. The output of each amplifier is split three ways and connected through high-pass filters to the three converters located on each of the Eastern and Western arms respectively.

The local oscillator signal supplied to the Eastern arm is maintained in phase to that supplied to the Western arm by the use of reference cables. These cables take the local oscillator signals obtained from couplers on the local oscillator inputs to the 17 E and 17 W sections to a central location where the Eastern signal is phase-switched against the Western signal. The D.C output from the phase sensitive detector is used as an error signal to control a phase-shifter located on the input to the 49 E local oscillator amplifier.

2.4 The I.F System.

In the phasing hut the I.F cables from the six aerial sections connect to phase shift and gain control units (low gain).

The controls to the low gain amplifiers are located in the control room.

A combining unit adds in phase the I.F outputs from the six phase and gain control units. The combiner output proceeds by shielded cable across to the control room to an amplifier of central frequency 5.60 MHz and 0.2 MHz bandwidth, followed by a total power detector.

2.5 Aerial Section Phasing.

The mutual phasing of the six aerial sections is carried out by forming phase-switched interferometer pairs between the six aerial sections where each pair contains a common aerial section which forms the phase reference (A.G.Little private communication). Observation of a strong small diameter source, 0915-11 is the only suitable source, allows the relative phasing of the aerial sections to be determined. Appropriate phase adjustments are then made to correct the relative phasing errors.

Abbreviations for Figs. 2.1 and 2.2 .

C : Converter.

H : Addition Hybrid.

HP : High Pass Filter.

IM : Image Filter.

LO : Local Oscillator.

P : Pre-amplifier.

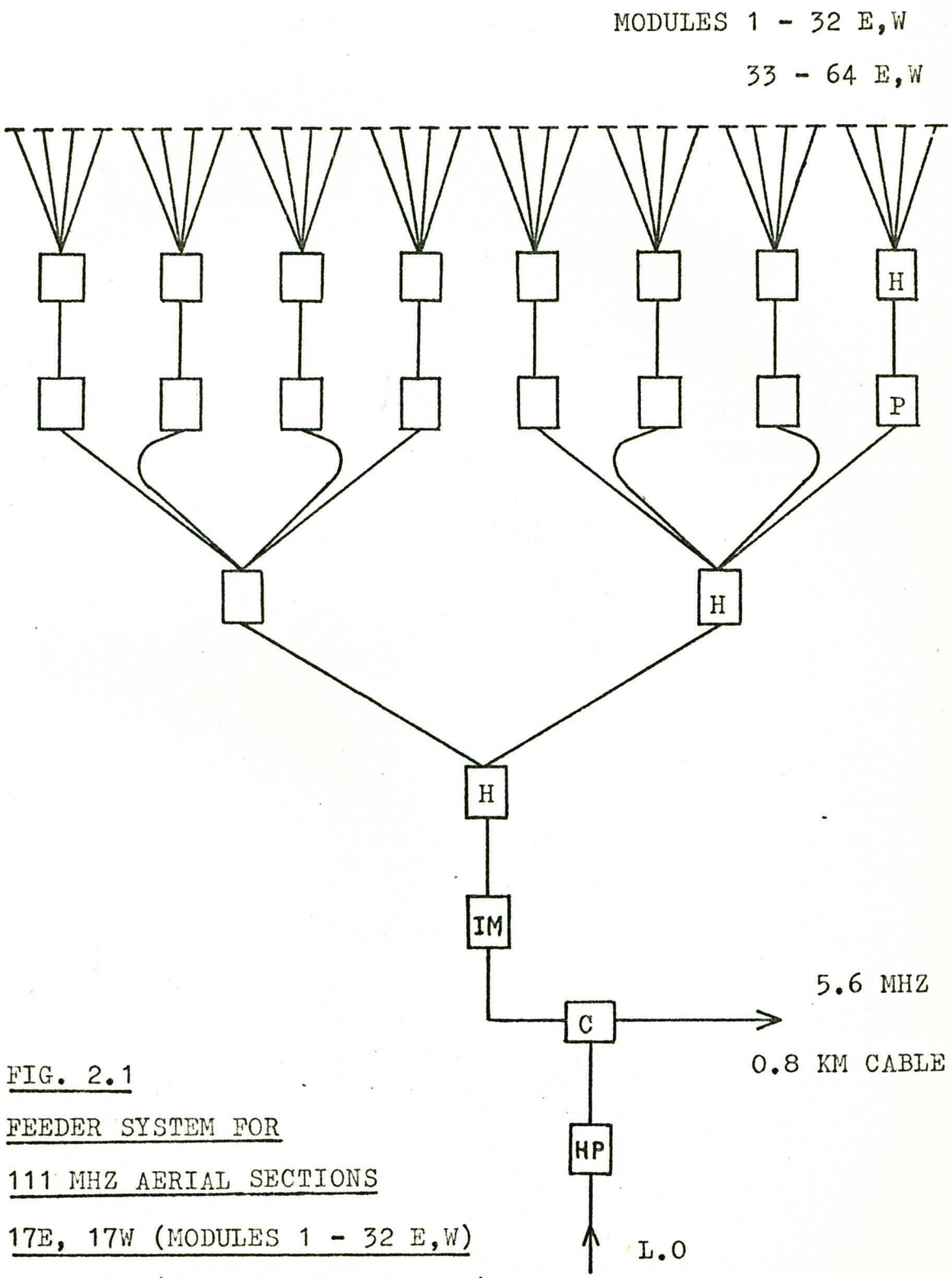

FIG. 2.1

FEEDER SYSTEM FOR

111 MHZ AERIAL SECTIONS

17E, 17W (MODULES 1 - 32 E,W)

49E, 49W (MODULES 33 - 64 E,W)

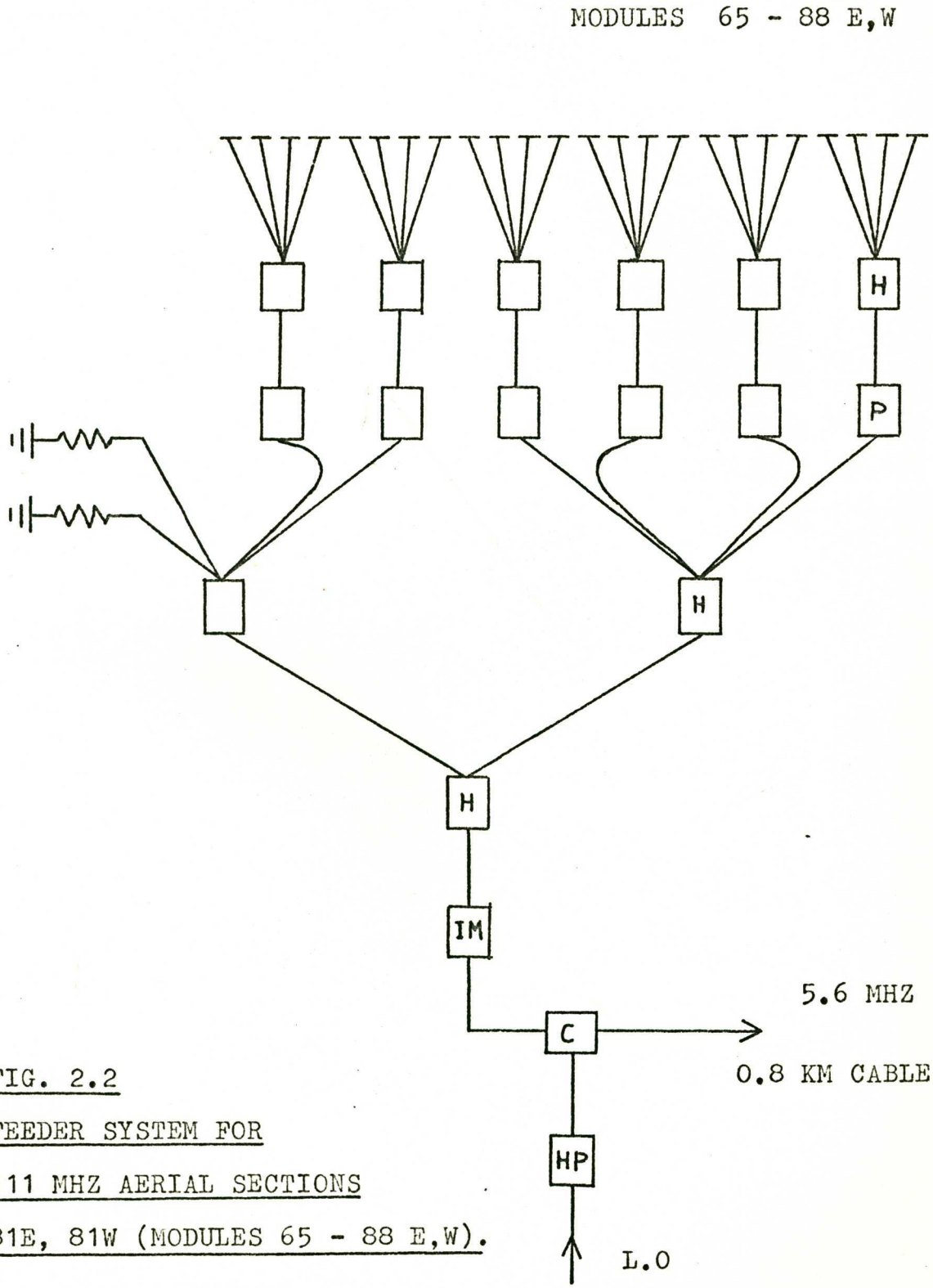

FIG. 2.2

FEEDER SYSTEM FOR

111 MHZ AERIAL SECTIONS

81E, 81W (MODULES 65 - 88 E,W).

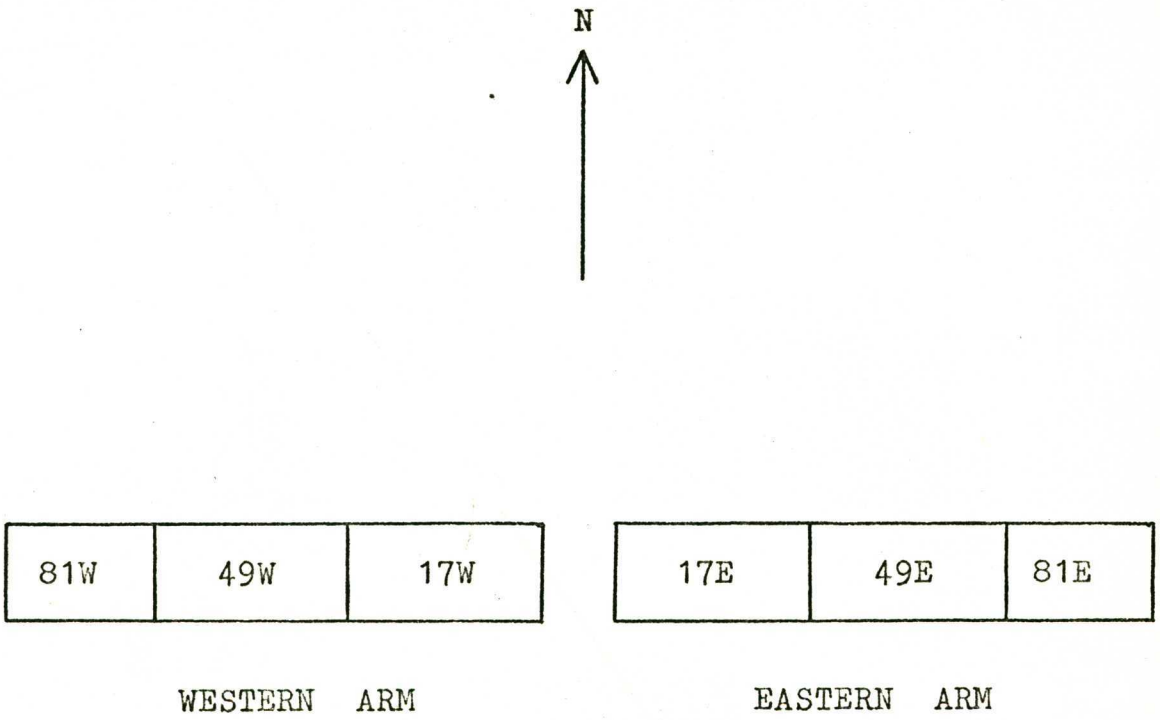

FIG. 2.3 . DIVISION OF THE EAST-WEST ARM OF THE MOLONGLO CROSS AT 111.2 MHZ.

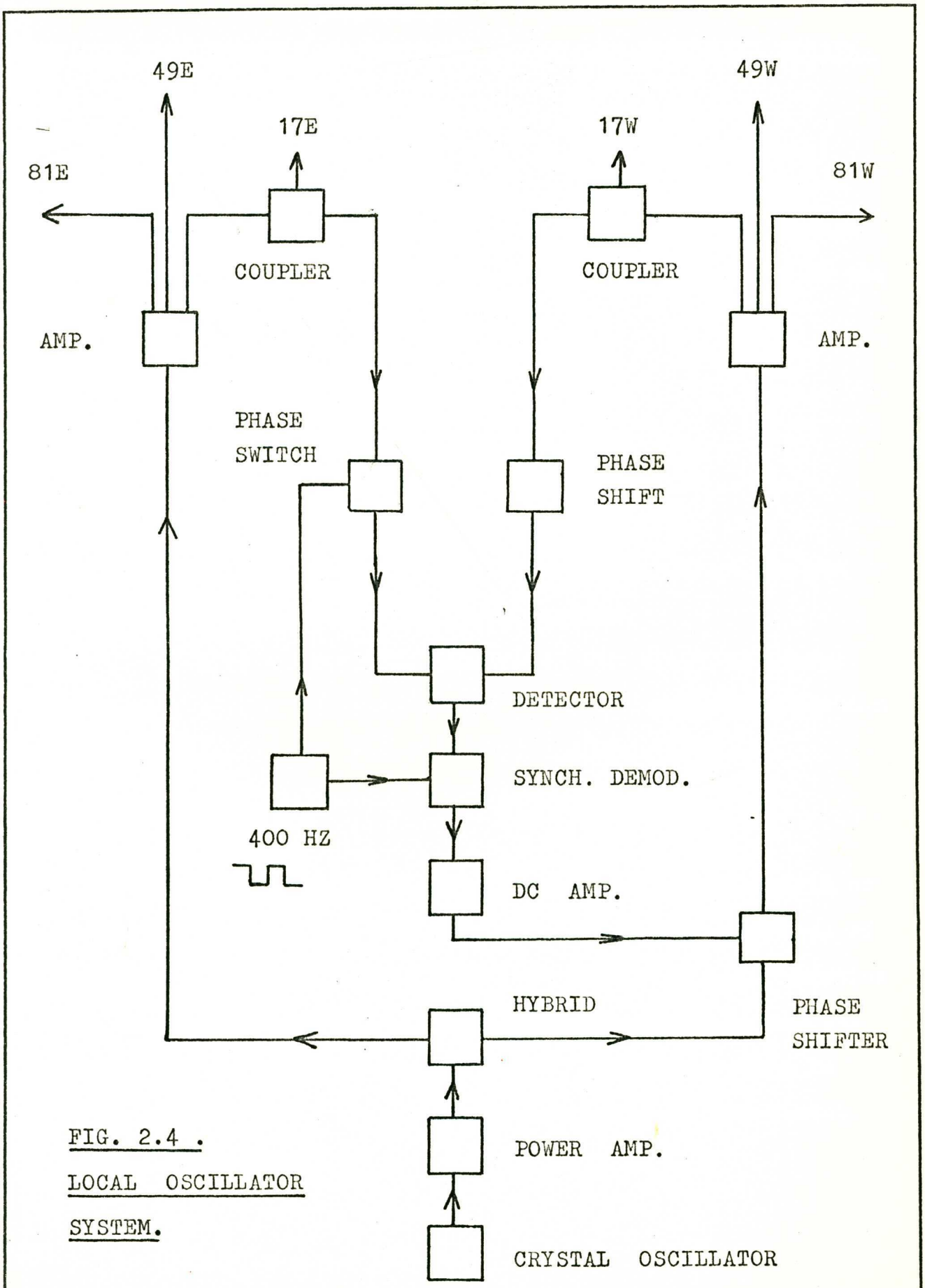

FIG. 2.4 .
LOCAL OSCILLATOR
SYSTEM.

CHAPTER 3.

ABSOLUTE FLUX DENSITY MEASUREMENT METHOD AND RECEIVING SYSTEM.

3.1 Elementary Definitions.

Consider a randomly polarized, non-extended radiosource under observation by a linearly polarized aerial. The change in available power at the receiver, denoted by ΔP_A, due to the radiosource is given by (Findlay 1966)

$$(1) \qquad \Delta P_A = \frac{1}{2} \int_0^\infty A(v)S(v)B(v)dv$$

where $A(v)$ = the effective area of the aerial in the direction of the source.

$S(v)$ = the flux density of the observed source.

$B(v)$ = the normalized bandwidth response function of the receiving system.

v = the observing frequency.

The 111.2 MHz receiving system has a maximun bandwidth of 0.300 MHz. Both S(v) and A(v) are slowly varying functions of frequency across the bandwidth. Consequently the approximation is made that A(v) and S(v) are treated as constant across the receiving system bandwidth. The factor of 1/2 appearing in equation (1) is due to the linear polarization of the aerial.

Rewrite equation (1)

$$(2) \qquad \Delta P_A = \frac{1}{2} A.S \int_0^\infty B(v)dv$$

where A and S are the average values of A(v) and S(v) respectively over the receiver bandwidth.

The thermal noise power per unit bandwidth, denoted by P, available from a resistor at temperature T^{o} K is given by Nyquist's formula,

$$P = k.T \tag{3}$$

where k is Boltzmann's constant.

The change in available power, denoted by ΔP_R, at the receiver terminals due to a temperature change ΔT in a resistor replacing the aerial at the input to the radiometer is given by,

$$\Delta P_R = k.\Delta T \int_0^\infty B(v)dv \tag{4}$$

Equations (2) and (4) then provide the following expression for S,

$$S = 2.k.\frac{\Delta T}{A} . \frac{\Delta P_R}{\Delta P_R} \tag{5}$$

3.2 Description of the Receiving System.

3.2.a General Description.

Both Wyllie methods I and II are applicable to the 111.2 MHz radiotelescope. Method II was selected in preference to method I for the following reasons.

The dominant reason was the sensitivity improvement of method II over method I. Preliminary observations, employing both methods I and II indicated that method II would permit accurate absolute flux density measurements to a lower flux density limit of approximately 100 Jy*. A second reason, of lesser importance, is that method II is instrumentally simpler in comparison to method I. Three output channels are required for method II, as opposed to six output channels required for method I. The post-observation data reduction is correspondently halved.

The reference aerial used for the 111 MHz absolute flux measurements was a horizontal half-wave dipole, polarized in the North-South direction, located 0.169 wavelengths above a highly conducting metallic sheet and wire mesh ground plane. The reference aerial was positioned 9.28 wavelengths West and 12.89 wavelengths North of the central intersection of the Molonglo Cross.

The 111.2 MHz absolute flux density measurement receiving system is shown in block diagram form in Figs 3.1, 3.2 and 3.3.

The receiving system operates in two modes. During source observation the reference aerial output voltage is multiplied against the East-West aerial's output voltage. The cosine

* 1 Jansky (Jy) = 10^{-26} W $m^{-2}Hz^{-1}$.

(phase difference θ) and the sine (phase difference $\theta + 90^{\circ}$) interferometer output components are recorded, together with the East-West aerial's total power output.

The receiving system is calibrated by the replacement of the reference aerial by a calibrated diode noise source. Part of the calibration signal is injected into the East-West aerial signal path enabling both total power and multiplier calibration deflections to be produced.

3.2.b The Reference Aerial Section.

Fig.3.2 shows the reference aerial equipment. The coaxial switch, remotely controlled from the control room, allows either the reference aerial or the calibration diode noise source to connect to the pre-amplifier input. The stages succeeding the coaxial switch were designed to be very similar to the corresponding R.F and I.F sections of the East-West aerial radiotelescope.

Stages following the pre-amplifier are 147 metres of cable, image filter, converter and 0.8 kilometres of I.F cable terminating in the phasing hut. The reference aerial section cable lengths had nearly the same values as for the East-West aerial in order to reduce to low significance the loss of correlation in the interferometer responses due to the bandwidth " fringe washing " function (Christiansen and Högbom 1969).

The length of the local oscillator cable to the reference aerial converter had a value close to the corresponding length in the East-West aerial system.

3.2.c The I.F System.

The I.F signal from the reference aerial converter connects to a 0/180 degrees phase switch in the phasing hut. Next follows a low gain phase and gain control unit identical to those units employed on the phasing hut I.F inputs from the six East-West aerial sections. The gain is remotely adjustable from the control room. The succeeding stage is an I.F amplifier of gain 26 dB, central frequency 5.60 MHz and 0.30 MHz bandwidth. The I.F amplifier output is split by a two-way ferrite-core hybrid (labelled hybrid 4 in Fig.3.1).

In the source observation receiving system mode one output of hybrid 4 connects to a matched termination (68 ohm). The other hybrid 4 output is further divided by another two-way hybrid (labelled hybrid 5). A 90 degrees phase delay is located on one of the hybrid 5 outputs resulting in the formation of two signals from the reference aerial section differing in phase by 90 degrees.

The output from the East-West aerial sections I.F combining unit connects to an I.F amplifier of the same design as the 26 dB amplifier located in the reference aerial's signal path following the phase switch. The next stage is a low gain amplifier. The gain of this amplifier is remotely adjustable from the control room. The amplifier output is divided by a hybrid having two inputs and two outputs (labelled hybrid 1). In the observing mode the unused input is terminated by a 68 ohm resistor.

One output from hybrid 1 connects across via shielded cable

to the total power signal path I.F amplifier, square-law detector, D.C balance and amplifier. The control room I.F amplifier has bandpass 0.200 MHz and was aligned on the central frequency of 5.60 MHz. The amplifier has course and fine gain controls. The total power output time constant was 1 second.

The other output of hybrid 1 was divided by hybrid 2.

The two reference aerial section and the two East-West aerial I.F outputs formed by hybrids 2 and 5 connect across to the control room. In the control room each output connects to an I.F gain adjustment unit to form the inputs to the cosine and sine multipliers.

The two multipliers are usually employed in the 408 MHz Molonglo Cross receiving system. The input levels to the multipliers may be monitored in the control room to ensure that the levels present in the 111.2 MHz flux density measurements, for both source observation and calibration, were close to the usual operating values for the multipliers.

The multipliers function on a combination of radiofrequency multiplication and phase switching. For each multiplier the phase switched reference aerial section signal and the East-West aerial signal are applied simultaneously but in opposite phases to the inputs of two square-law detectors. The difference between the outputs of the two detectors is a modulated signal proportional to the product of the two voltages.

The output of each multiplier connects to a synchronous demodulator followed by a low pass filter-amplifier. The output time constant for the interferometer outputs was 3 seconds.

The total power, cosine and sine multiplier outputs were recorded on a Rikadenki chart recorder.

3.2.d The Calibration System Mode.

The output signal path of hybrid 4 not connected to hybrid 5 is divided by hybrid 3. A 90 degrees phase delay was located on one of hybrid 3's outputs. In the observe system mode both outputs of hybrid 3 are terminated by 68 ohm loads.

During the receiver system calibration the 68 ohm load connected to the hybrid 1 input for the observe mode is disconnected and replaced by an output from hybrid 3 thus forming a path for the calibration signal from hybrid 4 to hybrid 1. The calibration signal divides in hybrid 1 and proceeds to the total power receiving system and to the East-West aerial sides of the cosine and sine multipliers to multiply against itself to produce the interferometer calibration deflections. The output of hybrid 3 not connected to hybrid 1 was always terminated by a 68 ohm load.

The case of the output of hybrid 4 connected to hybrid 1 through the hybrid 3 output not containing the additional 90 degrees phase delay is termed the CAL-I system mode.

The case where the additional 90 degrees phase delay is inserted into the signal path between hybrids 1 and 4 is termed the CAL-II system mode.

The locations of the switches labelled A,B,C,D and E are shown in Fig.3.1. Table 3.1 presents the status of the above-mentioned switches for the observe, CAL-I and CAL-II receiving system modes.

Table 3.1

System Switch Positions.

System Mode	Switch Positions	
	Open	Closed
Observe	B, C	A, D, E
CAL-I	A, C, E	B, D
CAL-II	B, D, E	A, C

The symbols listed in Table 3.2 are gain factors describing the receiving system between the system locations given. The gain factors include both losses and gains e.g cable losses, conversion losses and amplifier gains.

Table 3.2

Gain Factor Symbol Identification.

Symbol	Section of Receiving System Described.	
	Beginning Location	End Location
G_1	Coaxial switch output	Input to hybrid 4
G_2	East-West aerial combiner output	Input to hybrid 1
α	Output of hybrid 1 leading to hybrid 2	East-West aerial input to the sine multiplier

Table 3.2 continued.

Symbol	Beginning Location	End Location
β	Output of hybrid 1 leading to hybrid 2	East-West aerial input to the cosine multiplier
γ	Input to hybrid 4	Reference aerial input to the cosine multiplier
δ	" " " "	Reference aerial input to the sine multiplier
η_1	East-West input to hybrid 1	Total power output of hybrid 1 (measured for the observe system mode)
η_2	" " " " "	Output of hybrid 1 leading to hybrid 2 (measured for the observe system mode)
η_{3I}	Hybrid 3 input to hybrid 1	Output of hybrid 1 leading to hybrid 2 (measured for the CAL-I system mode)
η_{3II}	" " " " " "	Output of hybrid 1 leading to hybrid 2 (measured for the CAL-II system mode)

Table 3.2 continued.

Symbol	Beginning Location	End Location
η_{4I}	Hybrid 3 input to hybrid 1	Total power output of hybrid 1 (measured for the CAL-I system mode)
η_{4II}	" " " " " "	Total power output of hybrid 1 (measured for the CAL-II system mode)
ϵ_I	Input to hybrid 4	Hybrid 3 input to hybrid 1 (measured for the CAL-I system mode)
ϵ_{II}	" " " "	Hybrid 3 input to hybrid 1 (measured for the CAL-II system mode)
g_T	Total power output of hybrid 1	Total power chart recorder output
g_C	Inputs to the cosine multiplier	Cosine multiplier chart recorder output
g_S	Inputs to the sine multiplier	Sine multiplier chart recorder output

3.3 Theory of the Absolute Flux Density Measurement Method.

Consider the case of a randomly polarized non-extended source of flux density S transiting the meridian. The receiving system is assummed to be in the observe mode. The resulting total power record source deflection is given by

$$D_1 = \left(\frac{S A_{EW}}{2}\right) G_2 \cdot \eta_1 \cdot g_T \qquad (6)$$

where A_{EW} is the effective area of the East-West aerial of the Molonglo Cross at 111.2 MHz in the direction of the source.

The phase switched multiplying interferometer's cosine and sine recorder source deflections are given by

$$D_2 = g_c \cdot \left(\frac{S A_{EW}}{2} \cdot G_2 \cdot \eta_2 \cdot \beta\right)^{1/2} \cdot \left(\frac{S A_R}{2} \cdot G_1 \cdot \gamma\right)^{1/2} \cdot \cos\theta$$

$$D_3 = g_s \cdot \left(\frac{S A_{EW}}{2} \cdot G_2 \cdot \eta_2 \cdot \alpha\right)^{1/2} \cdot \left(\frac{S A_R}{2} \cdot G_1 \cdot \delta\right)^{1/2} \cdot \sin\theta \qquad (7)$$

where A_R is the effective area of the reference aerial in the direction of the source and θ is the phase angle between the East-West aerial and the reference aerial I.F source voltages at the location of signal multiplication (at the cosine multiplier).

For the receiving system in the CAL-I and CAL-II modes the reference aerial is remotely replaced by a saturated diode noise source.

A common location for the reference aerial and calibration

noise source output voltages is the output of the coaxial switch. Losses from the output of the coaxial switch through the reference aerial side of the coaxial switch and in the cable connecting the input of the coaxial switch to the reference aerial half-wave dipole are treated as losses in the reference aerial.

Similarly, losses from the output of the coaxial switch back through the coaxial switch to the diode noise source are treated as losses associated with the calibration noise source.

The calibration noise temperature is the excess noise temperature above when the noise diode source is not operating. The calibration signal obtained from the noise diode is 100 percent modulated at the phase switching frequency. The noise temperature T is the equivalent noise temperature of the noise diode signal measured at the output of the coaxial switch.

In the case of the receiving system set in the CAL-I mode the total power calibration deflection is given by

$$D_{1cal} = \frac{k.T}{2} \cdot G_1 \cdot \epsilon_I \cdot \eta_{4I} \cdot g_T \tag{8}$$

The cosine and sine chart recorder calibration deflections are given by

$$D_{2cal} = \frac{g_c}{2} \cdot \left(k.T.G_1.\epsilon_I.\eta_{3I}.\beta\right)^{1/2} \cdot \left(k.T.G_1.\gamma\right)^{1/2} \cdot \cos\phi \tag{9}$$

$$D_{3cal} = \frac{g_s}{2} \cdot \left(k.T.G_1.\epsilon_I.\eta_{3I}.\alpha\right)^{1/2} \cdot \left(k.T.G_1.\delta\right)^{1/2} \cdot \sin\phi$$

The factor of 1/2 arises from the 100 percent modulation of the diode noise source signal, ϕ is the phase angle difference between the two calibration signals at the location of signal multiplication for the cosine multiplier, k is Boltzmann's constant.

In the case of the receiving system set in the CAL-II mode the total power chart recorder calibration deflection is given by

$$D_{4cal} = \frac{kT}{2} \cdot G_1 \cdot \epsilon_{II} \cdot \eta_{4II} \cdot g_T \tag{10}$$

The cosine and sine chart recorder calibration deflections are given by

$$D_{5cal} = \frac{g_s}{2} \left(kT G_1 \epsilon_{II} \eta_{3_{II}} \alpha\right)^{1/2} \cdot \left(kT G_1 \delta\right)^{1/2} \cos\phi$$

$$D_{6cal} = \frac{g_c}{2} \left(k.T.G. \epsilon_{II} \cdot \eta_{3II} \beta\right)^{1/2} \cdot \left(kT G_1 \gamma\right)^{1/2} \sin\phi \tag{11}$$

The above set of equations provide the following expression for the source flux density

$$S = \frac{\left(D_2^2 + D.D_3^2\right). D_{ical} . kT}{\left(D_{2cal}^2 + D.D_{3cal}^2\right) \cdot D_1 \cdot A_R} \cdot \left(\frac{\eta_1}{\eta_2}\right) \cdot \left(\frac{\eta_{3I}}{\eta_{4I}}\right) \tag{12}$$

where

$$D = \frac{D_{2cal}^2}{D_{5cal}^2} \cdot \frac{D_{4cal}}{D_{ical}} \cdot \left(\frac{\eta_{3II}}{\eta_{4II}}\right) \cdot \left(\frac{\eta_{4I}}{\eta_{3I}}\right) \tag{13}$$

To obtain the source absolute flux density by the above method the following quantities are required in addition to the source and calibration deflections.

a. The effective area of the reference aerial as a function of zenith angle along the meridian.
b. The absolute noise diode noise temperature T.
c. Measurements of the hybrid 1 loss ratios.

The reason for adding unmodulated noise from a second, remotely controllable, diode noise source to the output of the calibration modulated diode noise source is to maintain the noise levels in the reference aerial signal paths during calibration at the values that applied for the coaxial switch connected to the reference aerial dipole.

In practice, upon changing the coaxial switch from sky to calibration and the system mode from observe to CAL, the unmodulated diode noise source's output level, for the modulated noise diode source not operating, was adjusted until the noise levels at the reference aerial side inputs to the sine and cosine multipliers had the same values as applied for the coaxial switch connected to the sky and the receiving system set in the observe mode.

The noise levels at the inputs to the total power detector and the East-West aerial inputs to the multipliers in the CAL system modes are a combination of noise from the East-West aerial and the calibration input to hybrid 1. Upon changing the system mode from observe to CAL the change in noise level at the total

power detector input due to the change of noise level at the calibration input to hybrid 1 is compensated by adjusting the noise level of the East-West aerial input to hybrid 1.

In practice, for the modulated calibration noise diode source not operating and after adjustment of the unmodulated diode noise source, the gain of the low gain amplifier located in the East-West aerial signal path before the hybrid 1 input was adjusted until the total power detector input noise levels for the observe and CAL modes were equalized. During calibration the East-West aerial is treated as a noise source. This procedure also closely equalizes the noise levels at the East-West aerial inputs to the multipliers for the observe and CAL system modes.

Maintaining the noise levels in the receiving system at near constancy for the observe and CAL modes reduces the effects of non-linearities in the receiving system.

The present 111.2 MHz flux density calibration method differs from Wyllie method II in that Wyllie employed signal addition hybrids and phase switching to form the interferometer outputs. For Wyllie's receiving system application of a modulated calibration signal to the reference aerial inputs of the addition hybrids produces a calibration deflection. The resulting calibration deflections combined with loss measurements from the addition hybrids to the recorder outputs formed the basis of the receiving system calibration. Wyllie did not employ the observe/CAL system modes or the addition and removal of the 90 degrees phase delay in the CAL-II/CAL-I calibration signal path.

Abbreviations for Fig. 3.1 .

CR : Chart Recorder.

D : Total Power Detector, DC Amplifier and DC Balance.

G : High Gain I.F Amplifier.

H : Hybrid.

LF : Low Pass Filter-amplifier.

O : Switching Waveform Input.

PG : Phase and Gain Control Unit.

PS : Phase Switch.

SD : Synchronous Demodulator.

T : Total Power I.F Amplifier.

X : Multiplier (includes Input Gain Adjustment Units)

Abbreviations for Fig. 3.2 .

C : Converter.

H : Hybrid.

HP : High Pass Filter.

IM : Image Filter.

L.O : Local Oscillator.

N1 : Calibrated Diode Noise Source.

N2 : Uncalibrated Diode Noise Source.

P : Pre-amplifier.

R : 50 Ohm Termination.

S : Noise Diode Power Supply and Diode Current Control.

O ; Switching Waveform Input.

FIG. 3.1 . PHASING HUT AND CONTROL ROOM RECEIVING EQUIPMENT. THE EAST-WEST AERIAL PHASING HUT I.F SYSTEM IS SHOWN IN FIG. 3.3 .

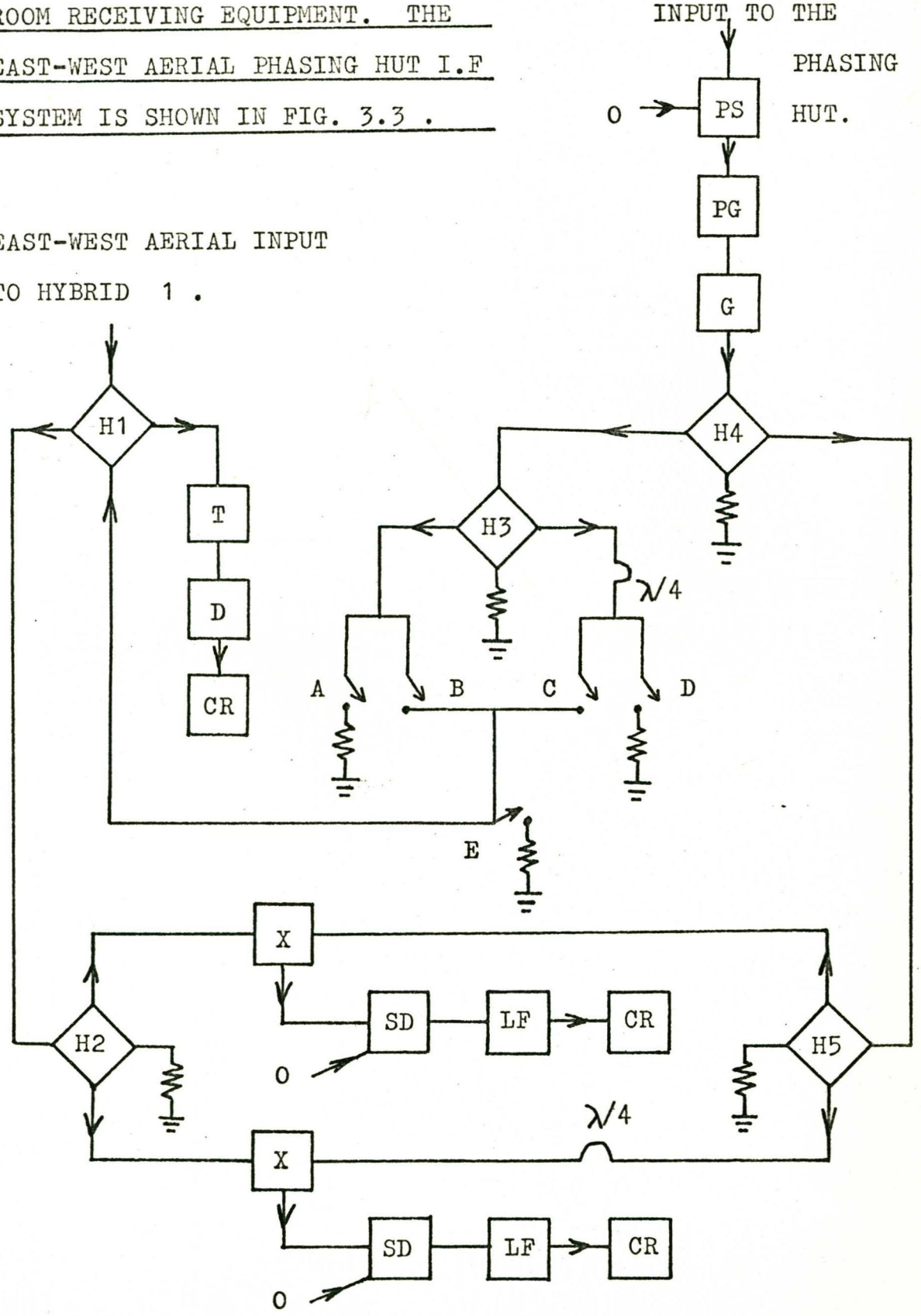

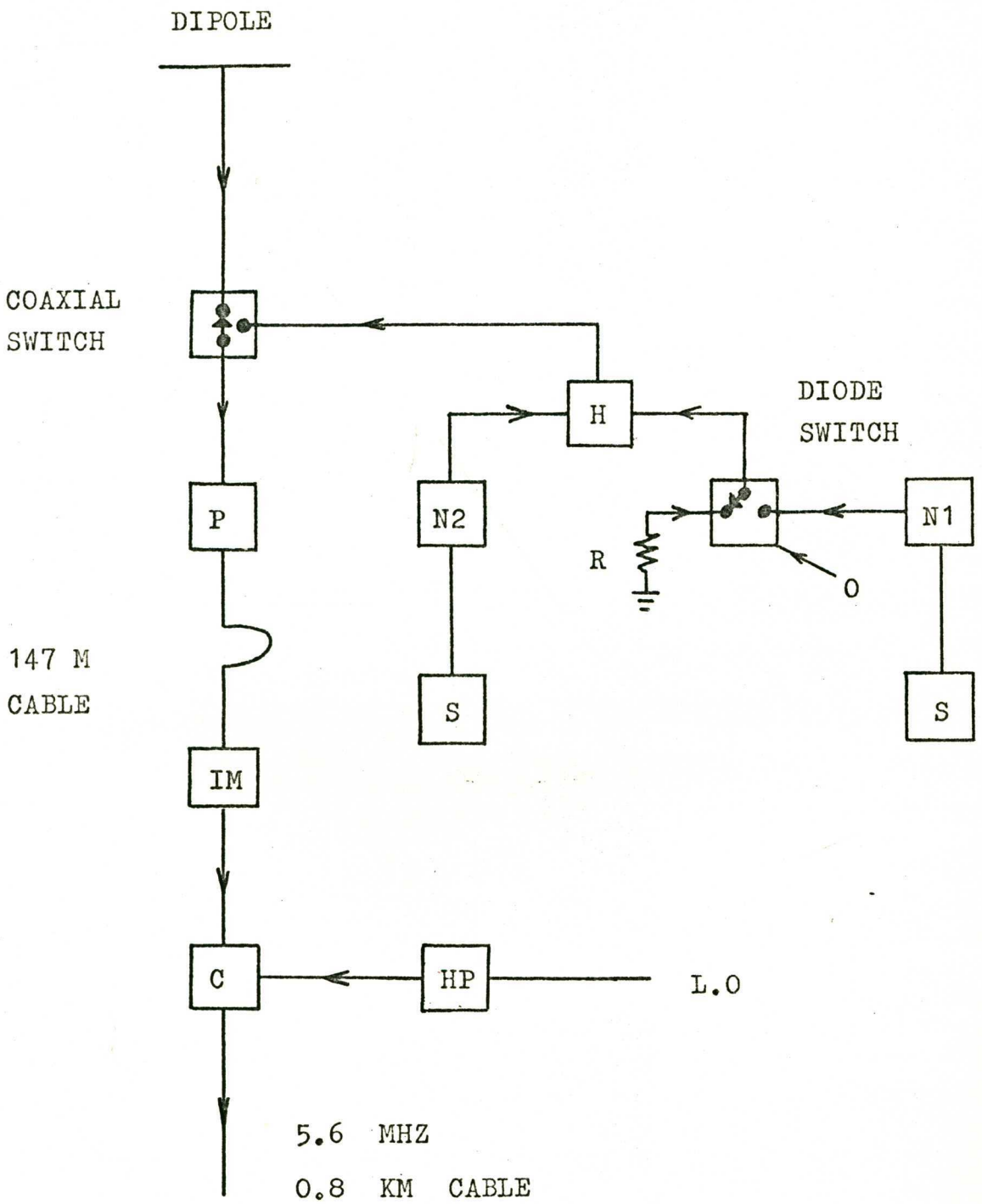

FIG. 3.2 . REFERENCE AERIAL FIELD RECEIVING SYSTEM .

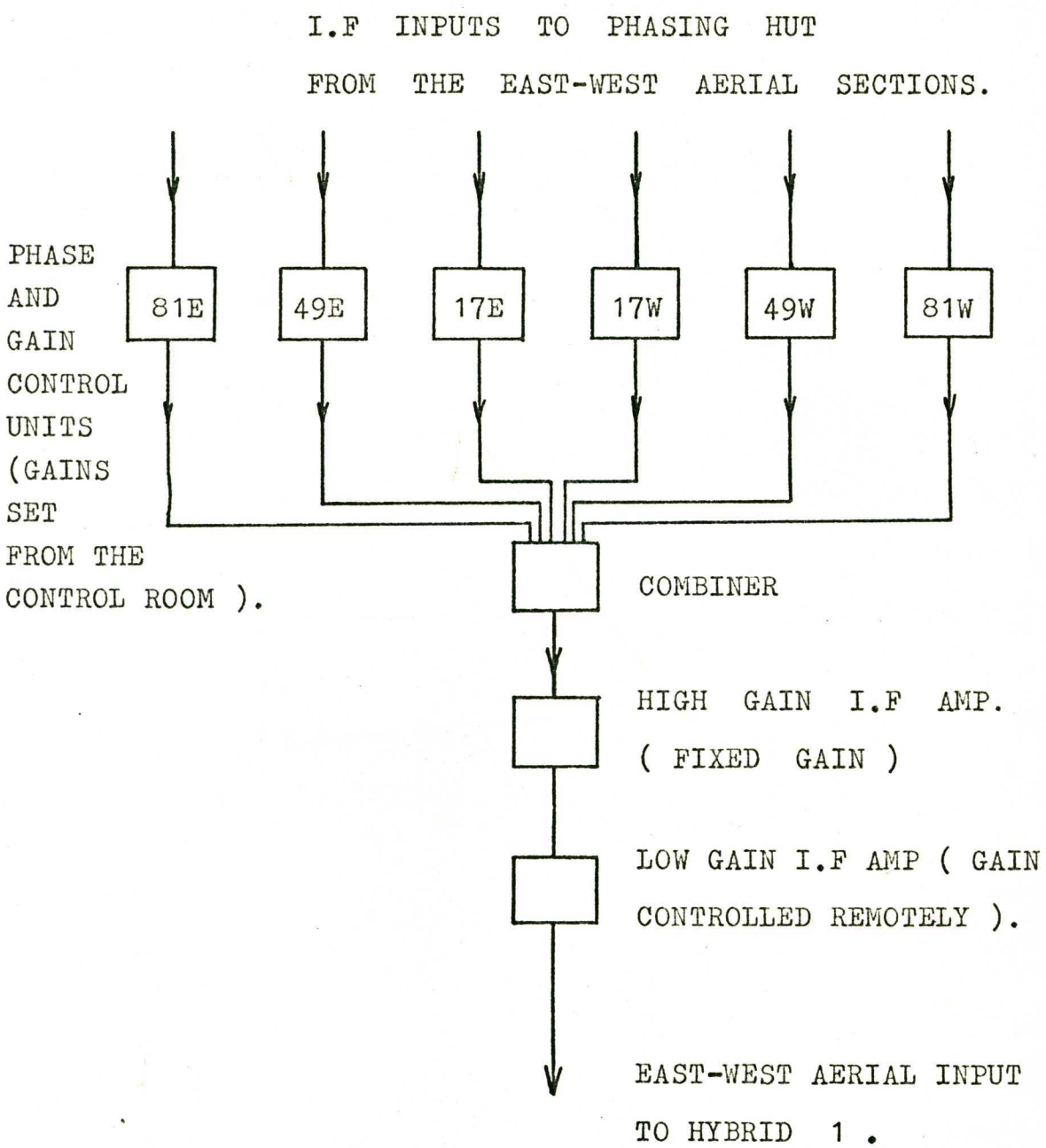

FIG. 3.3 . EAST-WEST AERIAL PHASING HUT SYSTEM .

CHAPTER 4.

THE REFERENCE AERIAL.

At metre wavelengths an aerial of simple geometry for which the effective area is accurately calculable is a horizontal dipole or a simple array of horizontal dipoles over a flat sheet reflector. A single half-wave dipole was used for the 111.2 MHz flux density calibration measurements.

4.1 Definitions.

The reciprocity theorem provides that the radiation patterns of a given aerial are the same for transmission or reception (Schelkunoff and Friis 1952). It is more convenient to consider the reference aerial operating as a transmitter.

Define $U(\theta, \phi)$ as the far-zone radiation intensity i.e the power radiated by the aerial per unit solid angle in the direction defined by the zenith angle θ and the azimuth angle ϕ .

The directivity of an aerial, denoted by D, may be defined as the ratio of the maximun radiation intensity to the average radiation intensity (Kraus 1966). Hence for a given aerial

$$(1) \qquad D = \frac{4\pi . U(\theta, \phi)_{max}}{\iint_{4\pi} U(\theta, \phi) d\Omega}$$

where $U(\theta, \phi)_{max}$ is the maximun radiation intensity and $d\Omega$ is an element of solid angle.

The gain of an aerial, denoted by G, may be defined as the maximun radiation intensity of the aerial divided by the radiation intensity of a lossless isotropic radiator with the same power input (Kraus 1950). The aerial gain is related to the aerial directivity by,

$$G = \eta \cdot D \tag{2}$$

where η is the loss factor in the aerial structure and feed cable.

The effective area of an aerial in the direction of maximun radiation intensity, denoted by A_{max}, is related to the aerial gain by,

$$A_{max} = \frac{\lambda^2}{4\pi} \cdot G \tag{3}$$

The power pattern of an aerial, denoted by $P(\theta, \phi)$

normalized to unity in the direction of maximun radiation intensity is given by,

$$(4) \qquad P(\theta, \phi) = \frac{A(\theta, \phi)}{A_{max}}$$

where $A(\theta, \phi)$ is the effective area of the aerial in the direction (θ, ϕ).

4.2 Calculation of the Reference Aerial Effective Area.

$U(\theta, \phi)$ may be written in the form,

$$(5) \qquad U(\theta, \phi) = I(\theta, \phi) \cdot F(\theta, \phi)$$

where $I(\theta, \phi)$ is the free-space half-wave dipole far-zone radiation intensity and $F(\theta, \phi)$ originates from the presence of the ground plane.

The description of $U(\theta, \phi)$ therefore divides into obtaining suitable expressions for the element factor $I(\theta, \phi)$ and the ground factor $F(\theta, \phi)$.

4.2.1 The Element Factor.

Schelkunoff and Friis (1952) present the following expression for $I(\theta, \phi)$ derived for a sinusoidal dipole current distribution and which takes into account the finite dipole arm radius end-effect,

$$I(\alpha) = \frac{15\, I_o^2}{\pi \sin^2\alpha} \left\{ \cos(k.\delta)\cos\left[\left(\frac{\pi}{2} - k.\delta\right)\cos\alpha\right] - \sin(k.\delta)\cos\alpha \sin\left[\left(\frac{\pi}{2} - k\delta\right)\cos\alpha\right]\right\}^2 \tag{6}$$

where α is a polar angle measured from the axis of the dipole arms and

$$k = 2\pi/\lambda$$

$$\delta = \frac{\lambda}{4} - \ell \tag{7}$$

where ℓ is the physical length of one arm of the dipole and δ is the length by which ℓ is less than one-quarter wavelength. I_o is the amplitude of the sinusoidal dipole current.

4.2.2 The Ground Factor.

Fig 4.1 provides an overhead view of the 111.2 MHz reference aerial's horizontal ground screen. The screen has an inner rectangular region with North-South and East-West dimensions of 1.35 and 1.34 wavelengths respectively, composed of six metallic sheets, thickness 0.8 mm, which overlapped slightly and were soldered together at intervals.

The outer section of the ground screen consisted of wire mesh, cell size 25 by 12 mm and wire diameter 0.9 mm. The overall size of the rectangular ground screen was 3.40 by 3.07 wavelengths North-South and East-West respectively.

The wire mesh and metallic sheets were supported upon a wooden frame. The frame was accurately set horizontally across a grid of surface points by the use of a Surveyor's Level.

The mesh was overlapped onto the ground along the Northern and Southern edges of the ground screen.

The ground plane may be divided into two regions. Firstly the metallic sheet and wire mesh ground screen, above which the horizontal dipole was centrally located. Secondly, a flat horizontal region of imperfectly conducting ground effectively extending to infinity in all directions.

The calculation of the upper hemisphere far-zone radiation intensity consisted of two parts.

(i) Those directions for which the reflected wave strikes the metallic sheet and wire mesh ground screen, regarded as perfectly conducting. In this case the ground factor resulting from the dipole and its induced image is given by,

$$F(\theta) = 4 \sin^2(k.h.\cos\theta), \quad \text{all } \phi . \tag{8}$$

where h is height of the centre of the dipole above the ground screen.

(ii) To calculate the far-zone radiation intensity for those directions for which the reflected wave strikes the imperfectly conducting region of the ground plane the wave incident upon the ground is resolved into its horizontal (TE) and vertical plane of incidence (TM) electric vector components. The positive directions for the incident and reflected TE and TM electric vectors are as defined by Jordan (1950) i.e for the TE component the positive direction is the same for both the incident and reflected electric vector. For the TM case the positive directions are defined such that for vertical incidence the incident and reflected positive directions are parallel and oppositely directed, for grazing incidence the positive directions are parallel and both directed towards the zenith.

Define R_H and R_V as the TE and TM reflection coefficients respectively.

Define $E_H(\theta, \phi)$ and $E_V(\theta, \phi)$ as the far-zone TE and TM components of the direct wave electric vector radiated in the direction (θ, ϕ).

Define $E'_H(\theta, \phi)$ and $E'_V(\theta, \phi)$ as the TE and TM components respectively of the far-zone electric vector in the direction (θ, ϕ) i.e the superpositions of the direct and the reflected far-zone electric vectors of the TE and TM polarizations respectively.

Then from the geometry of the situation obtain the result,

$$E'_H(\theta, \phi) = E_H(\theta, \phi).(1 + R_H e^{-j2k h\cos(\theta)}) \tag{9}$$

and

$$E'_V(\theta, \phi) = E_V(\theta, \phi).(1 - R_V e^{-j2k h\cos(\theta)}) \tag{10}$$

Fig 4.2 defines the geometry to resolve the electric vector $E(\theta, \phi)$ radiated from the dipole towards the ground into its TE and TM components.

The resolved components are given by,

$$E_{TE}(\theta, \phi) = \frac{E(\theta, \phi) \cos \phi}{\sin \alpha}$$

(11)

$$E_{TM}(\theta, \phi) = \frac{-E(\theta, \phi) \cos \theta \cdot \sin \phi}{\sin \alpha}$$

where $\cos \alpha = \sin \theta \cdot \sin \phi$

Write

$$R_H = q_H e^{j\psi_H}$$

(12)

$$R_V = q_V e^{j\psi_V}$$

where q_H and q_V are the amplitudes and ψ_H and ψ_V are the phase angles of the TE and TM reflection coefficients respectively.

Define

$$f_H = 1 + q_H^2 + 2q_H\cos(\psi_H - 2k h\cos\theta)$$

(13)

$$f_V = 1 + q_V^2 - 2q_V\cos(\psi_V - 2k h\cos\theta)$$

Equations (9) and (10) are used to calculate the far-zone radiation intensities for the TE and TM polarizations. The addition of the radiation intensities for both polarizations yields the following expression for the total far-zone radiation intensity.

(14)

$$U(\theta,\phi) = I(\theta,\phi).\left(f_H\left(\frac{\cos\phi}{\sin\alpha}\right)^2 + f_V\left(\frac{\cos\theta\,.\sin\phi}{\sin\alpha}\right)^2\right)$$

4.2.3 Power Absorbed by the Imperfectly Conducting Ground.

The integral $\iint_{4\pi} U(\theta,\phi)\,d\Omega$ equals the total power radiated by the aerial. Integration of the far-zone radiation intensity over the upper hemisphere provides the useful power radiated. For the case of the ground plane including an imperfectly conducting region the power passing into the ground integrated over the lower hemisphere must be added to the useful power radiated to obtain the total power radiated.

The power absorption coefficients for the TE and TM polarizations, denoted by A_H and A_V respectively, are given by,

$$A_H = 1 - q_H^2$$

(15)

$$A_V = 1 - q_V^2$$

Adding the power absorbed for both polarizations the following expression is obtained for the total power absorbed by the ground in the direction (α, ϕ), denoted by $U_G(\alpha, \phi)$.

(16)

$$U_G(\alpha, \phi) = I(\alpha, \phi).(1 - q_H^2(\frac{\cos\phi}{\sin\alpha})^2 - q_V^2(\frac{\cos\alpha.\sin\phi}{\sin\alpha})^2)$$

4.2.4 The Reflection Coefficients.

Schelkunoff and Friis provide the following expressions for the TE and TM reflection coefficients.

$$R_H = -(1 - e^{j\varphi}.\sin\Delta.\sin\Delta_c).(1 + e^{j\varphi}.\sin\Delta.\sin\Delta_c)^{-1}$$

(17)

$$R_V = -(1 - (\frac{\sin\Delta}{\sin\Delta_c}).e^{-j\varphi}).(1 + (\frac{\sin\Delta}{\sin\Delta_c}).e^{-j\varphi})^{-1}$$

where Δ is the angle of elevation of the reflected wave and

$$\varphi = \frac{1}{2} \tan^{-1} \left(\frac{\lambda}{\lambda_c}\right)$$

(18)
$$\lambda_c = \frac{\epsilon_r}{60g}$$

$$\sin \Delta_c = \epsilon_r^{-1/2} . \left(1 + \left(\frac{\lambda}{\lambda_c}\right)^2 \right)^{-1/4}$$

where ϵ_r is the relative dielectric constant and g is the conductivity of the ground. Define,

(19)
$$c = \sin \Delta . \sin \Delta_c$$
$$b = \sin \Delta / \sin \Delta_c$$

The following expressions for the reflection coefficient amplitudes and phase angles may be derived from equations (17) and (19).

(20)
$$q_H = \frac{\left((1 - c^2)^2 + 4.c^2 . \sin^2 \varphi \right)^{1/2}}{1 + c^2 + 2.c.\cos \varphi}$$

$$q_V = \frac{\left((1 - b^2)^2 + 4.b^2 . \sin^2 \varphi \right)^{1/2}}{1 + b^2 + 2.b.\cos \varphi}$$

$$\psi_H = \tan^{-1}\left(\frac{2c\sin\varphi}{c^2 - 1}\right) - \pi$$

(21)

$$\psi_V = \begin{cases} \tan^{-1}\left(\dfrac{2b\sin\varphi}{1 - b^2}\right) & , \; b \geq 1 \\ \tan^{-1}\left(\dfrac{2b\sin\varphi}{1 - b^2}\right) - \pi & , \; b < 1 \end{cases}$$

Burgess (1949) and Schelkunoff and Friis (1952) give typical values for the relative dielectric constant and conductivity for soils of different moisture content. Accurate values for the soil parameters at the site of the reference aerial were not known.

The TE and TM reflection coefficient amplitudes and phase angles at 111.2 MHz, calculated from equations (20) and (21), are presented as a function of the ground reflected wave zenith angle in Figs 4.3 and 4.4. The curves were calculated for the wet and dry soil parameters listed in Schelkunoff and Friis i.e.

Table 4.1

Soil Parameters.

	g (mho/m)	r
Dry Soil	0.015	10
Wet Soil	0.015	30

For a perfectly conducting surface of infinite extent the TE and TM reflection coefficients are -1 and +1 respectively. The ground soil reflection coefficient for the TE electric vector tends towards -1 as grazing incidence is approached i.e tends towards the value of the TE reflection coefficient for a perfectly conducting surface, the far-zone direct and reflected waves tending to cancel. Hence provided the perfectly conducting ground screen is sufficiently large, the TE ground soil reflection coefficient will be a good approximation to -1, and the ground will then appear to the TE electric vector as an infinite extension of the perfectly conducting ground screen.

In the case of the soil TM reflection coefficient the amplitude passes through a minimun (approximately 0.06 and 0.02 for dry and wet soils respectively) and the phase angle changes rapidly from approximately 0° to -180° as the pseudo-Brewster angle (approximately at zenith angles 72° and 79° for dry and wet soils respectively) is passed through with increasing zenith angle. For zenith angles greater than the pseudo-Brewster angle the TM reflection coefficient tends to -1, the far-zone direct and reflected waves then add constructively, thus providing a stronger large zenith angle signal than for the case of a perfectly conducting infinite horizontal plane.

The waves radiated by the reference aerial due East-West and due North-South are completely TE and TM polarized respectively. The zenith angles of the perfectly conducting ground screen wire mesh/soil boundary reflected waves are 83.7 and 84.3 degrees for the East-West and North-South

directions respectively.

Table 4.2 gives the amplitudes and phase angles of the TE and TM reflection coefficients for zenith angles greater and equal to the respective wire mesh/soil boundary zenith angles.

Table 4.2

TE and TM reflection coefficients for zenith angles greater or equal to the wire mesh/soil boundary reflected wave zenith angle for the East-West and North-South directions respectively.

(A) TE Polarization.

Zenith Angle (Degrees)	83.7	86	88	90
(i) Wet Soil				
q_{TE}	0.9608	0.9749	0.9874	1.0000
ψ_{TE} (^{o})	-180.09	-180.06	-180.03	-180.00
(ii) Dry Soil				
q_{TE}	0.9343	0.9578	0.9786	1.0000
ψ_{TE} (^{o})	-180.47	-180.30	-180.15	-180.00

Table 4.2 (continued).

(B) TM Polarization.

Zenith Angle (Degrees)	84.3	86	88	90
(i) Wet Soil				
q_{TM}	0.2953	0.4469	0.6788	1.0000
ψ_{TM} (^{o})	-176.38	-177.91	-179.07	-180.00
(ii) Dry Soil				
q_{TM}	0.5199	0.6366	0.7999	1.0000
ψ_{TM} (^{o})	-175.13	-176.76	-178.44	-180.00

4.2.5 Dipole Aerial Description.

The physical dimensions of the reference aerial dipole are presented in Fig 4.5. The dipole constructed of 12.5mm diameter copper tubing was spaced 0.169 wavelengths above the ground screen. The dipole was connected to 6 metres of 50 ohm coaxial cable. The reference aerial was reflection matched at the cable output, the reflected wave was -40 dB down on the forward wave. The matching was brought about by adjustment of the dipole's arm lengths and of the dipole-reflector separation.

FitzGerrel (1965) provides theoretical curves of the radiation efficiency for a copper half-wave dipole aerial as a function of dipole arm diameter and frequency, where the radiation efficiency is defined as the "ratio of the power radiated to the total power supplied to the aerial at a given frequency". For the dipole utilized in the 111.2 MHz reference aerial the theoretical efficiency is approximately 0.004 dB down on an efficiency of unity.

The two dominant contributions to the power efficiency factor η for the 111.2 MHz reference aerial are the power efficiencies of the cable connecting the dipole aerial to the coaxial switch and of the reference aerial side of the coaxial switch. The two power efficiencies were measured individually and together.

The power efficiency of the connecting cable was determined by the measurement at the cable output of the forward and reflected power for the situation where the dipole aerial end of the cable was short circuited. The combined power efficiency of the connecting cable and aerial side of the coaxial switch was determined by repeating the same measurement procedure at the coaxial switch output. The two measurements may be combined to yield the power efficiency of the coaxial switch. The power efficiency of the coaxial switch was also determined by short-circuiting the input to the aerial side of the coaxial switch and then measuring the ratio of forward and reflected power at the coaxial switch output.

The measurements of the ratios of forward and reflected power were corrected for the loss of any additional cable lengths introduced into the measurement procedure and for the "apparent loss" due to systematic error inherent to the reflectometer. The reflectometer "apparent loss" was determined by the measurement of the ratios of forward and reflected power for the situation where the test item input to the reflectometer was short-circuited.

The dipole end of the connecting cable remained soldered to the dipole arms during the measurement of the cable power efficiency. The contacting surfaces of the dipole arm short-circuit were cleaned to avoid overestimation of the cable loss.

For the March and April 1976 observing sessions the measured reference aerial power efficiency contributions were,

(i) Dipole connecting cable
power efficiency = 0.880 $\pm$ 0.006

(ii) Coaxial switch
power efficiency = 0.992 $\pm$ 0.010

The value for the reference aerial power efficiency factor was,

$$\eta = 0.873 \pm 0.012$$

The quoted standard errors are due entirely to the scatter of the measurements. No allowance was made in η for power losses in the metallic sheet and wire mesh ground screen. Such losses are expected to be very slight ($<$ 1 percent).

The TM electric vector received at the reference aerial from a transiting radiosource may have components parallel to the reference dipole arms and also parallel to the vertical arms of the balun. The balun arms were shielded by a sheet-metal narrow box-like structure to lessen the possibility of reception of the TM electric vector by the balun arms. The East-West and North-South faces of the box were 53 mm (0.02 wavelengths) wide. The box was open at the top, except for a styrafoam cover, and terminated 5 mm below the lower edge of the horizontal dipole arms. The lower end of the box was bolted to the balun baseplate.

4.2.6 Reference Aerial Directivity Calculation.

The integral $\iint_{4\pi} U(\theta,\phi)\,d\Omega$ appearing in equation (1) is made up by,

$$\iint_{4\pi} U(\theta,\phi)\,d\Omega = I_A + I_B + I_C \qquad (22)$$

where I_A is the integral of the far-zone radiation intensity

over the upper hemisphere solid angle for which the reflected wave has come from the perfectly conducting ground screen, I_B is the integral of the far-zone radiation intensity over the upper hemisphere solid angle for which the reflected wave has come from the imperfectly conducting ground plane, I_C is the integral of the radiation intensity absorbed by the ground over the lower hemisphere solid angle subtended by the imperfectly conducting ground plane.

A computer program was written to evaluate, utilizing the previously presented theory, the directivity of an aerial consisting of a half-wave dipole elevated horizontally over the centre of a horizontal rectangular perfectly conducting ground screen surrounded by an imperfectly conducting horizontal surface of infinite extent as described earlier. The dipole was assumed to be at the same height above the perfectly and imperfectly conducting surfaces. The value used in equation (6) for the dipole arm length was the measured arm length.

For an aerial having the same dimensions as the 111.2 MHz flux density measurements reference aerial i.e a dipole-reflector separation of 0.169 wavelengths and a perfectly conducting ground screen having a North-South length of 3.40 wavelengths and an East-West length of 3.07 wavelengths, the directivity was calculated for a dry soil and for a wet soil using the soil parameters listed in Table 4.1. The directivity was also calculated for the aerial having a dipole-reflector separation of 0.169 wavelengths and the perfectly conducting screen extending to infinity in all directions. Table 4.3

lists the aerial directivities for the three types of ground plane.

Table 4.3

Reference Aerial Directivities.

Ground Plane Condition	Directivity
(i) Imperfectly conducting region of the ground plane described by dry soil parameters.	6.838
(ii) Imperfectly conducting region of the ground plane described by wet soil parameters.	6.847
(iii) Perfectly conducting ground screen extending to infinity in all horizontal directions.	6.861

Table 4.3 indicates for the 111.2 MHz reference aerial that the difference between the directivity calculated for the

case of an infinitely extending perfectly conducting ground plane and the directivities calculated for the case of a finite extent perfectly conducting ground plane surrounded by either a dry or wet soil infinite horizontal plane, is less than 1/2 percent.

Table 4.4 gives the fractional contributions of the integrals I_A, I_B and I_C to the integral $\iint_{4\pi} U(\theta,\phi)\, d\Omega$ for the three types of ground plane used in the Table 4.3 directivity calculation.

Table 4.4

Fractional Contributions of I_A, I_B and I_C to $\iint_{4\pi} U(\theta,\phi)\, d\Omega$ for the Table 4.3 Directivity Calculations.

Ground Plane Condition	Fractional Contributions		
	I_A	I_B	I_C
Case (i)	0.9959	0.0011	0.0030
Case (ii)	0.9972	0.0010	0.0018
Case (iii)	1.0000	------	------

The maximun contribution of I_B and I_C to the total integral was 0.4 percent for the case of a dry soil.

Fig 4.6 presents the dependence of the reference aerial directivity upon the spacing of the dipole above the ground screen. The directivity was calculated for a finite extent perfectly conducting ground plane of North-South and East-West dimensions 3.40 and 3.07 wavelengths respectively surrounded by either a dry or wet soil infinite horizontal plane i.e ground plane conditions case (i) and (ii). The difference between the dry and wet soil curves is to slight to be shown in Fig 4.6.

Fig 4.7 presents the dependence of the reference aerial directivity upon the North-South length of the perfectly conducting ground screen. The directivity was calculated for a constant spacing of the dipole above the ground screen of 0.169 wavelengths. The ratio of the East-West length of the perfectly conducting ground screen to the North-South length was kept constant at the value 3.07/3.40, which was the side length ratio used for 111.2 MHz flux density measurement reference aerial. The aerial directivity was calculated for both dry and wet surrounding plane soils.

The calculated directivity (average of the dry and wet soil ground plane conditions), gain and effective area for the 111.2 MHz flux density measurement reference aerial were,

Directivity	=	6.84
Gain	=	5.97
Effective Area	=	3.46 m^2

The reference aerial meridional power pattern is shown in Fig 4.8. The epoch 1950.0 flux density calibration source co-ordinates were precessed to epoch 1976.3 for the calculation of the reference aerial effective area for the individual source declinations.

4.2.7 Reference Aerial Effective Area Uncertainties.

(a) The back to front mesh screen ratio.

From the curves provided by Cottony and Wilson (1960) the reference aerial mesh screen transmission loss for normal incidence is -47 dB at 111 MHz. For several reasons, namely,

(i) The inner section of the ground screen was covered by continuous metallic sheets,

(ii) The transmission loss decreases for incidence angles increasing away from normal incidence,

the result of transmission through the mesh screen upon the reference aerial effective area should be less than 0.5 percent.

(b) Diffraction at the Ground Screen Edges.

The reference aerial dipole is receptive to the transiting source's TM component electric vector. At the zenith angles for all the flux density calibration sources the TM soil reflection coefficient phase angles do not differ appreciably from the perfectly conducting ground reflection coefficient phase angle value, however there exists a major discontinuity in the TM reflection coefficient amplitude across the mesh ground screen/soil boundary (refer to Fig 4.3). Consequently

diffraction due to the TM reflection coefficient amplitude discontinuity at the ground screen mesh edges may have a very significant declination dependent effect on the reference aerial effective area. This question is further discussed in Chapter 8.

(c) Uncertainty in the Dipole-Reflector Separation.

For spacings of the dipole aerial above the ground screen in the neighbourhood of 0.169 wavelengths the rate of change of effective area with dipole-reflector separation is 1 percent per centimetre. The uncertainty in the dipole height over the inner metallic sheet region was less than 0.5 centimetres. The corresponding uncertainty in the reference aerial effective area is less than 0.5 percent.

(d) Uncertainty in the Reference Aerial Orientation.

The reference aerial effective area uncertainty associated with the orientation of the dipole arms along the North-South direction is negligible.

The ground screen was flat over the inner metallic sheet region. The outer wire mesh region was more irregular (r.m.s deviation approximately 1 cm).

The average plane surface of the ground screen, as set by Surveyor's Level, has an uncertainty in the North-South and East-West gradients of $\angle$ 0.1 degrees. Slightly larger local gradients were present in the outer section of the ground screen due to slight warping of the underlying timber frame.

The dipole aerial arms were aligned horizontally by the use of levels and measurements of the separation of the dipole arms from the metallic sheet surface. Near the zenith a small error in the dipole's horizontal alignment produces a negligible effect on the effective area due to the very wide dipole power pattern. Away from the zenith the effect upon the reference aerial's power pattern of a slight tilt of the dipole arms away from the horizontal tends to be compensated by the corresponding tilt of the image dipole.

The uncertainty in the reference aerial effective area due to misalignment of the dipole arms parallel to the average ground screen plane surface is negligible (<0.1 percent).

The uncertainty in the North-South horizontal alignment of the ground screen produces an uncertainty in the effective area which increases with increasing zenith angle. For the 111.2 MHz flux density calibration source having the largest zenith angle at transit i.e Taurus A , the effective area uncertainty is 2 percent.

(e) Uncertainty in the Reference Aerial Efficiency Factor.

The percentage standard error in the reference aerial efficiency factor was taken to be 2 percent.

(f) Element Factor.

The reference aerial maximun effective area was calculated using for the element factor the free-space far-zone radiation intensity expression for an ideal thin half-wave dipole i.e

$$(23) \qquad I(\alpha) = \frac{15\, I_o^2 \cos^2\left(\frac{\pi}{2}\cos\alpha\right)}{\pi \sin^2\alpha}$$

The difference between the calculated maximun effective area for the ideal half-wave dipole element factor and for the element factor supplied by Schelkunoff and Friis i.e equation (6), was 1 percent.

(g) Miscellaneous Uncertainties.

An uncertainty of 2 percent has been allowed for irregularities and losses in the ground plane and scattering by objects in the vicinity of the reference aerial.

The question of coupling between the Western arm of the Molonglo Cross and the reference aerial and the resulting uncertainty in the reference aerial effective area are considered in Chapter 6 section 19.

There existed a slight gradient in the soil ground plane surrounding the ground screen. The Southern edge of the ground screen was slightly elevated (approximately 0.02 wavelengths) above the soil. Since the contributions of the integrals I_B and I_C to the reference aerial directivity are small the effect of the small gradient in the surrounding soil may be neglected.

The resulting standard error in the reference aerial effective area due the above error sources, excluding (b) which is considered in a later Chapter, is 4 percent.

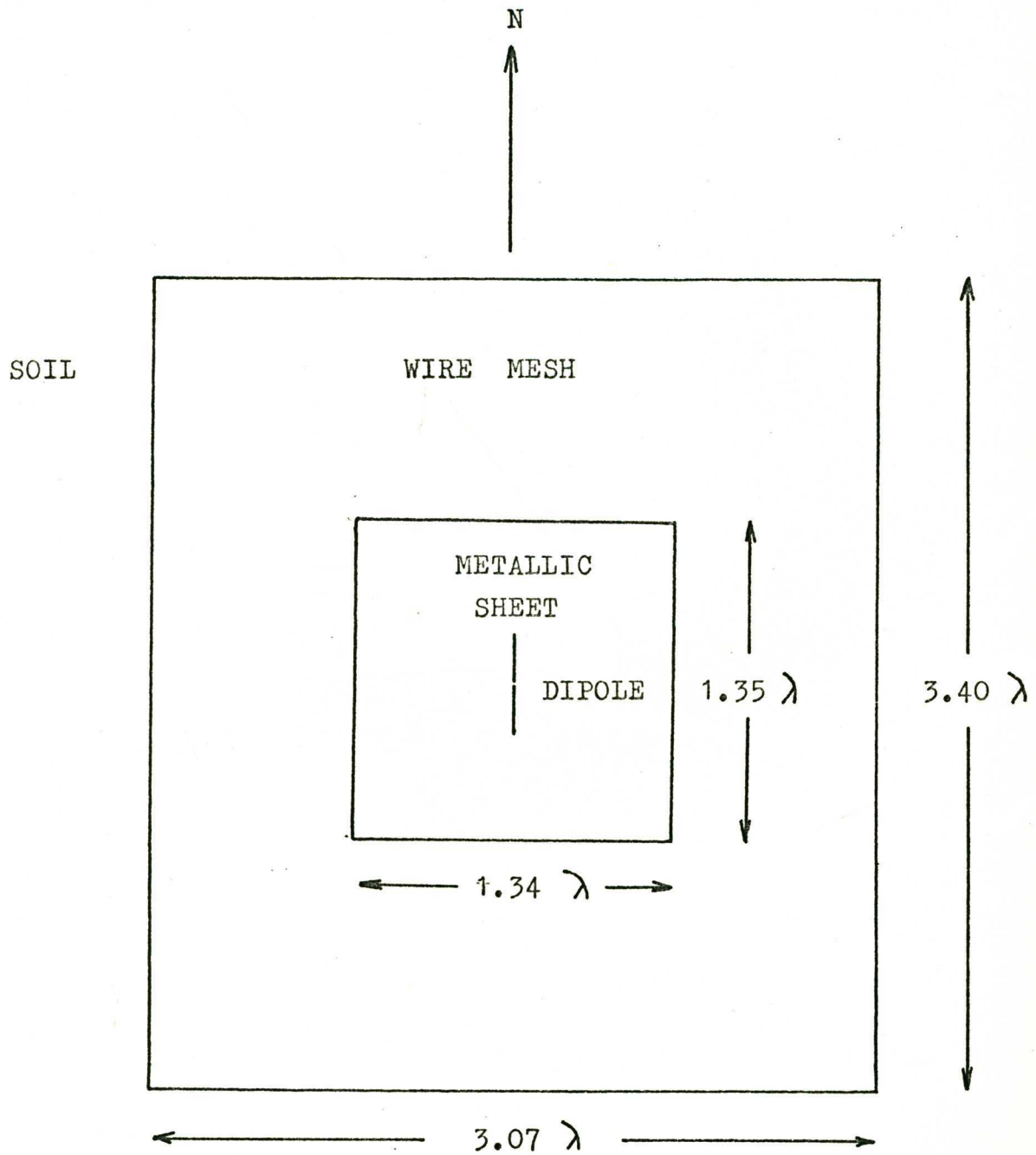

FIG. 4.1 . OVERHEAD VIEW OF THE REFERENCE AERIAL.

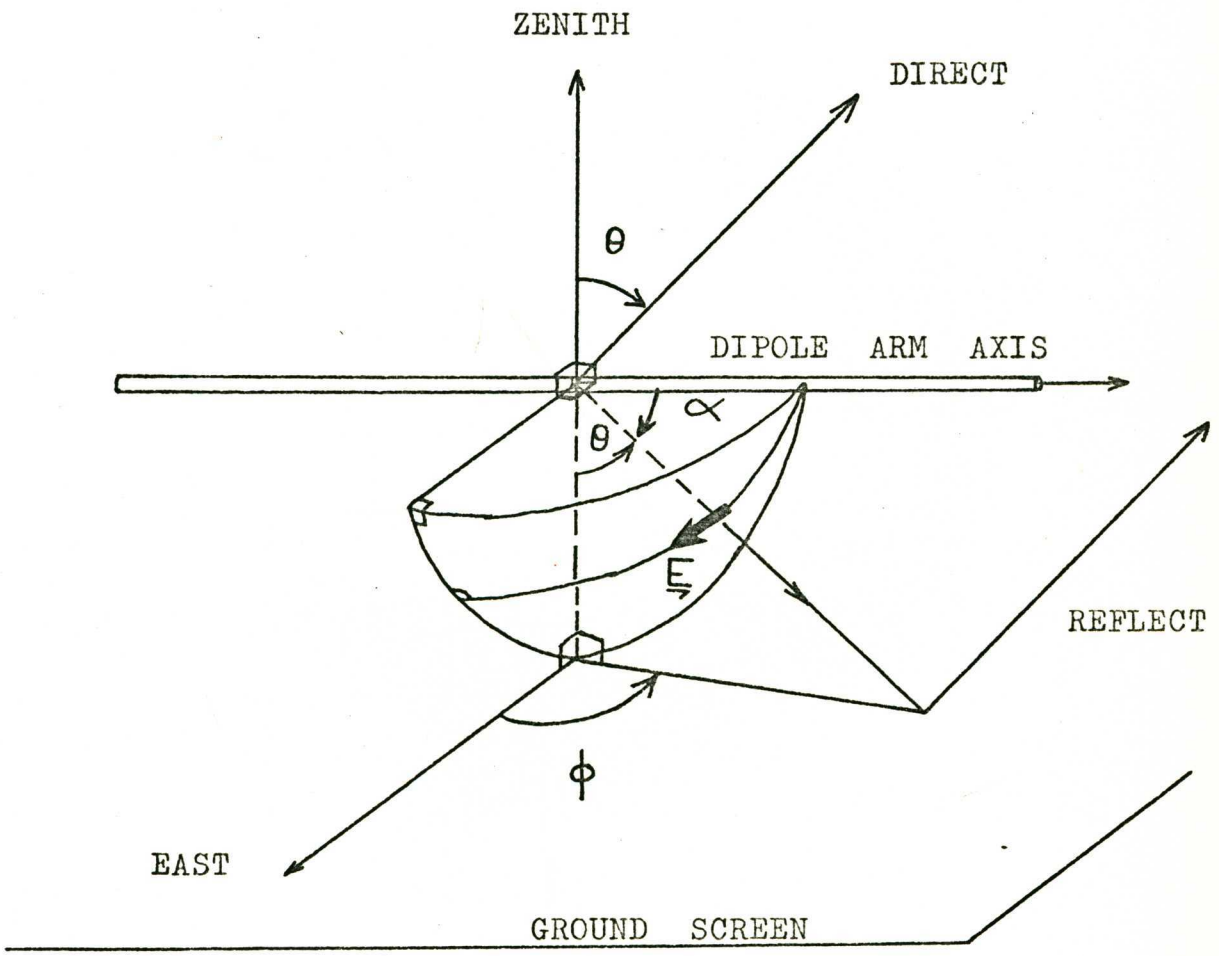

FIG. 4.2 . DIPOLE AND GROUND PLANE CO-ORDINATE SYSTEM . E REPRESENTS THE ELECTRIC VECTOR RADIATED BY THE DIPOLE.

FIG. 4.3 . AMPLITUDES OF THE TE AND TM REFLECTION COEFFICIENTS.

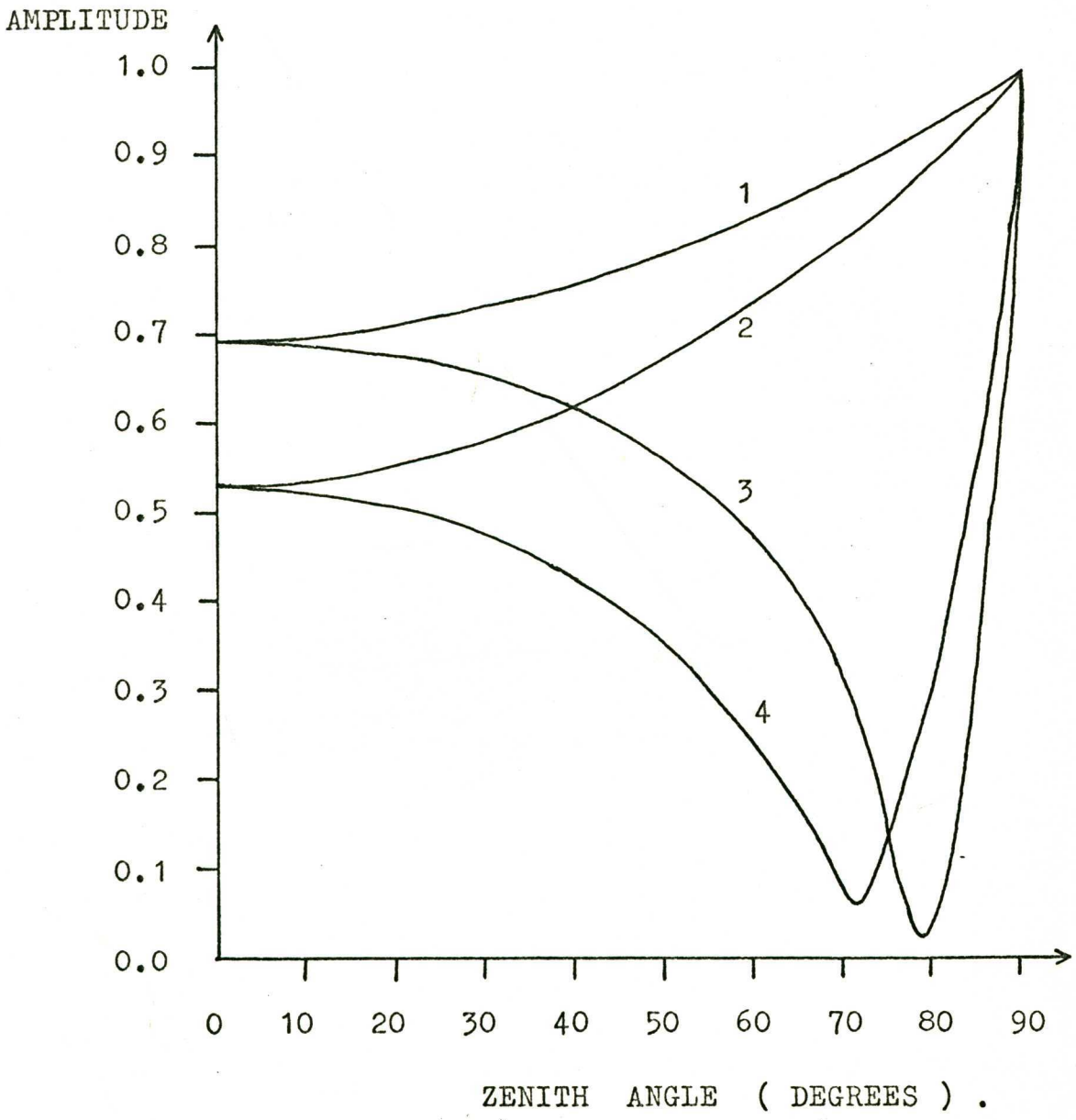

CODE.

1 : q_H (WET SOIL)
2 : q_H (DRY SOIL)
3 : q_V (WET SOIL)
4 : q_V (DRY SOIL)

FIG. 4.4 . PHASE ANGLES OF THE TE AND TM REFLECTION COEFFICIENTS.

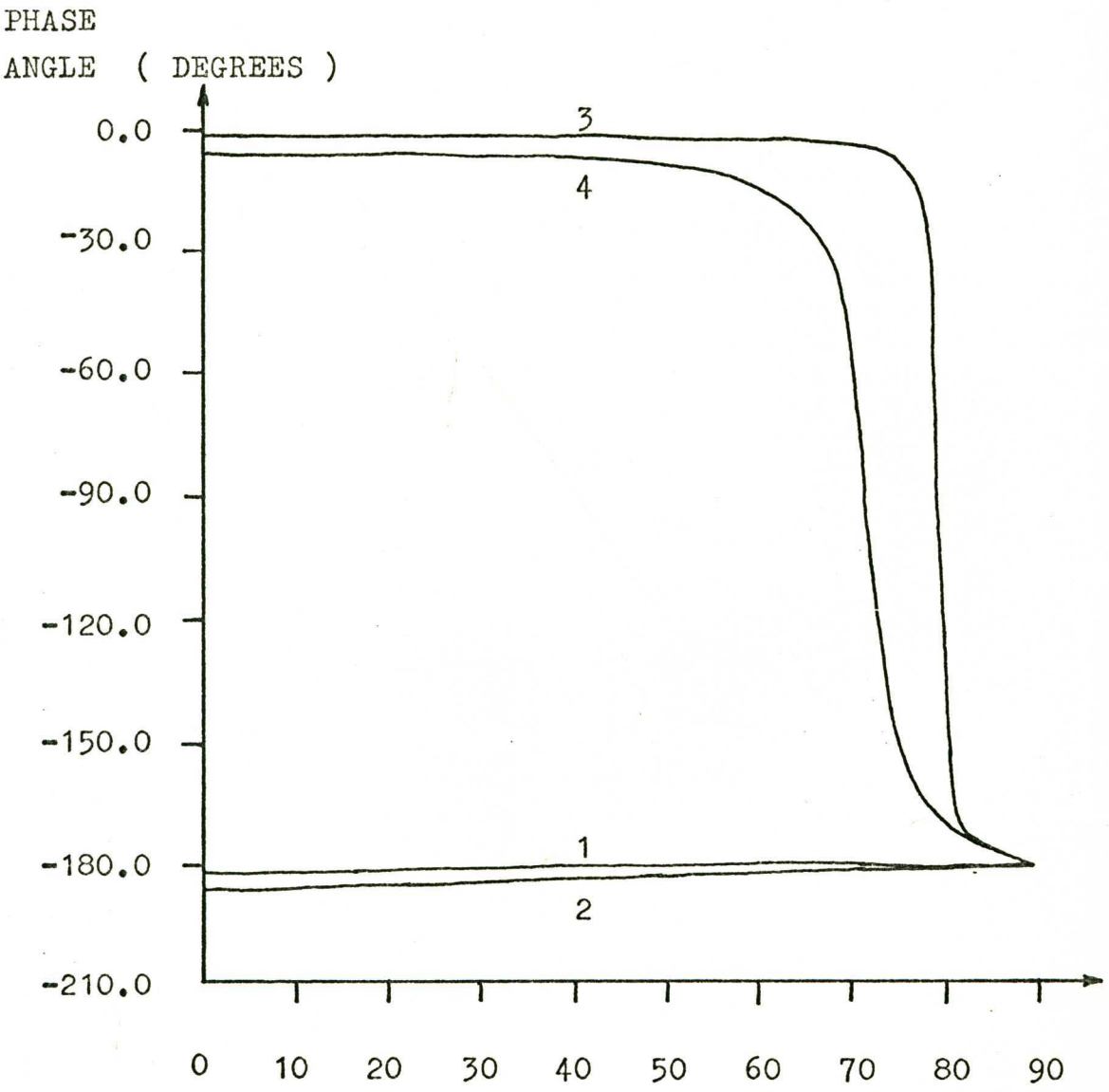

CODE.

1	:	Ψ_H	(WET SOIL)
2	:	Ψ_H	(DRY SOIL)
3	:	Ψ_V	(WET SOIL)
4	:	Ψ_V	(DRY SOIL)

FIG. 4.5 . REFERENCE AERIAL DIPOLE .

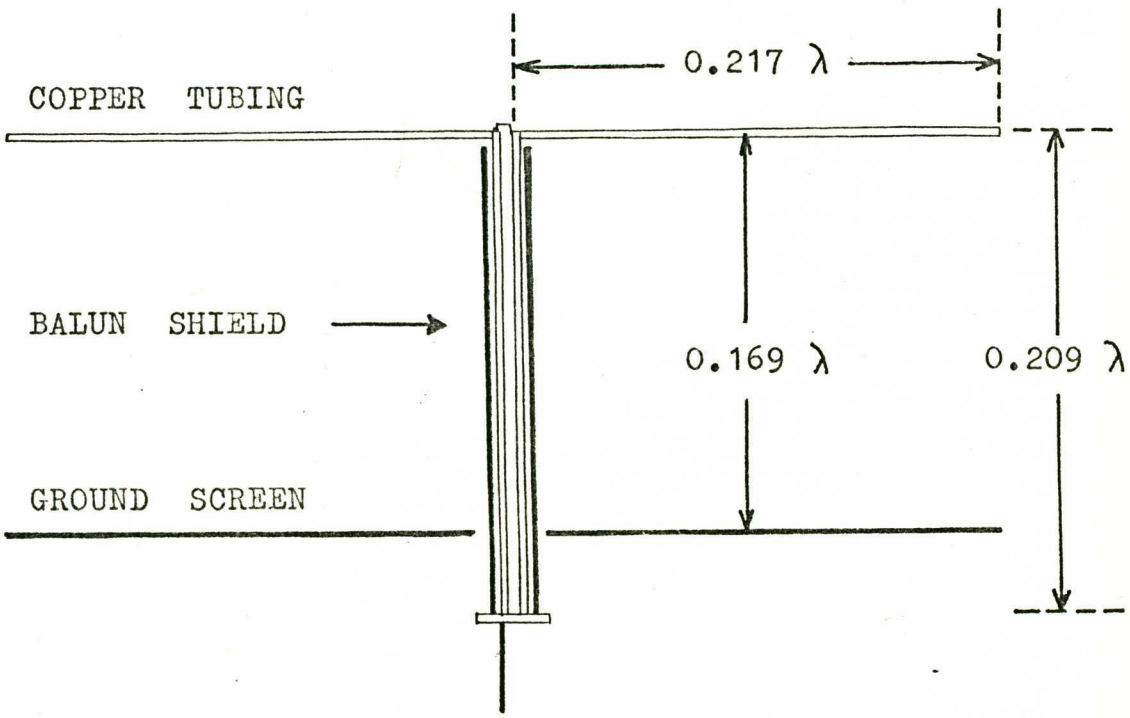

RADIUS OF COPPER TUBING = 2.4×10^{-3} λ

SEPARATION OF THE BALUN ARMS = 7.1×10^{-3} λ

FIG. 4.6 . DIRECTIVITY OF THE REFERENCE AERIAL AS A FUNCTION OF THE HEIGHT OF THE DIPOLE ABOVE THE GROUND SCREEN.

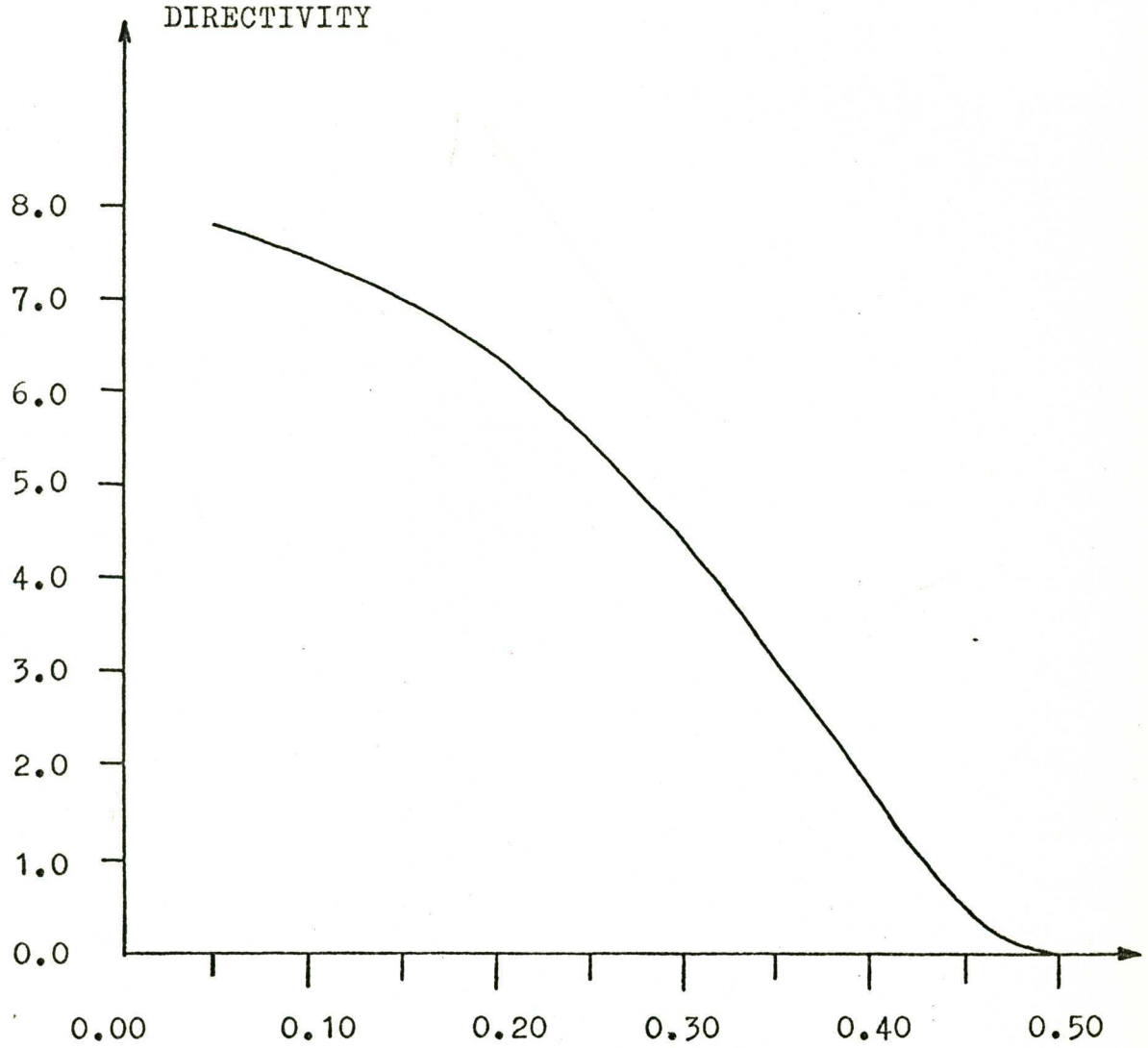

FIG. 4.7 . DIRECTIVITY OF THE REFERENCE AERIAL AS A FUNCTION OF THE NORTH-SOUTH LENGTH OF THE GROUND SCREEN .

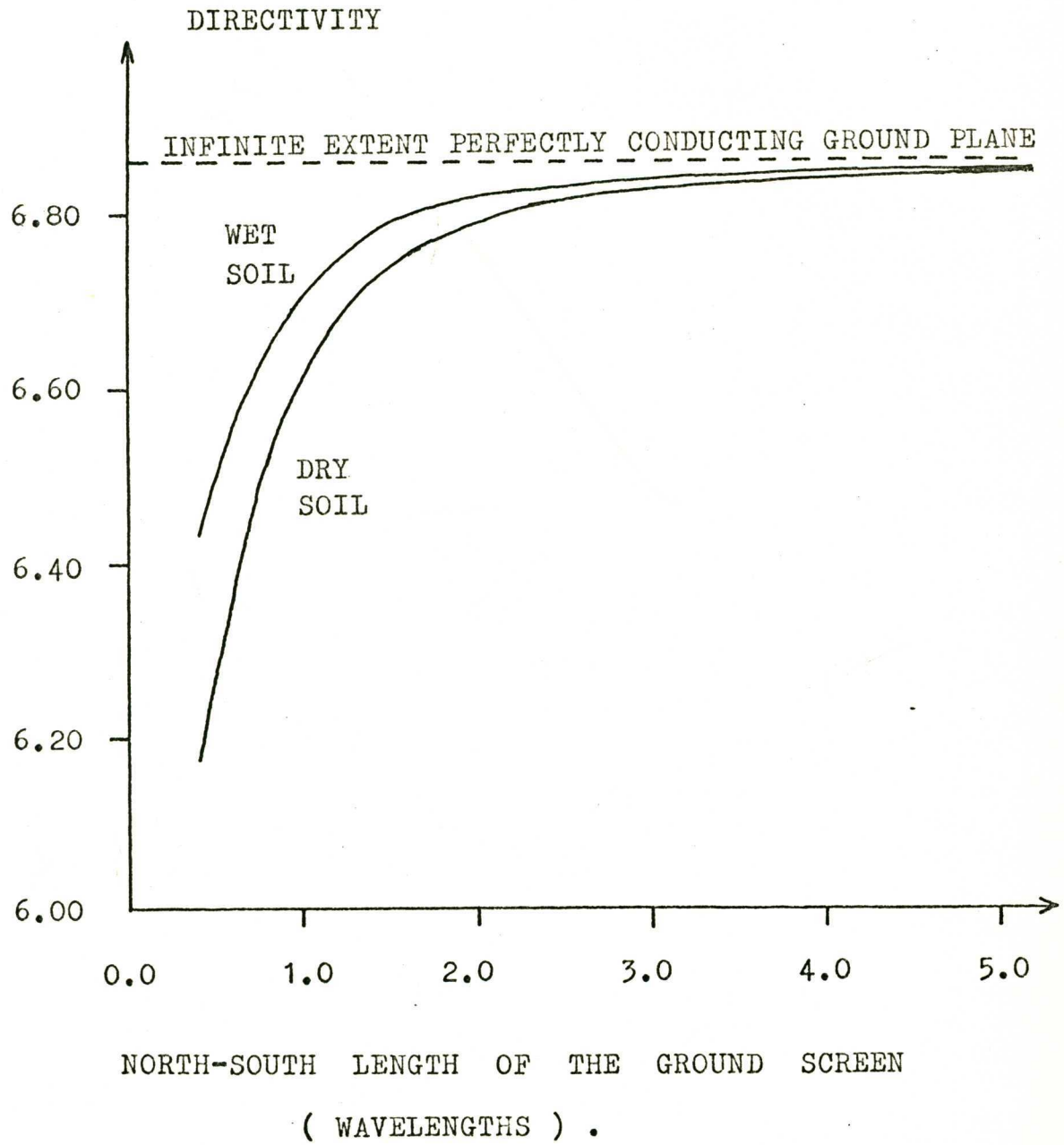

FIG. 4.8 . REFERENCE AERIAL MERIDIONAL POWER PATTERN .

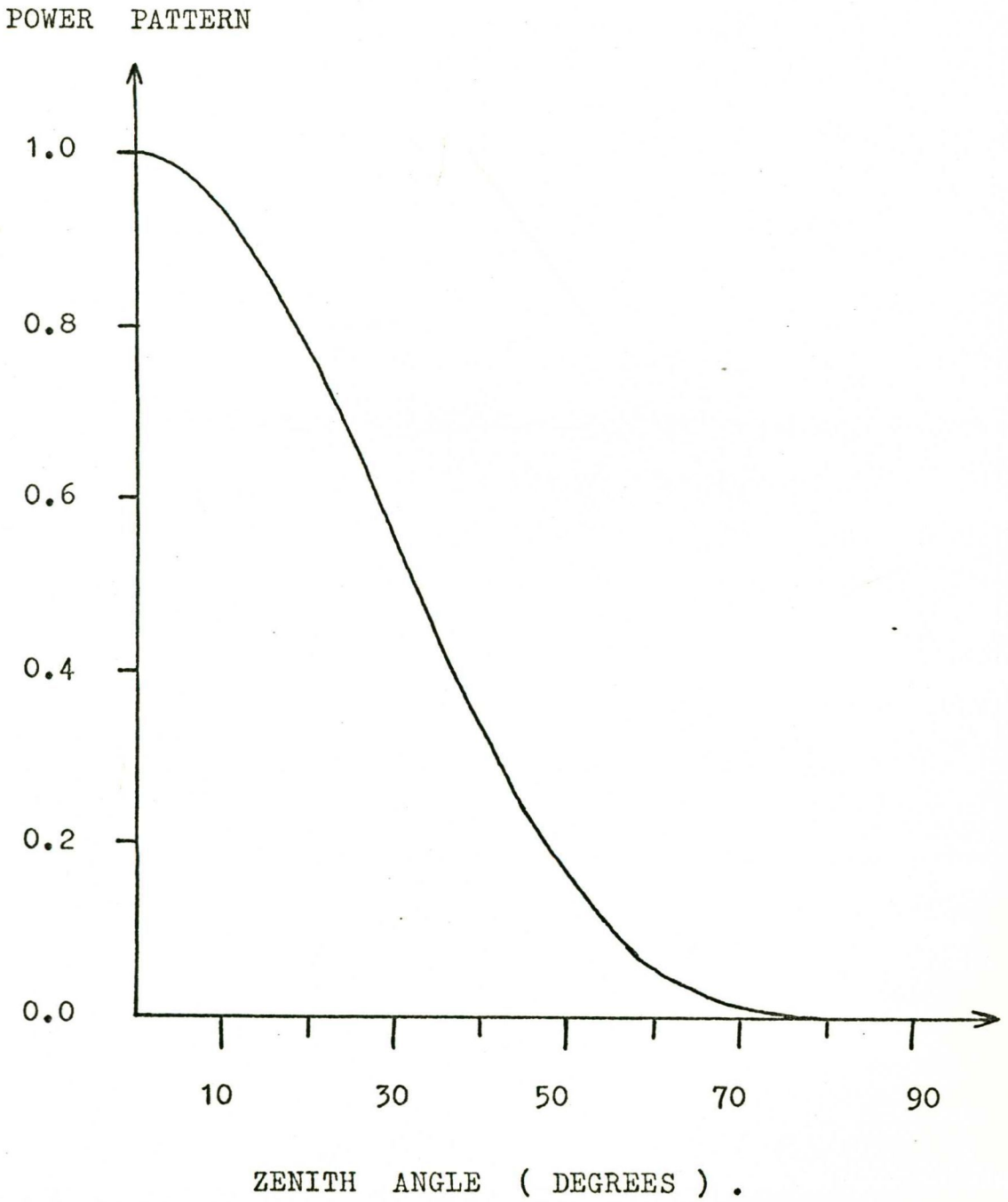

CHAPTER 5.

REFERENCE NOISE SOURCE CALIBRATION.

5.1 The Liquid Nitrogen Load.

The absolute standard of noise temperature for the 111.2 MHz absolute flux density determination consisted of a matched 50 ohm termination immersed in liquid nitrogen.

A saturated diode noise source experimentally calibrated against the liquid nitrogen standard was used as the calibration secondary noise temperature standard during the radiosource observing sessions. The equipment that supplied the flux density measurement receiving system calibration is shown in Fig 3.2. The output of the calibration diode noise source was 100 percent modulated at the switching frequency by the use of a diode switch that switched between a matched 50 ohm termination and the calibration diode noise source.

The calibration of the output noise temperature of the calibration diode noise source for a fixed diode current value against the liquid nitrogen load noise temperature was performed twice.

(i) The noise temperature of the calibration signal at the output of the cable connecting the calibration diode noise source to the 111 MHz addition hybrid was absolutely calibrated in the laboratory at Sydney during March 1974.

(ii) The noise temperature of the calibration signal at the coaxial switch output was absolutely calibrated at the Molonglo

Cross during May 1976.

The cold load consisted of a resistor and brass resistor mount connected to a length (0.12 wavelengths) of low loss rigid coaxial transmission line. The resistor mount was immersed in pure liquid nitrogen contained in a thermos flask. The flask's styrofoam lid allowed the external passage of nitrogen vapour.

The resistor's depth below the liquid nitrogen surface was kept constant, thereby attempting to reduce possible impedance variations due to liquid nitrogen level alterations. The nitrogen load match was measured at 111.2 MHz utilizing a reflectometer and C.W signal generator. The reflected wave was 30 dB below the forward wave.

The normal boiling point (N.B.P) of pure liquid nitrogen is 77.35 ^{o}K (Johnston 1961). During calibration measurements the liquid nitrogen is assumed to be in equilibrium with a pure nitrogen vapour at the local atmospheric pressure. The data supplied by Johnston on the vapour pressure-temperature curve for liquid nitrogen in the neighbourhood of the N.B.P indicates that an increase in the vapour pressure of 0.11 atmospheres results in an increase in the boiling point temperature of 1.0 ^{o}K.

For the March 1974 Sydney calibration measurements the local atmospheric pressure was sufficiently close to one atmosphere to allow the pressure correction to the liquid nitrogen boiling point to be negligible.

The local atmospheric pressure for the May 1976 Molonglo calibration was 0.940 atmospheres. The resulting pressure correction was a decrease of 0.55 ^{o}K in the liquid nitrogen boiling point.

The N.B.P of oxygen is 90.2 ^{o}K. Oxygen dissolving into the liquid nitrogen elevates the boiling point. A mole percentage of 5 percent dissolved oxygen will elevate the boiling point of liquid nitrogen by 0.6 ^{o}K. The increase in the boiling point of liquid nitrogen at the depth of the load resistor due to the extra hydrostatic pressure was estimated to be approximately 0.004 ^{o}K and can thus be neglected.

Stelzried (1965) treats the calculation of the effective output noise temperature, denoted by T' ^{o}K, of a noise source consisting of a matched resistive element at thermal temperature T ^{o}K delivering power through a uniform lossy transmission line. The line temperature and attenuation may vary along the length of the transmission line.

Assume the following conditions.

(a) The transmission line loss is less than 0.5 dB.

(b) Constant attenuation along the transmission line.

(c) Approximating by a linear distribution the transmission line temperature between the resistive termination and the transmission line output.

(d) Assume the transmission line output is at ambient temperature, denoted by T_o ^{o}K.

Stelzried presents the following expression for the equivalent output noise temperature of the noise source under the above listed assumptions.

$$(1) \qquad T' = T + \frac{(T_o - T)}{2} \cdot L - \frac{(T_o - T)}{6} \cdot L^2 +$$

where L is 0.2303 times the insertion loss ratio, expressed in decibels, of the transmission line. For the liquid nitrogen load T represents the temperature of the resistor immersed in liquid nitrogen. The measured transmission loss of the rigid coaxial line was 0.05 $\pm$ 0.01 dB (April 1974).

The values of the liquid nitrogen load output noise temperature for the ambient temperature and pressure conditions for the March 1974 and May 1976 calibration experiments as given by equation (1) are supplied in Table 5.1.

Table 5.1

Nitrogen Load Output Noise Temperatures (T').

Session	Average Ambient Temperature ^oK	T' (^oK)
March 1974	299.5	78.64
May 1976	287.2	78.01

5.2 March 1974 Calibration Methods.

5.2.1 Calibration Method I.

Fig 5.1 details the experimental system originally tried in order to calibrate the calibration diode noise source.

A diode switch enables the pre-amplifier input to be switched at the switching frequency between a fixed matched termination (50 ohm) and a matched load which may be either the liquid nitrogen load or the calibration diode noise source or a matched termination.

The receiving system's output voltage from the synchronous demodulator was recorded on a chart recorder. Let the diode switch input to which the different loads are connected be termed the CAL input. The calibration diode noise source included the diode switch used to provide the 100 percent modulation of the calibration signal during radiosource calibration and also included the cable employed to connect the diode noise source to the 111 MHz addition hybrid. The calibration diode noise source diode switch remained biased to the diode noise source side during the laboratory calibration experiments.

Make the following assumptions.

(a) The amplifiers in the receiving system are linear and the receiver detector is square-law.

(b) The CAL input loads i.e the liquid nitrogen load, calibration diode noise source and the matched 50 ohm

terminations are well matched (reflection matches better or equal to -30 dB) and the receiving system output is assumed to be independent of the small impedance differences between the CAL input loads.

The zero for deflection measurements was defined by placing the matched 50 ohm termination on the diode switch CAL input.

The receiving system output deflection, denoted by D_L, corresponding to the liquid nitrogen load placed on the diode switch CAL input is given by,

$$D_L = B.(T_o - T') \qquad (2)$$

where B is a constant.

The calibration diode noise source output noise temperature is given by $T_o + T_N$ where T_N is the calibration signal noise temperature due to the diode's direct current.

The output deflection corresponding to the calibration diode noise source connected to the diode switch CAL input, denoted by D_N, is given by,

$$D_N = -B.T_N \qquad (3)$$

From equations (2) and (3) obtain the following result,

$$(4) \qquad \frac{D_N}{D_L} = - \frac{T_N}{(T_o - T')}$$

In practice the baseline was found to alter significantly with input impedance. The reflection matches of the liquid nitrogen load, calibration diode noise source and matched terminations were all better than or equal to -30 dB. The ratio D_N/D_L for a particular diode direct current was found to vary systematically with the system noise temperature in a manner consistent with the presence of non-linearity in the receiving equipment.

5.2.2 Calibration Method II.

In order to remove the effects of the receiving system non-linearity present in calibration method I a second method was developed which involved the balance of noise power at the pre-amplifier input for either the fixed matched termination or CAL diode switch sides connected to the receiving system input.

As in method I the liquid nitrogen load, calibration diode noise source or a matched termination was switched at

400 Hz against a fixed matched termination.

The output of the diode switch was added by a 111 MHz hybrid to the output from a second diode noise which was also switching against a matched termination. Depending upon which two sides of the two diode switches are added together in the hybrid, the total noise power at the pre-amplifier input may be equalized for both switching positions.

Fig 5.2 shows a block diagram of the experimental system employed for the second calibration method. In this system a matching stub was located on the CAL input to the first diode switch. The liquid nitrogen load, calibration diode noise source and non-fixed matched termination impedances as measured from the reflectometer location shown in Fig 5.2 were adjusted by the matching stub to within 0.2 dB of the measured reflection match of the permanently positioned 50 ohm termination on the first diode switch, thereby attempting to eliminate possible CAL input impedance dependent gain and noise figure variations in the receiving system.

Define α as the efficiency factor for the signal path between the CAL input to the first diode switch and the location of signal addition in the hybrid,

β as the efficiency factor of the signal path between the output of the second uncalibrated diode noise source and the location of signal addition in the hybrid,

γ as the efficiency factor from the location of signal addition to the pre-amplifier input.

The noise temperature of the output of the second diode

noise source is given by $T_o + C.I$ where C is a constant and I is the second diode noise source's direct diode current.

Consider the case of the liquid nitrogen load connected to the first diode switch CAL input. The second diode noise source output power is added to the liquid nitrogen load output noise power to achieve noise power equalization for the two switching positions at the pre-amplifier input. The noise temperatures at the pre-amplifier input, denoted by T_1 and T_2 respectively, for the two switching positions are given by,

(i) Diode switch liquid nitrogen load side connected.

$$(5) \qquad T_1 = \frac{\gamma}{2} \cdot (\alpha(T' - T_o) + \beta.C.I_1) + T_o$$

(ii) First diode switch fixed termination side connected.

$$(6) \qquad T_2 = T_o$$

Therefore for noise temperature balance i.e $T_1 = T_2$ obtain from equations (5) and (6) the relationship,

$$(7) \qquad T_o - T' = \frac{\beta}{\alpha} \cdot C \cdot I_1$$

The factor of 1/2 is the hybrid efficiency factor and I_1 is the liquid nitrogen load balance direct current of the second diode noise source.

For the case of the calibration diode noise source connected to the CAL input of the first diode switch the phase of the 400 Hz switching signal supplied to the second diode switch was altered by 180 degrees to the case in which the liquid nitrogen load was connected to the first diode switch CAL input. The pre-amplifier input noise temperatures, denoted by T_3 and T_4 respectively, for both switching positions are given by,

(i) CAL input diode switch side connected.

$$T_3 = \frac{\gamma}{2} . \alpha . T_N + T_o \tag{8}$$

(ii) First diode switch fixed termination side connected.

$$T_4 = \frac{\gamma}{2} . \beta . C . I_2 + T_o \tag{9}$$

Therefore for noise temperature balance i.e $T_3 = T_4$ obtain from equations (8) and (9) the relationship,

$$T_N = \frac{\beta}{\alpha} . C . I_2 \tag{10}$$

where I_2 is the second diode noise source balance current for a particular calibration diode noise source direct diode current.

Equations (7) and (10) may be combined to give the following final relationship.

$$(11) \qquad \frac{T_N}{(T_o - T')} = \frac{I_2}{I_1}$$

The procedure for carrying out the experiment was as follows.

(a) The receiving system output zero corresponding to noise temperature equalization at the pre-amplifier input was defined by placing a matched termination on the CAL input to the first diode switch and by turning off the direct diode current of the second diode noise source.

(b) For either the calibration diode noise source or the liquid nitrogen load connected to the first diode switch CAL input the direct diode current of the second diode noise source was adjusted until the system output was zeroed.

The permanently located 50 ohm terminations on both diode switches are assumed to be at ambient temperature. The diode noise source's output noise temperature includes a contribution assumed to be due to an increase in the diode noise source thermal temperature above ambient originating when the direct

diode current is flowing. Both diode noise sources exhibit this effect.

Equation (11) was derived on the assumption that the calibration diode noise source and the second diode noise source output noise temperatures were $T_o + T_N$ and $T_o + C.I$ respectively. Corrections need to be applied to the balance currents I_1 and I_2 to allow for the additional noise temperature contributions.

Let the additional noise temperature contributions to the calibration diode noise source and the second diode noise source output noise temperatures be termed T_{H1} and T_{H2} respectively. The experiment aims to measure T_N i.e the excess output noise temperature of the calibration diode noise source, for a particular direct diode current value, above the output noise temperature for the direct diode current not flowing. T_N does not include T_{H1}, since T_{H1} persists, decreasing slowly with time, after the calibration diode noise source direct current is switched off.

Table 5.2 lists the output noise temperatures of the calibration diode noise source and the second diode noise source for the following situations applying to the calibration experiment.

(a) Both noise source diode currents switched off and both of the diode noise sources are in thermal equilibrium with the surrounding room temperature.

(b) At noise power balance.

(c) Subsequent to noise power balance and with both diode noise source direct diode currents switched off.

Table 5.2

Output Noise Temperatures.

Case.	Calibration Diode Noise Source.	Second Diode Noise Source.
(a)	T_o	T_o
(b)	$T_o+T_N+T_{H1}(t)$	$T_o+C.I+T_{H2}(t)$
(c)	$T_o+T_{H1}(t)$	$T_o+T_{H2}(t)$

Both T_{H1} and T_{H2} are functions of time.

Experimentally T_{H1}/T_N and $T_{H2}/(C.I)$ are not difficult to measure. In the manner in which the calibration experiment was carried out, for a calibration diode noise source direct current meter reading of 1.00 mA the ratios T_{H1}/T_N and $T_{H2}/(C.I_2)$ averaged 0.020 and 0.009 respectively.

In the case of the liquid nitrogen load connected to the first diode switch CAL input the ratio $T_{H2}/(C.I_1)$ averaged 0.013.

The average correction to the measured noise temperature balance current ratio I_2/I_1 was a reduction of 2.5 percent.

The difference between the matching stub losses for the impedance adjustment of either the liquid nitrogen load or the calibration diode noise source was assumed to be negligible. A subsidiary experiment indicated consistency with this assumption. A 1 percent correction was applied to the balance current ratio I_2/I_1 to allow for possible non-linearity in the dependence of the second diode noise source output noise temperature upon the direct diode current meter reading.

The value of T_N for a calibration diode noise source direct diode current meter reading of 1.00 mA was measured by calibration method II at,

$$T_N = 346 \pm 6 \ ^oK$$

The standard error in T_N due to scatter in the I_2/I_1 ratios was only 0.5 percent.

5.3 May 1976 Calibration Experiment.

5.3.1 Calibration Method III.

The noise temperature, T_N, of the calibration signal was measured at the output of the coaxial switch for the May 1976 calibration measurements. Fig 5.3 shows a block diagram of the equipment used for the May calibration experiment at the Molonglo Cross radiotelescope.

The equipment operates as a total power receiver. Assume that all the receiving system amplifiers are linear, the detector square-law and that the output of the total power detector is not dependent upon the impedance of the load presented to the pre-amplifier input. The detector output was recorded on a chart recorder.

If a matched termination, at ambient temperature, is placed on the pre-amplifier input the resulting recorder deflection, denoted by D_T, is given by,

$$D_T = B.(T_o + T_s) - O \qquad (12)$$

where B is a constant, T_s is the system noise temperature less the noise temperature contributed by the load placed on the pre-amplifier input and O is the D.C offset applied to the detector output.

The recorder deflection, denoted by D_L, resulting for the liquid nitrogen load placed on the pre-amplifier input is given by,

$$D_L = B.(T' + T_s) - O \qquad (13)$$

For the calibration diode noise source, which was 100 percent modulated at 400 Hz, placed on the pre-amplifier input the

resulting recorder deflection, denoted by D_N, is given by,

$$(14) \qquad D_N = B.\left(T_o + \frac{T_N}{2} + T_s \right) - O$$

Equations (12), (13) and (14) may be combined to give the following relationship.

$$(15) \qquad \frac{D_N - D_T}{D_T - D_L} = \frac{T_N}{2.(T_o - T')}$$

In practice small input impedance dependent effects were present at the detector output. This effect is assumed to produce errors in the deflection measurements at the 1 percent level. Non-linearity was present in the receiving system. The non-linearity was investigated by a method similar to the procedure for obtaining total power non-linearity receiving system corrections as described in Chapter 6 section 9.

In outline, the unmodulated uncalibrated diode noise source is used to alter the system noise temperature. Recorder deflections resulting from the calibration diode noise source operating at two fixed values of diode current meter reading are superimposed upon the recorder level defined by the unmodulated diode noise source. Values of system noise

temperature are selected to cover the range of system noise temperatures present in the calibration experiment. An analysis of the superimposed deflections enables evaluation of the non-linearity corrections. A non-linearity correction of 1.6 percent was applied to the equation (15) deflection ratio.

The same ammeter was used for the calibration diode noise source direct diode current readings in the March 1974 and May 1976 noise temperature comparison experiments and for all the radiosource observing sessions i.e March and April 1976.

The value of T_N for a calibration diode noise source direct diode current meter reading of 1.00 mA was measured by calibration method III at,

$$T_N = 165 \pm 3 \ ^oK$$

The standard error in T_N due to scatter in the deflection ratios was 0.17 percent.

5.4 Comparison of the March 1974 and May 1976 T_N Values.

To compare the March 1974 value of T_N with the May 1976 value, the March T_N value must be corrected for losses of the 111 MHz addition hybrid, coaxial switch and added connecting cables.

The corrected March 1974 value of T_N for a direct diode current meter reading of 1.00 mA is,

$$T_N = 169 \pm 4 \ ^{o}K$$

The ratio of the March 1974 value of T_N to the May 1976 value is 1.024 ± 0.031 . The March 1974 and May 1976 T_N values are in moderately good agreement. The May 1976 value of T_N was adopted for the absolute calibration of the March and April of 1976 radiosource observations.

Abbreviations for Figs. 5.1, 5.2 and 5.3 .

C : Converter.

CR : Chart Recorder.

D : Total Power Detector, DC Amplifier and DC Balance.

DS : Diode Switch.

DS1 : Diode Switch 1 .

DS2 : Diode Switch 2

DV : Digital Voltmeter.

H : Addition Hybrid.

HP : High Pass Filter.

I : I.F Amplifiers.

IM : Image Filter.

L : Liquid Nitrogen Load/Reference Diode Noise Source/ 50 Ohm Termination.

LO : Local Oscillator.

NG2 : Second Diode Noise Source (Uncalibrated).

O : Switching Waveform Generator.

P : Pre-amplifier.

R : 50 Ohm Termination.

RE : Receiver.

RR : Reflectometer.

SD : Synchronous Demodulator.

SW : Switch to Alter the Phase of the 400 Hz Switching Signal by 180 degrees.

TS : Tuning Stub.

FIG. 5.1 . DIODE NOISE SOURCE CALIBRATION METHOD I .

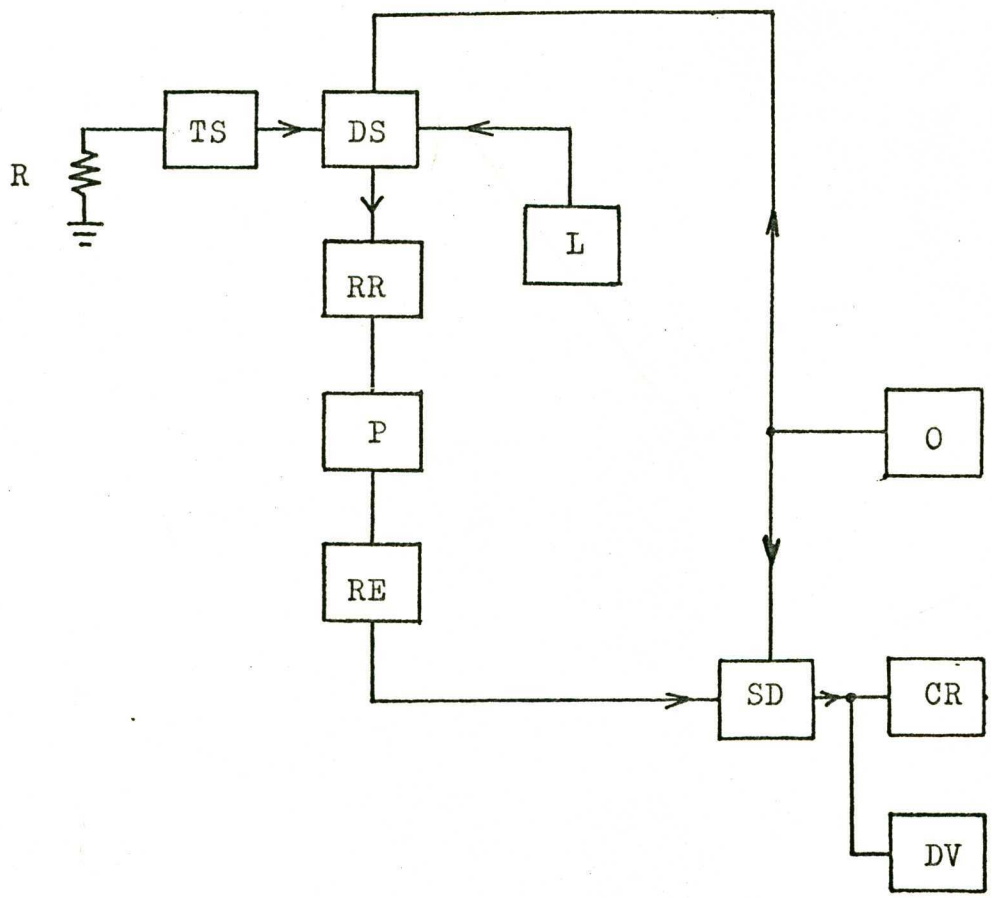

FIG. 5.2 . DIODE NOISE SOURCE CALIBRATION METHOD II .

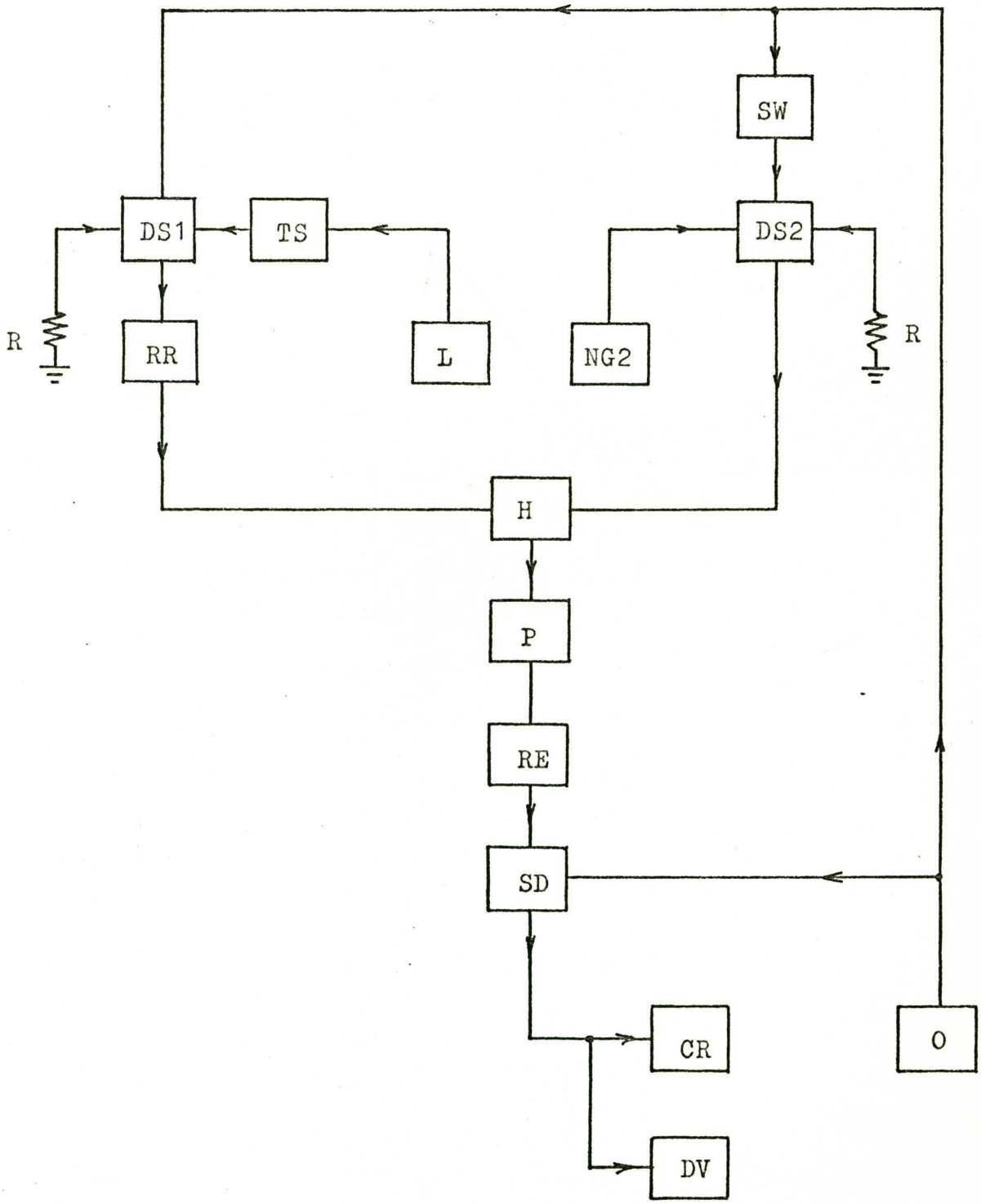

FIG. 5.3 . DIODE NOISE SOURCE CALIBRATION METHOD III .

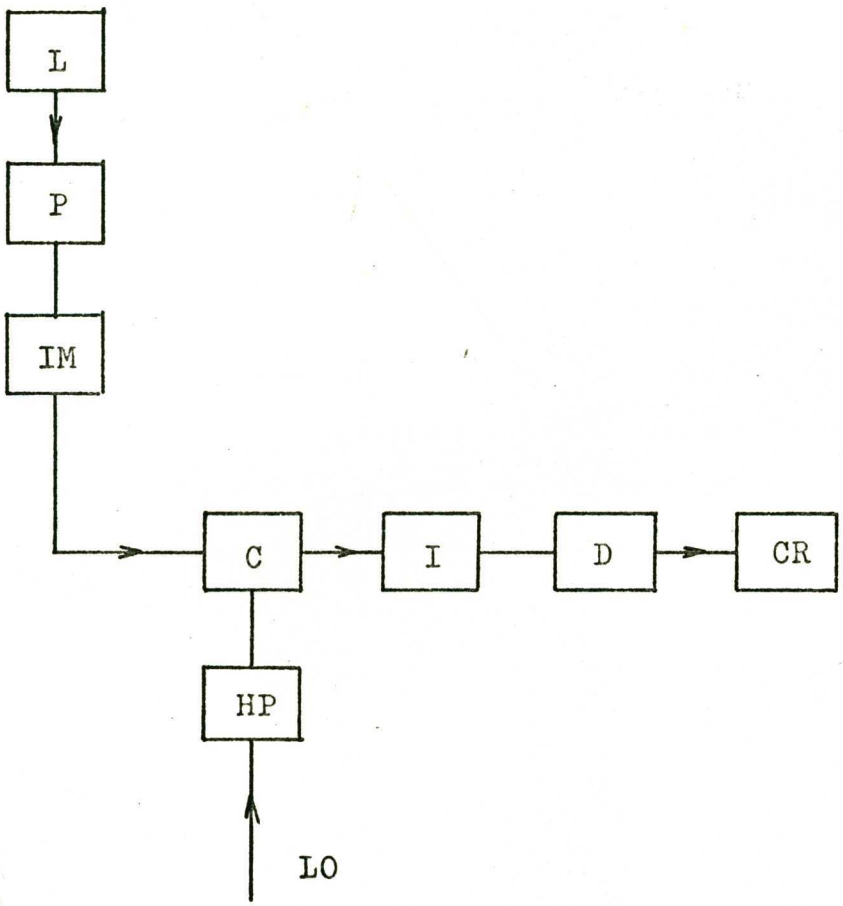

CHAPTER 6.

THE ABSOLUTE FLUX DENSITY MEASUREMENTS.

6.1 Phasing.

The phasing requirements of the I.F receiving system are,

a. The cosine and sine multiplier outputs must be in phase quadrature.

b. The phase difference between the CAL-I and CAL-II system modes of the signal path from hybrid 4 to hybrid 1 must be 90 degrees.

Two methods were used to achieve these requirements.

Method A.

a. The phase difference of 90 degrees between the CAL-I and CAL-II system modes was set by the means of an adjustable phase delay permanently located in the signal path connecting hybrids 4 and 1, a C.W signal generator set at the central I.F frequency of 5.600 MHz and a Hewlett-Packard Vector Voltmeter.

b. The receiving system was set in the CAL-I mode. The cosine multiplier chart recorder deflection produced by the reference aerial modulated diode noise source was set equal to zero by the addition and removal of lengths of cable between hybrids 4 and 5.

c. The system was placed in the CAL-II mode. The adjustable phase delay located between hybrid 5 and the sine multiplier was adjusted until the sine multiplier chart

deflection produced by the reference aerial modulated diode noise source was set equal to zero.

Method B.

a. The phase switch output was divided by a hybrid. One of the hybrid's outputs connected to the hybrid 5 input, the other output connected to the East-West aerial input to hybrid 1. The receiving system was set in the observe mode but the reference aerial coaxial switch was connected to the calibration noise source side. The path length between the additional hybrid's output and the hybrid 5 input was varied until the cosine multiplier chart recorder deflection produced by the reference aerial modulated diode noise source was set equal to zero.

b. An additional phase delay of 90 degrees, measured by C.W signal generator and Vector Voltmeter was inserted into the signal path connecting the additional hybrid's output and the hybrid 5 input. An adjustable phase delay, located between hybrid 5 and the sine multiplier was varied until the sine multiplier chart recorder deflection produced by the reference aerial modulated diode noise source was set equal to zero.

c. Upon restoration of the receiving system to the form used for flux density measurement the CAL-I/CAL-II 90 degrees phase difference may be set by adjustment and measurement using C.W signal generator and Vector Voltmeter or alternatively, by the use of the reference aerial modulated

diode noise source deflections and the known phase quadrature of the cosine and sine multiplier outputs.

The phase adjustment was performed for an insignificant level of noise on the chart recordings. A precision of approximately 0.2 degrees was achieved. A comparison of Methods A and B indicated the presence of small phase anomalies not exceeding several degrees in the phase settings. The use of mixed C.W and I.F noise phase adjustment methods was a possible source of error.

For the absolute flux density measurements the phase difference between the calibration signal voltages at the inputs to hybrids 2 and 5 was adjusted such that the D_{3cal} and the D_{6cal} deflections were set equal to zero, resulting in a simplification of the subsequent flux density calculation. In addition, the zeroed D_{3cal} and D_{6cal} chart recorder responses were used to monitor any drifting out of phase alignment of the I.F system from the division hybrids to the multipliers. No drifting out of phase alignment was noted for the observing sessions.

6.2 Hybrid 1 Power Division Ratios.

The hybrid 1 power division ratios were derived from measurements of the hybrid 1 output voltages resulting from the injection of a 5.60 MHz C.W signal into the appropriate hybrid 1 input. The measurements were repeated using I.F noise obtained from either the East-West aerial or the reference aerial. The C.W measurements were verified.

The power division ratios were, unfortunately, sensitive to the load impedances placed upon the two hybrid 1 outputs. The pads, cables etc located on the hybrid 1 outputs were not disturbed during each observing session.

The power division ratios of hybrids 2, 4 and 5 are assummed to remain constant for the observe/CAL-I/CAL-II system modes. Measurement of the hybrid 2, 4 and 5 power divisions for the observe/CAL-I/CAL-II system modes verified this assumption.

There existed insignificant differences between the values of the hybrid 1 power division ratios for the two observing sessions.

The values of the hybrid 1 power division ratios were,

$$\left(\frac{\eta_1}{\eta_2}\right)\cdot\left(\frac{\eta_{3I}}{\eta_{4I}}\right) = 0.821 \pm 0.002$$

(1)

$$\left(\frac{\eta_{3II}}{\eta_{4II}}\right)\cdot\left(\frac{\eta_{4I}}{\eta_{3I}}\right) = 1.070 \pm 0.003$$

6.3 Time Constant Corrections.

The step function responses of both post-multiplier D.C integrator units were measured by the following procedure.

a. The system was set in the appropriate CAL-I or CAL-II mode. The reference aerial coaxial switch connected to the modulated diode noise source side.

b. For the modulated diode noise switched ON, the synchronous demodulator cutput to the D.C integrator unit was removed for sufficient time to zero the integrator output. The

synchronous demodulator output was re-inserted into the D.C integrator input to produce the step-function response. The chart recorder was run at 320 mm/minute. As a check for the presence of systematic error the procedure was repeated for the diode noise source switched OFF.

The impulse response of a filter is specified by the time derivative of the filter's step-function response. The output voltage of a filter is specified by convolving the input voltage with the impulse response (Bracewell 1965).

The averaged impulse responses for the cosine and sine D.C integrator units were determined by a graphical method of time differentiation of a set of step-function responses. The resulting average impulse responses were convolved with the theoretical point source in-phase interferometer response (undistorted by the time constant) to give the point source in-phase interferometer response after distortion by the post-multiplier integrator units.

There existed insignificant difference between the impulse response for the cosine and sine D.C integrator units.

Fig 6.1 presents the reduction in peak amplitude of the point source in-phase interferometer response for the full aperture East-West aerial due to distortion by the D.C integrator units as a function of declination.

An approximate RC equivalent time constant for the post-multiplier integrator units is 3 seconds.

The total power output time constant was 1 second. The decrease in the total power peak source response due to the 1 second RC time constant was obtained from the graph given by Salomonovich and Kuz'min (1966).

6.4 Phase Switch Efficiency Ratio.

The power losses through the two phase switching positions (0/180 degrees) of the reference aerial section phase switch were unequal.

Designate by α_1 and α_2 the power efficiencies of the phase switch sides that connect into the reference aerial signal path simultaneously with the reference aerial section diode switch biased to the calibration diode noise source and to the fixed matched termination side respectively.

The power efficiency ratio α_2/α_1 was measured to be (for both observing sessions)

$$(2) \qquad \frac{\alpha_2}{\alpha_1} = 1.027 \pm 0.001 \quad .$$

The flux density calculated from equation (12) in Chapter 3 must be reduced by 1.4 percent to correct for the phase switch efficiency inequality.

6.5 Image Responses.

The 122.4 MHz image response was measured, through the reference aerial signal path, to be 24 dB below the 111.2 MHz response.

6.6 Bandpass Corrections.

The I.F frequency bandpass characteristics are determined by the East-West aerial and reference aerial high gain I.F amplifiers located in the phasing hut and the total power signal path I.F amplifier located in the control room. The bandpass characteristics of the three bandpass defining amplifiers are different. Corrections must be applied to the flux density measurements to account for the effects of the differing bandpasses.

Denote the East-West aerial, reference aerial and total power I.F power bandpass characteristics by $B_{EW}(v)$, $B_R(v)$ and $B_T(v)$ respectively, where v is the I.F frequency. The three I.F amplifiers are aligned on the same central frequency, denoted by v_o. The bandpass characteristics are defined such that

$$B_{EW}(v_o) = B_R(v_o) = B_T(v_o) = 1 \qquad (3)$$

Consider the case of the interferometer observing a monochromatic source (I.F frequency v). The time difference in arrival of the source wavefront at the two interferometer aerials is assummed to be zero. The signal path lengths from the two aerials to the cosine multiplier location of multiplication are assummed to be identical. Thus there is no decorrelation due to the "fringe washing" function.

The cosine multiplier synchronous demodulator output voltage, denoted by $V_m(v)$, resulting from the observation of the monochromatic source is given by,

$$V_m(v) \propto (\vec{c}_{EW}(v).\vec{c}_R(v)) \tag{4}$$

where $$\vec{c}_{EW}(v) = c_{EW}(v)e^{j\xi_{EW}(v)}$$

$$\vec{c}_R(v) = c_R(v)e^{j\xi_R(v)}$$

and $$\left|\vec{c}_{EW}(v)\right|^2 = B_{EW}(v)$$

$$\left|\vec{c}_R(v)\right|^2 = B_R(v)$$

At the central frequency v_o

$$c_{EW}(v_o) = c_R(v_o) = 1$$

$$\xi_{EW}(v_o) = \xi_R(v_o) \tag{5}$$

Consider a broadband radiosource. The source flux density is assummed to remain at a constant value across the interferometer bandpasses. The effective areas of the two interferometer aerials are assummed to remain constant across the bandpass

frequency range.

The broadband source cosine multiplier synchronous demodulator output voltage, denoted by V_m, is obtained by integrating $V_m(v)$ across the I.F frequency bandpass i.e

$$V_m = \int_0^\infty V_m(v)dv$$

$$\propto \int_0^\infty \vec{c_{EW}}(v).\vec{c_R}(v)dv \qquad (6)$$

$$= \int_0^\infty c_{EW}(v)c_R(v)\cos(\xi_{EW}(v) - \xi_R(v))dv$$

At the central frequency the East-West aerial and reference aerial source voltages at the location of cosine multiplication are in phase. Moving off the central frequency the voltages decrease in amplitude and are no longer in phase due to phase delay differences between the East-West aerial and reference aerial I.F amplifiers.

Since the amplifiers are constructed to the same design and the bandpass characteristics only display small differences the assumption is made that the relative phase angle, $(\xi_{EW}(v) - \xi_R(v))$, does not deviate significantly from zero across the I.F bandpass.

Therefore $\cos(\xi_{EW}(v) - \xi_R(v)) = 1$

Consequently the following result is obtained,

$$V_m \propto \int_o^\infty \left(B_{EW}(v) B_R(v) \right)^{\frac{1}{2}} dv \tag{7}$$

The bandpass integral for the quadrature calibration deflection D_{2cal} is given by,

$$\begin{aligned} D_{2cal} &\propto \int_o^\infty \overrightarrow{c_{EW}}(v) . \overrightarrow{c_{EW}}(v) dv \\ &= \int_o^\infty B_{EW}(v) dv \end{aligned} \tag{8}$$

The bandpass integrals for the total power deflections D_1 and D_{1cal} are given by,

$$\begin{aligned} D_1 &\propto \int_o^\infty B_{EW}(v) B_T(v) dv \\ D_{1cal} &\propto \int_o^\infty B_R(v) B_T(v) dv \end{aligned} \tag{9}$$

The measured East-West aerial, reference aerial and control room total power I.F amplifier power bandpass characteristics are presented in Fig 6.2. The bandpass integrals were evaluated from the measured bandpasses. The flux densities calculated from equation (12) in Chapter 3, which assume a monochromatic source (at I.F frequency v_o), must be decreased by 0.3 percent to account for the bandpass differences.

6.7 Receiving System Cross-coupling.

The noise temperature increase produced by a transiting radiosource in the East-West aerial exceeds by several orders of magnitude the corresponding noise temperature increase produced in the reference aerial output.

A major source of systematic error would result from cross-coupling between the East-West aerial and reference aerial signal paths in the receiving system ahead of the reference aerial section phase switch. An East-West aerial source voltage coupled into the reference aerial signal path ahead of the phase switch would be phase switched against the East-West aerial inputs to the multipliers and hence would appear as a systematic error in the interferometer output radiosource deflections.

The receiving system was extensively tested for the presence of cross-coupling. Detected cross-coupling effects were removed. The receiving system in its final form exhibited insignificant cross-coupling.

6.8 Calibration Source Selection and Structure.

Potential calibration sources for the 111.2 MHz flux scale were extracted from the following source lists.

a. J.G.Robertson (1972). An all sky catalogue of strong extragalactic radiosources at 408 MHz.

b. Parkes Catalogue (1969).

c. The Mills, Slee and Hill surveys at 85 MHz (1958, 1960, 1961).

d. Culgoora-1 80 MHz catalogue (Slee and Higgins 1973).

The selection criteria were that the sources lack obvious confusing sources, have small diameter East-West brightness distributions so that excessive partial resolution corrections are not required and preferably lie away from the galactic equator in order to minimize confusion by galactic sources.

The total power and interferometer (East-West aerial/ reference aerial) responses of potential calibration sources were recorded in a short observing program. Sources having confused, excessively widened or weak total power and/or interferometer responses were rejected. An examination of published structural data aided the elimination of unsuitable sources.

The East-West aerial has the advantage that any combination of the six component aerial sections may be switched off. This feature allows the right ascension beamwidths to be widened enabling sources exhibiting excessive partial resolution corrections for the full aperture East-West aerial right ascension beamwidths to be observed with reduced aperture i.e using a widened right ascension beamwidth and correspondingly lowered partial resolution corrections.

The sources finally selected as suitable for absolute flux density calibration fall into two categories.

Category I Flux Density Calibrators.

Category I flux density calibration sources were observed using the East-West aerial at full aperture. Table 6.1 lists the Category I sources assumed to have East-West brightness extensions of less than 1 min arc. The remaining Category I sources, 0915-11 and 1648+05, have East-West brightness distributions of greater than 1 min arc extension.

0915-11. Maltby and Moffet (1962) note that the visibility curves obtained from North-South and East-West interferometer baselines at 960 MHz for 0915-11 are difficult to interpret. 0915-11 is described as a core-halo structure. The halo is large, but faint, with a diameter of about 5 min arc. The relative contribution of the halo to the total flux density is given as 12 ± 5 percent at 960 MHz. The East-West core diameter is given as less than 0.6 min arc.

Fomalont (1971) presents the two-dimensional structure of 0915-11 obtained with the Owens Valley Radio Observatory twin-element interferometer at 1425 MHz. Fomalont notes that the precise separation of the 0915-11 emission into large and small diameter components is ambiguous. The source is described as having a core-halo structure. The East-West diameters of the core and halo are given as 47 sec arc and 200 sec arc respectively. The relative contribution of the halo to the total flux density is given as 27 percent at 1425 MHz.

1648+05. Maltby and Moffet (1962) describe 1648+05 at 960 MHz as consisting of two components with a separation of 1.95 min arc along a major axis in position angle 100.5 ± 1.0 degrees, giving an East-West component separation of 1.92 ± 0.10 min arc. The relative intensities of the components are given as 1.4 ± 0.1 and 1. The components are described as circular with equal diameters of 0.75± 0.20 min arc.

Fomalont (1971) describes 1648+05 at 1425 MHz as having two components with an East-West separation of 1.9 min arc. The East-West diameters of the components are given as 25 and 70 sec arc. The relative intensities are given as 1.15 and 1.

Williams et al. (1961) examined the results of interferometer observations of 1648+05 made at the lower frequencies of 81.5, 159, 178 and 408 MHz at the Mullard Radio Astronomy Observatory. At the lower frequencies the components of 1648+05 were found to have nearly equal flux density (within 10 percent) and an East-West separation of 1.95 ± 0.1 min arc.

The partial resolution corrections applying to the East-West aerial full aperture total power and interferometer source responses for the source brightness distribution models given above for 0915-11 and 1648+05 were calculated. The overall partial resolution corrections applied to the flux densities calculated from the expression derived for a non-extended source (equation (12) Chapter 3) for both 0915-11 and 1648+05 were negligible.

Table 6.1

Category I Flux Density Calibration Sources.

(a) East-West extensions less than 1 min arc.

Source	Structure	Structure Data Reference
0624-05	15 sec arc EW 0± 10 sec arc NS	Fomalont and Moffet (1971), 1425 MHz.
1932-46	0.7 x 0.3 min arc P.A 110 ± 30°	Ekers (1969) 1403 MHz.
2211-17	Double structure Separation 83 ± 5 sec arc P.A 164 ± 5° Component diameters 25 sec arc EW 40 sec arc NS	Fomalont (1971), 1425 MHz.

(b) East-West extensions greater than 1 min arc.

Source: 0915-11, 1648+05

Category II Flux Density Calibrators.

Category II flux density calibration sources were observed with reduced East-West aerial aperture. Table 6.2 lists the Category II sources, East-West aerial sections switched ON, total power and interferometer (in-phase) half power East-West beamwidths and the East-West widths to half intensity of the assumed source brightness distribution models.

Table 6.3 lists the percentage reduction in the total power and interferometer (in-phase) responses due to partial resolution. Listed in the fourth column of Table 6.3 is the overall structure correction factor.

The source flux density calculated from equation (12) of Chapter 3 must be multiplied by the overall structure correction factor to correct the flux density for the reduction in the total power and interferometer source responses due to partial resolution.

The brightness distribution model used for 0531+21 was the integrated East-West brightness distribution measured by Mills (1953) at 101 MHz. The overall structure correction factor for 0531+21 is small. Consequently the flux density measurement does not depend critically on the assumed source brightness distribution model.

Costain et al. (1976) examined the available information on the 1228+12 source structure. 1228+12 is described as a core-halo structure. The core angular diameter is less than 1 min arc. Costain et al. note that the high resolution

mappings of 1228+12 at 80 MHz (Lockhardt 1971), 408 MHz (Cameron 1971) and 1420 MHz (Costain et al. 1976) show a halo elongated in position angle 34 degrees and of overall extent 16 x 12 min arc.

The relative contribution of the halo to the total flux density at the three frequencies is different consisting of 70 percent, 60 percent and 40 percent of the total flux density at 80, 408 and 1420 MHz respectively. These halo flux density contributions indicate a halo contribution to the total flux density of approximately 68 percent at 111 MHz.

Costain et al. comment that the 80, 408 and 1420 MHz halo mappings indicated no significant changes in overall angular size or structure of the halo over the 80 to 1420 MHz frequency range.

The brightness distribution model used to calculate the partial resolution corrections for 1228+12 was the integrated East-West brightness distribution measured by Mills (1953) at 101 MHz. For 1228+12 the overall structure correction factor does not depend critically on the fine details of the assumed East-West brightness distribution model.

Table 6.2

Category II Source Observation.

Source	East-West Aerial Sections ON.	East-West Half-power Beamwidth. (min arc)		Source East-West Half-intensity Width (min arc).
		Total Power	Interferometer (in-phase)	
0531+21	17E, 17W 49E, 49W	7.2	9.7	4.0
1228+12	17E,17W	14.0	18.8	4.6

Table 6.3

Partial Resolution Reductions and Corrections.

Source	Partial Resolution Source Response Reduction (Percent)		Overall Structure Correction Factor
	Total Power	Interferometer (in phase)	
0531+21	12.4	6.8	1.010
1228+12	6.5	3.5	1.004

6.9 Linearity Testing.

The expression for flux density given by equation (12) of Chapter 3 assumes that the receiving system is linear.

The linearity characteristics of the signal path from the hybrid 1 output to the total power chart recorder output was examined by the following procedure.

a. The receiving system was set in the CAL-I or CAL-II mode. The coaxial switch was biased to the diode noise source side. The noise level at the hybrid 1 total power output was adjusted to the level pertaining at the hybrid 1 total power output for the receiving system set in the observe mode and the coaxial switch biased to the sky. The procedure for obtaining the noise level equalization was explained in Chapter 3. The total power chart recorder position consequently corresponds to the OFF source baseline.

b. The noise output of the unmodulated reference aerial diode noise source was not altered subsequent to step a.

c. A D_{1cal} (or D_{4cal}) deflection for a fixed modulated diode noise source current meter reading was superimposed upon the total power chart recorder baseline defined in step a.

d. Additional noise was added to the hybrid 1 total power output from the East-West aerial. This was achieved by increasing the gain of the remotely controlled amplifier located in the East-West aerial signal path ahead of hybrid 1.

A D_{1cal} deflection resulting from the same fixed diode current meter reading as applied for step c was superimposed upon the newly defined total power chart recorder level. The values of the D_{1cal} deflection and the additional East-West aerial noise level increase were selected such that the range of noise levels encountered at the total power output of hybrid 1 for source observation and calibration was covered.

Let $\triangle T$ represent an increase in the hybrid 1 total power output noise temperature above the level defined in step a. Define D as the total power chart recorder deflection, measured from the baseline defined in step a, resulting from the noise temperature increase $\triangle T$.

An approximate relationship between D and $\triangle T$ is,

$$D = C(\triangle T)^{\alpha} \qquad (10)$$

where C is a constant and α describes the linearity characteristic.

The linearity test procedure outlined above provides sufficient information for the evaluation of α. The linearity procedure is independent of non-linearities inherent in the diode noise generator or present in the signal path connecting the coaxial switch and hybrid 1.

The linearity characteristic from the coaxial switch to the chart recorder output of the total power section was examined by

a closely similar procedure. In this situation the noise level from the East-West aerial remains unchanged during the investigation.

D_{1cal} deflections for a fixed value of the modulated noise source diode current meter reading are recorded for noise added or removed by the adjustment of the noise output of the reference aerial unmodulated diode noise source to cover the range of noise levels encountered for source observation and calibration.

The combination of the two non-linearity measurement procedures described above allow the examination of the linearity in the signal path connecting the coaxial switch and the input to hybrid 4.

The following method was used to examine the linearity of the signal path from the coaxial switch to the cosine and sine multiplier chart recorder outputs.

D_{2cal} and D_{3cal} deflections were recorded for a fixed value of modulated diode noise source current meter reading. The output of the reference aerial unmodulated diode noise source was raised and lowered to cover the range of noise levels encountered for source observation and calibration.

The linearity of the multipliers for two different non-zero values of the modulated diode noise source current meter readings was examined by the following procedure.

a. The total power D_{1cal} (or D_{4cal}) deflections for the two different non-zero values of modulated diode noise source

current meter readings were recorded. The D_{1cal} deflection ratio obtained for the two values of diode current was corrected for non-linearity in the signal path from the output of hybrid 1 to the total power recorder output.

b. If there are no departures from linearity in the signal paths connecting the outputs of hybrid 4 to the cosine and sine multiplier chart recorder outputs the D_{2cal} (or D_{3cal}) deflection ratio recorded simultaneously with the D_{1cal} ratios in part a. should equal the D_{1cal} ratio corrected for non-linearity as described in part a, since the non-linearity corrected D_{1cal} ratio should be the same at hybrid 4 as for hybrid 1.

In practice, no significant departures from linearity was measured from the hybrid 4 outputs to the cosine and sine multiplier chart recorder outputs.

The conclusions of the extensive investigations of departures from non-linearity in the absolute flux density measurement receiving system were as follows.

a. No corrections for non-linearity are required for the D_2, D_3, D_{2cal}, D_{3cal}, D_{5cal} and D_{6cal} deflections for all of the flux density calibration source measurements.

b. The D_1 deflection required correction for non-linearity in the signal path between hybrid 1 and the total power

recorder output. The D_{1cal} and D_{4cal} deflections required corrections for non-linearity in the signal path between the coaxial switch and the total power chart recorder output. The corrections for non-linearity applied to the total power deflections were less than/equal to 1 percent.

It is not essential to the absolute flux density measurements that the East-West aerial receiving system ahead of the input to hybrid 1 is linear. The linearity of the East-West aerial receiving system is examined in Chapter 7.

6.10 I_{LO}, I_{HI} Noise Temperatures.

The output noise temperature of the reference aerial calibration diode noise source was calibrated against the liquid nitrogen load output noise temperature for a fixed diode current meter reading of 1.00 mA.

Calibration of the interferometer source responses required a noise diode current reading of less than 1.00 mA. Adequate calibration of the total power source responses required a noise diode current reading in excess of 1.00 mA.

The absolute flux density observing records were calibrated with the calibration diode noise operating at the same two fixed values of diode current meter reading for all the sources.

The output noise temperatures of the calibration diode noise source corresponding to the low and high currents (measured relative to a 1.00 mA current meter reading) were obtained by relative measurement to the absolutely calibrated 1.00 mA diode current reading noise temperature.

The relative measurements were on the receiving system's total power output and the multiplier outputs. The receiving system was examined for departures from non-linearity during the relative noise temperature measurement experiment. Slight corrections ($\leq$ 1 percent) were applied to the noise temperature ratios to correct for the presence of non-linearity.

The measured high (I_{HI}) and low(I_{LO}) diode current meter reading noise temperatures were,

$$I_{LO} = 50.3 \pm 1.2 \quad {}^{o}K$$

(11)

$$I_{HI} = 1276 \pm 26 \quad {}^{o}K$$

The quoted standard errors are due solely to the experimental scatter of the noise temperature ratios and do not include the uncertainty in the absolute calibration of the 1.00mA diode current noise temperature.

6.11 Beamshapes.

Figs 6.3, 6.4 and 6.5 display the ideal in-phase and quadrature East-West relative power patterns for the correlation interferometer consisting of the East-West aerial and the reference aerial for the following conditions.

a. All East-West aerial sections ON.

b. 81E, 81W East-West aerial sections OFF, 49E, 17E, 17W and 49W ON.

c. East-West aerial sections 17E, 17W ON only.

The effect of the central 4.7 wavelength gap in the East-West aerial aperture as compared to the relative power pattern for a completely filled East-West aerial aperture is to systematically raise and lower sections of the interferometer relative power pattern. This effect introduces a slight bias into the determination of the baseline in the vicinity of the primary source response. For each flux density calibration source the interferometer phase angle was calculated from the cosine and sine multiplier responses. The ideal relative power patterns were calculated and examined for bias effects in the source response baseline determination procedure.

No corrections were applied to the measured flux densities for baseline bias due to the smallness of the effect (≤ 1 percent) and the divergence of the real interferometer relative power patterns (refer to Figs 6.7 to 6.13) from the ideal beamshapes.

The measured North-South normalized total power pattern of the East-West aerial is given in Fig 6.6.

6.12 Atmospheric Attenuation.

In the frequency range 0.1 GHz to 1.0 GHz atmospheric attenuation is mainly due to neutral oxygen. The atmospheric attenuation due to water vapour is slight in comparison to the attenuation due to oxygen.

Howell and Shakeshaft (1967) compare theory and observation for atmospheric attenuation in the frequency range 0.4 GHz to 1.0 GHz. Howell and Shakeshaft measured the zenithal atmospheric attenuation at 0.4 percent at 408 MHz, in agreement with theoretical curves (Hogg 1959, Croom 1964).

Westman (1968) presents curves for the differential absorption coefficients of oxygen and water vapour in the frequency range 0.1 GHz to 1.0 GHz.

Combining Howell and Shakeshaft's atmospheric attenuation measurement at 408 MHz with the Westman curves the zenithal atmospheric attenuation due to oxygen at 111 MHz was estimated at 0.04 percent. Consequently the atmospheric attenuation at 111 MHz due to oxygen and water vapour is insignificant.

6.13 Observing Procedure.

The absolute flux density measurements were made during March and April 1976 in separate observing sessions.

The observation of 1932-46 was limited during the March 1976 observing session due to a 408 MHz observing project operational on the Molonglo Cross during the 1932-46 transit. The observation of 0531+21 and 2211-17 was severely limited during the March observing session due to the commencement of a solar noise storm on March 26 which rendered absolute flux density measurement impossible when the sun was above the horizon during most of the March observing session.

Nine percent of the night time observations during March and April were rejected due to severe distortion of the total power and interferometer source responses by ionospheric scintillation.

At the commencement of each observing session the following receiving system measurements and test procedures were carried out.

a. The reference aerial dipole was orientated in the correct North-South and horizontal alignment.

b. The dipole-reflector separation was adjusted to optimize the reflection match. The reference aerial reflection match was measured at the dipole feed cable output and at the pre-amplifier input to ensure a reflection match better than -30 dB. The dipole-reflector separation was recorded.

c. The dipole feed cable loss was measured.

d. The reflection matches of the reference aerial diode noise sources for the two bias positions of the diode switch were measured at the pre-amplifier input. The reflection matching was equal to or better than -30 dB.

e. The I.F bandpasses of the I.F bandpass defining amplifiers were measured. The East-West aerial and reference aerial I.F bandpasses were aligned with the central frequency of the control room total power I.F bandpass (5.60 MHz). The I.F bandpass shapes were examined.

f. The interferometer cosine and sine multiplier outputs were set in phase quadrature. The quadrature phasing of the CAL-I/CAL-II receiving system modes was set.

g. The hybrid 1 power division ratios were measured.

h. The local oscillator frequency was measured.

i. The AGC usually operative on the total power receiving system was switched OFF.

j. The receiving system I.F noise levels were measured to check that the receiving system was operating in the vicinity of levels set and expected from previous investigations.

In the intervals between flux density calibration source observations the receiving system was extensively examined for departures from non-linearity. The intervals were also used to obtain drift scans for later analysis to enable the evaluation of the r.m.s confusion errors on the interferometer and total power source observations.

The observing procedure was the same for all the flux density calibration sources i.e a preceding calibration, the source responses and a following calibration.

In greater detail,

Observing Procedure.

$$D_{1cal},\ D_{4cal},\ \begin{matrix} D_{5cal} \\ D_{6cal} \end{matrix},\ \begin{matrix} D_{3cal} \\ D_{2cal} \end{matrix}\ \text{SKY OBSERVE}\ \begin{matrix} D_{3cal} \\ D_{2cal} \end{matrix},\ \begin{matrix} D_{5cal} \\ D_{6cal} \end{matrix},\ D_{4cal},\ D_{1cal}$$

Each deflection was recorded twice, yielding a total of four deflections for each type of calibration deflection (e.g D_{1cal}) per observation.

The duration of the sky drift scan for the Category I flux density calibration sources was 30sec δ minutes where δ is the source and East-West aerial pointing declination. The expected source transit time was 15 sec δ minutes after the start of the drift scan.

The sky observe duration for 0531+21 was 40 minutes and for 1226+12 was 60 minutes.

There was insufficient time between the completion of the 0531+21 following calibration and the commencement of the 0624-05 sky drift to allow the application of a preceding set of calibration deflections for 0624-05.

Figs 6.7 to 6.13 show typical total power and interferometer source responses obtained for the seven flux density calibration sources.

6.14 Data Reduction Procedure.

All the 111 MHz flux density calibration records were reduced by hand.

a. Category I Sources.

a.1 Total Power Records.

Inspection of the 0915-11 East-West total power source response, for which the effects of system noise and confusion are slight, indicated that zeroes in the full aperture East-West power pattern could be expected 2.5 half-power beam-widths (HPBWs) preceding and following the peak source response.

The total power baselines for all Category I sources were determined from minima of the total power record in the neighbourhood of the points preceding and following the peak response by 2.5 HPBWs. The length of total power record in the neighbourhood of the 2.5 HPBW points over which the most negative deflection was sought did not exceed a half HPBW excepting 1932-46, in which case the presence of large back-ground gradients resulted in the following minima of the total power record lying closer in to the peak response.

The maximun of the total power source response was determined by the method of bisected chords. The total power source deflection was measured from the baseline connecting the expected power pattern zeroes determined in the neighbourhood of the preceding and following 2.5 HPBW points.

a.2 Interferometer Records.

A 4.5 min time section of the observation centred on the primary source response was excluded from the baseline measurement procedure for the cosine and sine interferometer records.

Deflections of the interferometer records, relative to an arbitrary zero, were measured every 15 seconds on the non-excluded preceding and following sections of the cosine and sine interferometer sky observation records.

The average of the preceding and following baseline deflections determined the baseline in the vicinity of the primary source responses.

The effect of the 3 second time constant on an interferometer in-phase source response is to reduce the amplitude of the peak response and to delay the attainment of the peak response on the interferometer in-phase record by approximately 3 seconds. The total power time constant was 1 second.

The expression for source flux density given by equation (12) of Chapter 3 assumes negligble time constant distortion of the source responses and simultaneous measurement of the source's total power and interferometer responses.

To satisfy the simultaneous measurement condition in the presence of time constant caused source response time delays the interferometer source deflections were measured 2.0 seconds following the time of maximun attainment of the total power response.

b. Category II Sources.

Confusion and system noise are negligible on the Category II source total power records. Negligible uncertainty is introduced into the determination of the baseline under the peak source response by the linear interpolation of the background measured away from the main source response.

The measurement of the source responses, baseline deflections and calibration deflections for the total number of flux density observations required the measurement of 28,000 deflections.

6.15 Confusion Error on the Interferometer Recordings.

The output of an interferometer has a confusion error due to the presence of a population of numerous unresolved radio sources in the reception pattern.

The error due to confusion and noise for a discrete source interferometer response at a particular point on the interferometer record is the deflection that would be observed at that point if the discrete source were removed.

The combined confusion, system noise, interference, scintillation, short term gain and phase instability error distribution can be determined directly by the measurement of the deflections of an interferometer drift scan at a set of independent points.

This was done at 111 MHz for the full aperture East-West

aerial/reference aerial correlation interferometer. Six drift scans from right ascension 0955 to 1125 with the East-West aerial directed to declination 11 degrees South were recorded. The interferometer phasing was similar for each observation.

An interferometer record deflection measurement procedure similar to the procedure used to determine the baseline and the source deflection relative to the baseline for the absolute flux density measurements was applied to the interferometer drift scans at points spaced every 30 seconds. The interferometer East-West relative power pattern HPBW at declination 11 degrees South was 29 seconds of time.

The sensitivity of the interferometer records did not allow the noise contribution to the combined confusion and noise error distribution to be neglected. To obtain an estimate of the r.m.s confusion error the following procedure was adopted to separate the r.m.s confusion error from the combined confusion and noise r.m.s error.

Consider the ideal situation of two noise free drift scans of the same strip of sky obtained by the same interferometer under identical receiving system gain, phase and aerial pointing conditions. The interferometer is assumed to be completely free of gain and phase instabilities with the complete absence of interference and scintillation. The only error contribution on the interferometer records is the confusion error.

If the interferometer record deflections measured for corresponding independent sample points on the two ideal drift scans are plotted against each other on (x,y) Cartesian axes

the deflections will be in perfect correlation with all the data points lying on the regression line y = x, since the confusion error deflection at corresponding sample points on the two ideal interferometer records is the same. It is assumed that there exists no measurement error in the interferometer records deflections.

Define the (X,Y)co-ordinate axes as the axes resulting from a counter-clockwise rotation of 45 degrees of the (x,y) axes.

The parent distribution of the data point X-co-ordinates should be symmetrical about the X-origin. Denote the standard deviation of the data point X co-ordinate distribution by σ_F.

Consider the case of two drift scans of the same strip of sky obtained by the real interferometer having a combined confusion and noise error distribution present on the drift scan. The interferometer record deflections measured for corresponding independent sample points on the two real drift scans plotted against each other on (x,y) axes are scattered about the regression line y = x (i.e Y = 0) due to the presence of noise.

The parent distribution of the real interferometer data point Y co-ordinates is symmetrical about the Y origin. Denote the standard deviation of the parent distribution of data point Y co-ordinates by σ_N. The standard deviation σ_N arises solely from random noise on the interferometer records.

In the absence of a confusion error the standard deviation of the data point X co-ordinate parent distribution would be σ_N (by symmetry with the Y co-ordinates). The X co-ordinate parent distribution would be symmetrical about the X axis.

In the presence of the confusion error the data point X co-ordinate distribution is the convolution of a confusion error distribution with the X co-ordinate noise error distribution.

The standard deviation of the resulting data point X co-ordinate parent distribution, denoted by σ_{NC}, is given by

$$\sigma_{NC}^2 = \sigma_N^2 + \sigma_F^2 \qquad (12)$$

The r.m.s confusion error present on the interferometer records, denoted by σ_C, is related to σ_F by

$$\sigma_C = \frac{1}{\sqrt{2}} \sigma_F \qquad (13)$$

Hence the following expression for σ_C results

$$\sigma_C = \frac{1}{\sqrt{2}} \left(\sigma_{NC}^2 - \sigma_N^2 \right)^{1/2} \qquad (14)$$

In practice, the six drift scans were divided into pairs. For each pair of drift scans the interferometer deflection scales (Jy/cm) were equalized by using a simple relationship existing between the absolute flux density calibration

deflections and the East-West aerial calibration deflection applied at the commencement and termination of each drift scan. The calibration to convert the interferometer deflections to units of flux density was obtained from the observation of 0915-11 which preceded each drift scan. The calibration source was observed under closely similar total power and interferometer gain and phase conditions to the drift scans.

Fig 6.14 shows interferometer deflections measured for corresponding independent sample points on a pair of drift scans (with equalized deflection scales) plotted against each other on (x,y) axes.

Fig 6.15 presents the histograms of the data point X co-ordinates and Y co-ordinates obtained from Fig 6.14. Both Figs 6.14 and 6.15 clearly show the presence of a confusion error distribution.

Analysis of the six drift scans gave the following estimate for the r.m.s confusion error on the full East-West aerial/reference aerial correlation interferometer output record for the strip of sky scanned,

(15) $$\sigma_C = 7.8 \pm 1.6 \text{ Jy}$$

The minimun reliable flux density (Sr) of a phase-switched interferometer in the presence of confusion is given by Mills and Slee (1957) as

$$S_r = 9\,(\Omega_c/4\pi)^{2/3}\, S_o \tag{16}$$

where

$$\Omega_c = \iint_{4\pi} F^2\, d\Omega$$

where F is the normalized power response of the interferometer in the direction of $d\Omega$. S_o is the flux density obtained by extrapolating the log N-log S relation to N = 1 at the observing frequency.

For the 111 MHz interferometer Sr is understood to be three times the r.m.s confusion error of the interferometer output signal. Therefore,

$$\sigma_c = 3\,(\Omega_c/4\pi)^{2/3}\, S_o \tag{17}$$

For the 111 MHz interferometer

$$\Omega_c = 1.054 \times 10^{-3}\ \text{rad}^2$$
$$S_o = 1.706 \times 10^{3}\ Jy \tag{18}$$

where Ω_c was obtained from the measured normalized power pattern of the interferometer and S_o was obtained from the 85 MHz

value of S_o (Mills and Slee 1957) and a spectral index of 0.8.

The value of σ_c calculated from equation (17) was

(19) $$\sigma_c = 9.8 \text{ Jy}$$

The observed and theoretically estimated r.m.s confusion errors are not in major disagreement. Considering the approximate nature of both estimates the closeness of agreement may be fortuitous.

6.16 Confusion Error on the Total Power Recording.

The total power radiotelescope output fluctuates due to many confusion sources passing through the beam.

Total power record deflections for a sky drift scan from

right ascension 0955 to 1125 hours at declination -11^{o} were measured at points spaced at HPBW intervals.

A deflection measurement procedure closely similar to the procedure used for the absolute flux density measurements was used to determine baselines and the deflections relative to the baseline (Category I source total power measurement procedure).

Fig 6.16 presents the measured total power record confusion and noise error distribution. The sensitivity of the total power record was very good. Comparison of the total power sky drift scans for the same strip of sky obtained on successive days indicated negligible day to day changes in the shape of the background. The good sensitivity and the day to day stability of the total power response allowed the assumption that the noise error contribution to the combined confusion and noise error distribution could be taken as negligible. Consequently the Fig 6.16 distribution was taken to be exclusively due to the confusion error. The deflection/flux density scale for Fig 6. was calibrated from the preceding observation of 0915-11.

The measured full East-West aerial total power confusion error, denoted by σ_T, was

(20) $$\sigma_T = 5.4 \pm 0.8 \text{ Jy}$$

Condon, Neill and Jauncey (1971) give the following expression for the r.m.s confusion flux density error for a total

power telescope,

$$(21) \qquad \sigma_T = C.\ \lambda^{0.7} \cdot \Omega_b^{2/3}$$

where σ_T is the r.m.s width of the gaussian portion of the confusion flux density error distribution, λ is the observing wavelength, Ω_b is the beam area to half-power width (arc min)^2 and C is a "universal constant" (4.3×10^{-3}). Condon, Neill and Jauncey (CNJ) determined the value of C from total power confusion flux density error distributions measured at 318 and 606 MHz with the Arecibo reflector. The method used for baseline determination for the Molonglo 111 MHz measurements was similar to the CNJ method. No corrections were applied to the CNJ expression for σ_T to account for differences in baseline determination methods.

For the Molonglo full aperture East-West aerial at 111 MHz

$$(22) \qquad \Omega_b = 1.84 \times 10^4 \ \text{(arc min)}^2$$

The CNJ expression for σ_T yields

$$(23) \qquad \sigma_T = 6.0 \ \text{Jy}$$

which compares favourably with the observed value.

6.17 Confusion and Random Noise Error Bias.

Wyllie (1968) noted that the flux density values derived from the application of the equations for flux density of Wyllie methods I and II are overestimates of the true flux densities. The bias is present in the 111 MHz absolute flux density calibration method even if D_2, D_3 and D_{2cal} are influenced only by random error.

For a single observation the cosine multiplier chart recorder source deflection can be expressed as

$$(24) \qquad D_2 = A_2 \pm \sigma_2$$

where σ_2 is the combined confusion and random noise error and A_2 is the cosine multiplier chart recorder source deflection in absence of confusion and random noise on the cosine multiplier chart record.

Similarly,

$$(25) \qquad (D)^{\frac{1}{2}}.D_3 = A_3 \pm \sigma_3$$

Squaring and adding

$$(26) \quad D_2^2 + D.D_3^2 = A_2^2 + A_3^2 + \sigma_2^2 + \sigma_3^2 \pm \epsilon_1$$

where ϵ_1 is a random error, $(D_2^2 + D.D_3^2)$ is overestimated by the amount $(\sigma_2^2 + \sigma_3^2)$.

The full aperture interferometer confusion error was evaluated at 7.8 Jy in Section 6.15. For more complex regions of the sky the 7.8 Jy value of confusion error is undoubtably an underestimate. If σ_{2N} is the random noise error on the cosine multiplier chart recording for the receiving system set in the observe mode and if the measurement of D_2 involved smoothing by eye at the time of source transit over N time constants on the chart record then σ_2 is related to the confusion and random noise errors approximately by

$$(27) \qquad \sigma_2 = \left(7.8^2 + \frac{2}{N} \cdot \sigma_{2N}^2 \right)^{\frac{1}{2}}$$

Similarly

$$(28) \qquad \sigma_3 = \left(7.8^2 + \frac{2}{N} \cdot \sigma_{3N}^2 \right)^{\frac{1}{2}}$$

The calibration deflection D_{2cal} may be expressed

$$(29) \qquad D_{2cal} = A_4 \pm \sigma_4$$

where σ_4 is the r.m.s error in the measurement of D_{2cal} due to random noise on the cosine multiplier calibration record and A_4 is the value of the D_{2cal} deflection in the absence of record noise.

Squaring D_{2cal}

$$(30) \qquad D_{2cal}^2 = A_4^2 + \sigma_4^2 \pm \epsilon_2$$

where ϵ_2 is a random error, D_{2cal}^2 is overestimated σ_4^2.

In practice, σ_{2N} and σ_{3N} were evaluated from the interferometer records for each calibration source, σ_2 and σ_3 were evaluated for $N = 5$. The dominant contribution to σ_2 and σ_3 for all the flux density calibration sources was the confusion error. The bias produced in D_{2cal} by σ_4 was negligible. The individual source correction factors for confusion and noise error bias are listed in Table 6.5.

6.18 Results of the Absolute Flux Density Measurements.

Table 6.4 lists the flux density correction factors common to all the flux density calibration sources. The flux density values calculated from equation (12) of Chapter 3 were multiplied by the correction factors.

Table 6.5 lists the flux density correction factors peculiar to each calibration source.

Table 6.4

Common Flux Density Correction Factors.

Correction Origin	Correction Value
Phase-switch Efficiency Ratio.	0.987
I.F Bandpass	0.997

Table 6.5

Individual Flux Density Correction Factors.

Origin Source	Time Constant	Source Structure	Non-Linearity	Cal Phase Error	Confusion Noise Bias
0531+21	1.016	1.010	1.009	0.994	1.000
0624-05	1.037	-----	1.007	0.996	0.988
0915-11	1.036	-----	1.007	0.994	0.999
1228+12	1.004	1.004	1.009	0.996	1.000
1648+05	1.038	1.002	1.007	0.995	1.000
1932-46	1.014	-----	1.007	0.992	0.987
2211-17	1.031	-----	1.009	0.992	0.992

Table 6.6 lists the absolute flux density measurements.

Column 1 lists the source.

Column 2 gives the number of independent observations for each source.

Column 3 gives the absolute flux density.

Column 4 lists the random component of the r.m.s flux density error due to combined effect of system noise, interference, ionospheric scintillation, short term gain and phase fluctuations. This error was assessed from the scatter of the absolute flux density measurements for each source. This error source reduces by $\sqrt{N}$ where N is the number of independent observations.

Column 5 lists the r.m.s confusion error assessed from the confusion error measurements discussed in Sections 6.15 and 6.16. The confusion errors for the Category II sources were scaled from the full aperture confusion error measurements using the beam pattern dependence of equations (17) and (21).

Column 6 gives the total r.m.s error which is the square root of the quadratic sum of the r.m.s random error, r.m.s confusion error, r.m.s error in the reference aerial effective area (4 percent), r.m.s error in the thermal calibration of the absolute scale (3 percent) and the small r.m.s errors ($\leq$ 2 percent) in the I_{LO}, I_{HI} ratios and the common and individual flux density correction factors.

Table 6.6

111 MHz Absolute Flux Density Measurements.

(1)	(2)	(3)	(4)	(5)	(6)
Source	Number of Observations.	Absolute Flux Density. (Jy)	R.M.S Random Error. (Percent)	R.M.S Confusion Error. (Percent)	Total R.M.S Error. (Percent)
0531+21	13	1633	3.3	1.3	6.4
0624-05	13	112.5	5.2	14.1	15.9
0915-11	15	465.3	2.3	3.8	6.9
1228+12	15	1696	2.3	2.0	6.1
1648+05	17	822.5	3.4	2.6	6.8
1932-46	11	118.5	9.0	15.2	18.4
2211-17	13	128.0	6.7	11.2	14.1

6.19 Western Arm Reflection and Re-radiation Experiment.

1. The reference aerial was positioned 12.9 wavelengths North of the Western arm of the Molonglo Cross. An experiment was designed to determine whether there was a significant amount of radiation being received indirectly from the source under calibration by the reference aerial originating from,

(i) Reflection from the Western Cross arm surface.

(ii) Diffraction or re-radiation from the Western arm feed dipoles and the feed support mechanical structure.

2. Selected calibration sources were observed in the following manner.

(i) The Western arm I.F amplifiers were switched off for the entire experiment. The Western arm therefore no longer contributed significantly to the total power output.

(ii) Several sections of the Eastern arm had their I.F amplifiers switched off in order to widen the East-West beamwidth for the observation of extended sources. This procedure was not essential to the experiment but increases the usefulness of the observations for other purposes. The Eastern arm I.F amplifiers were switched off as follows.

Source	Eastern Arm Section OFF.
0531+21	81 E
1228+12	81, 49 E
0915-11	No Eastern Section OFF

3. Each source was observed with the the Western arm directed at either the source or the zenith for alternate source transits. The Eastern arm was always directed at the source transit declination. If a significant amount of reflected and re-radiated radiation were received from the source at the reference aerial for the situation where the Western arm was directed at the source transit declination, then it would be expected for the Western arm directed towards the zenith during source transit that the reflected and re-radiated electric vector components received at the reference aerial would be diminished in amplitude and changed in phase. The ratios of the flux densities obtained for each source by the usual method of flux density measurement using the Eastern arm and the reference aerial for the two Western arm pointing positions should set upper limits to the possible effect of Western arm radiation and re-radiation on the flux density determination for each source declination.

4. Results. The Western arm radiation and re-radiation experiment was carried out over 9 consecutive days in December 1975. Seventeen percent of the observations were rejected due to severe ionospheric distortion of the total power and interferometer source responses.

The flux density ratios for the Western aerial pointing positions were,

a. 0531+21

$$\frac{\text{Flux Density (Western arm at Dec } +19^{\circ})}{\text{Flux Density (Western arm at zenith)}} = 1.01 \pm 0.14$$

b. 0915-11

$$\frac{\text{Flux Density (Western arm at Dec } -11^{\circ})}{\text{Flux Density (Western arm at zenith)}} = 1.07 \pm 0.09$$

c. 1228+12

$$\frac{\text{Flux Density (Western arm at Dec}+12^{\circ})}{\text{Flux Density (Western arm at zenith)}} = 0.94 \pm 0.08$$

The source 1648+05 was not observed due to the proximity of sun in right ascension. The results are consistent with the absence of significant reflection and re-radiation effects from the Western arm, although, in view of the large standard errors in the flux density ratios it would be going beyond the evidence to assume the effect is completely absent.

FIG. 6.1 . THE REDUCTION IN PEAK AMPLITUDE OF THE POINT SOURCE IN-PHASE INTERFEROMETER RESPONSE FOR THE FULL APERTURE EAST-WEST AERIAL DUE TO DISTORTION BY THE D.C INTEGRATOR UNITS EXPRESSED AS A FUNCTION OF DECLINATION.

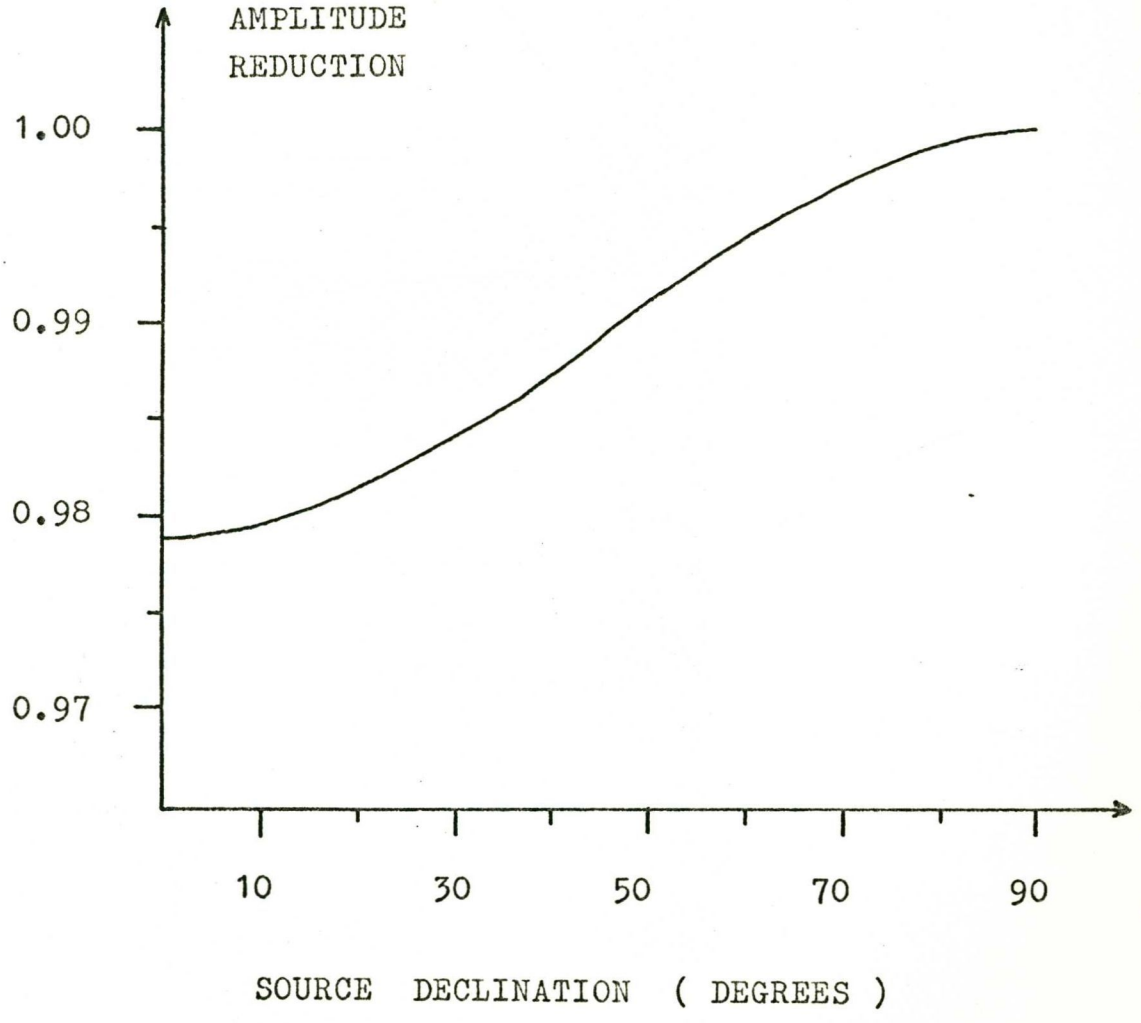

FIG. 6.2 . I.F POWER BANDPASSES.

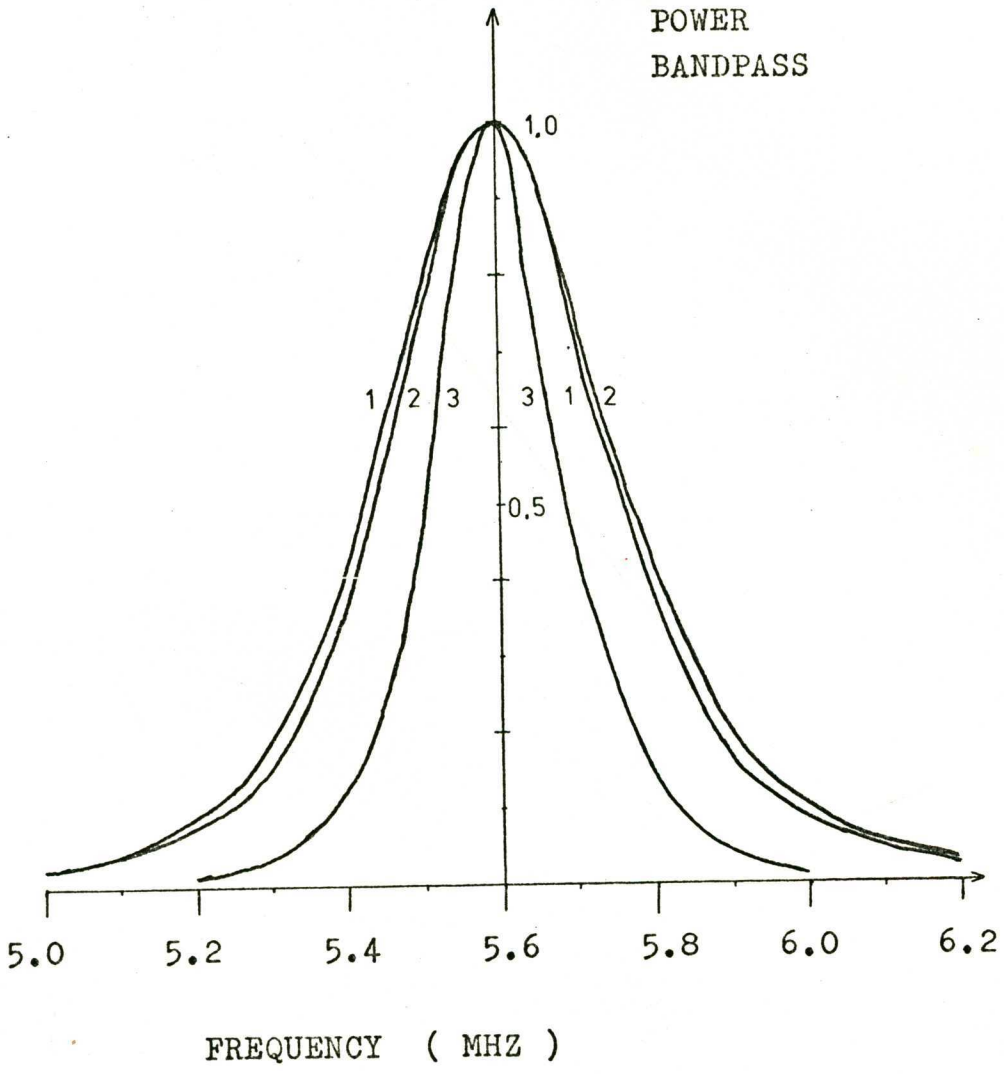

CODE.

1 : $B_R(v)$

2 : $B_{EW}(v)$

3 : $B_T(v)$

FIG. 6.3 .

IDEAL INTERFEROMETER EAST-WEST RELATIVE POWER PATTERN.

ALL EAST-WEST AERIAL SECTIONS ON .

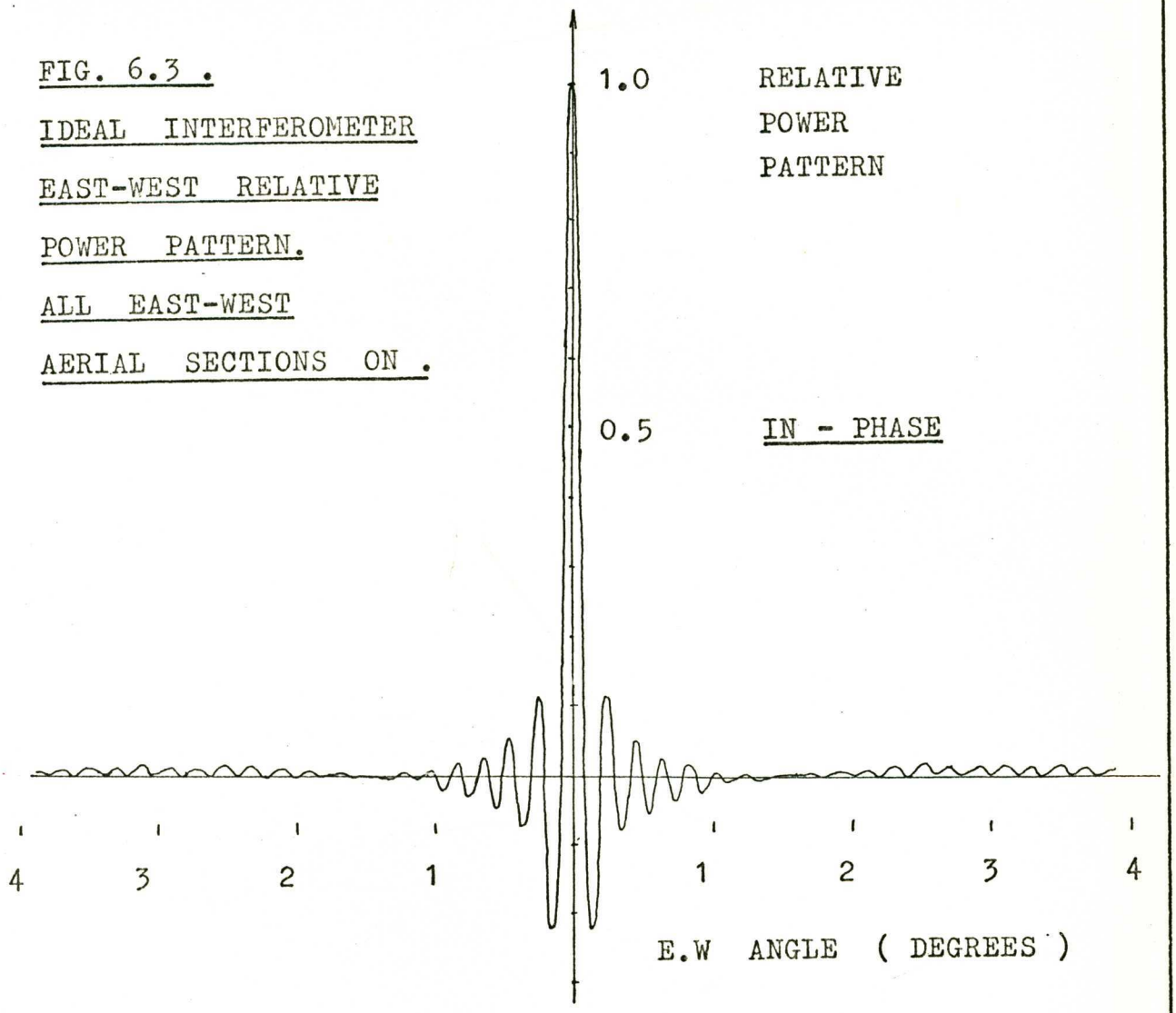

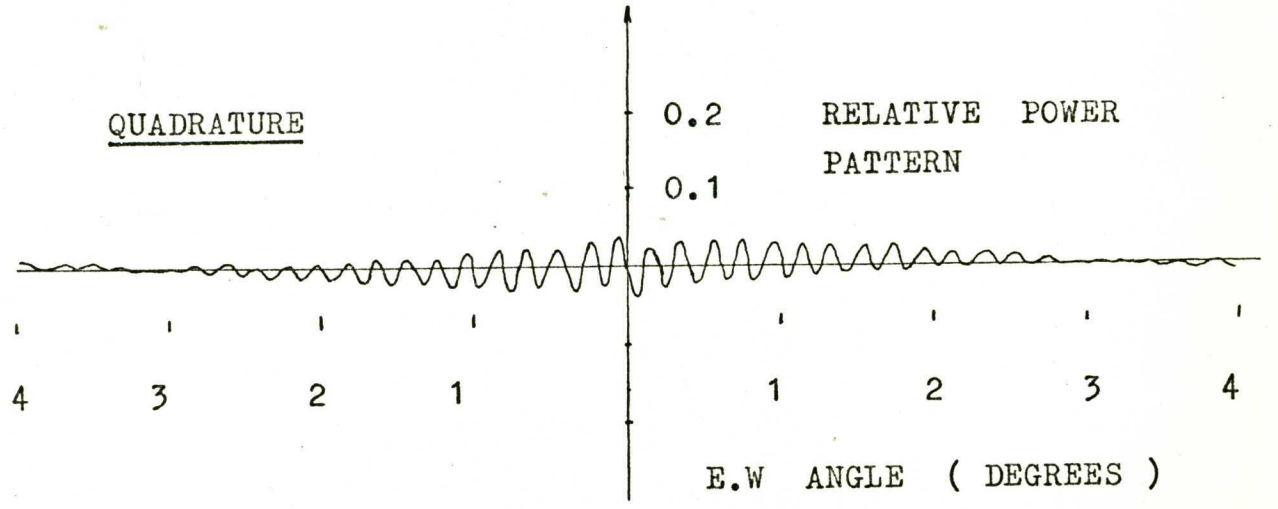

FIG. 6.4 .

INTERFEROMETER

EAST-WEST RELATIVE

POWER PATTERN.

17 E,W , 49 E,W ON .

81 E,W OFF .

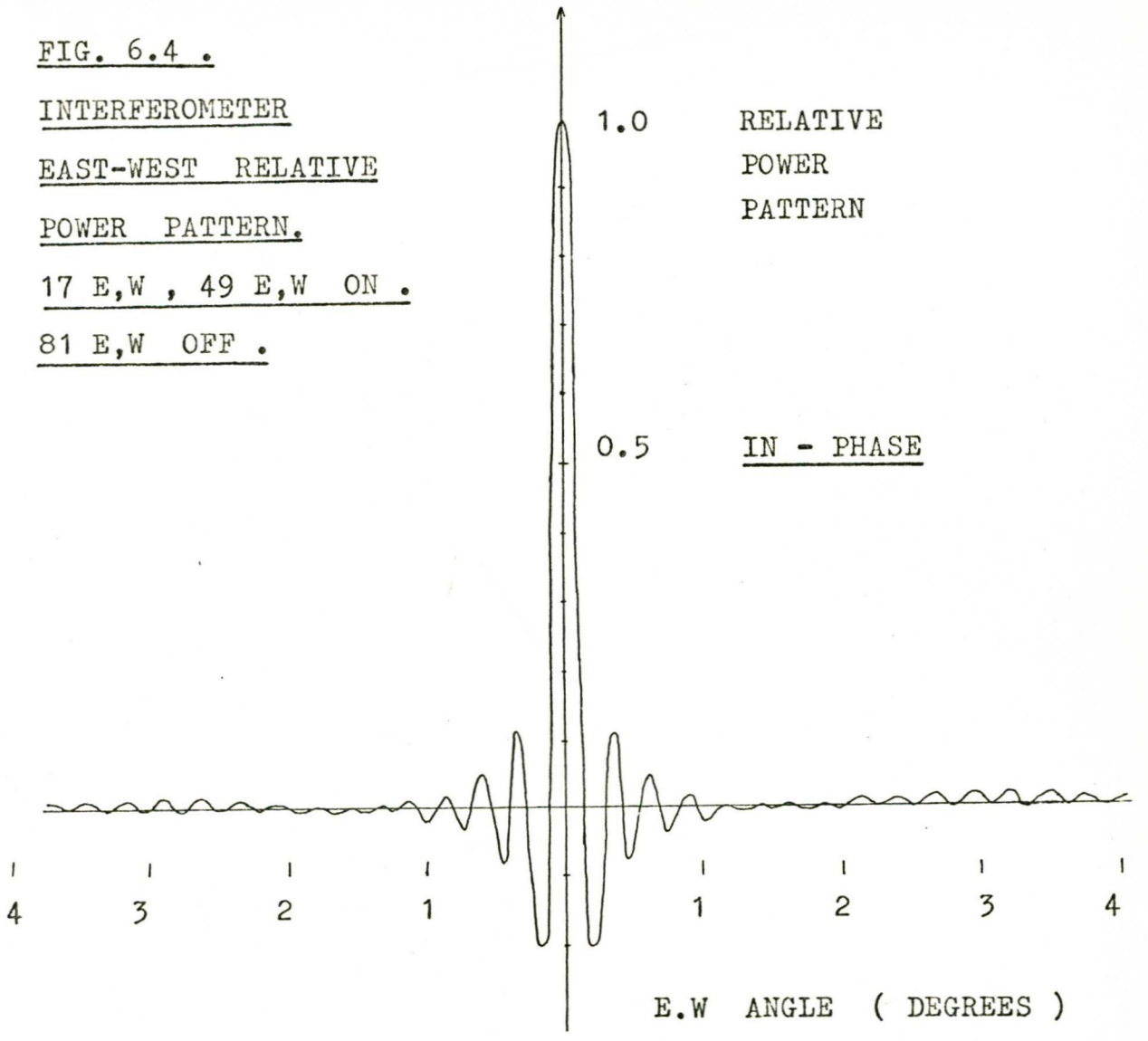

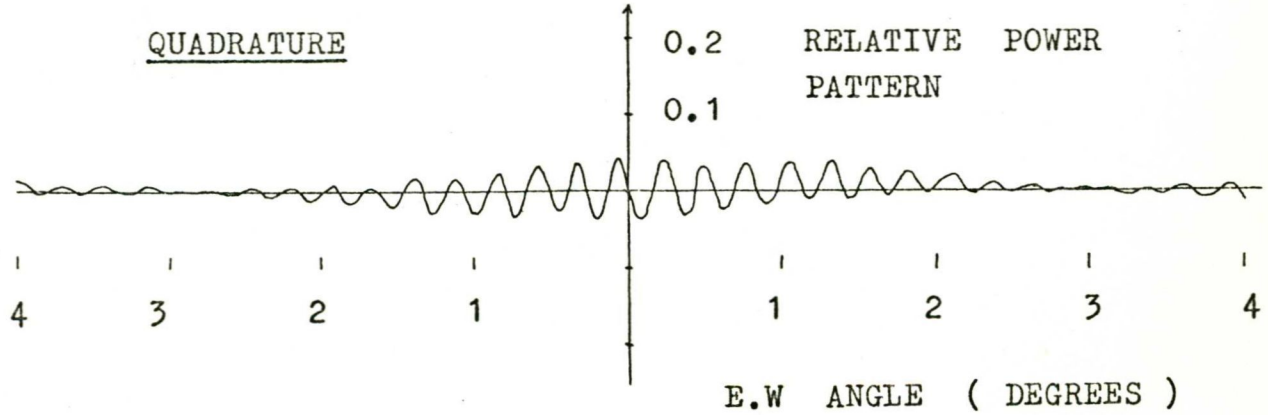

FIG. 6.5 .

IDEAL INTERFEROMETER

EAST-WEST RELATIVE

POWER PATTERN.

17 E,W ON .

49 E,W , 81 E,W OFF .

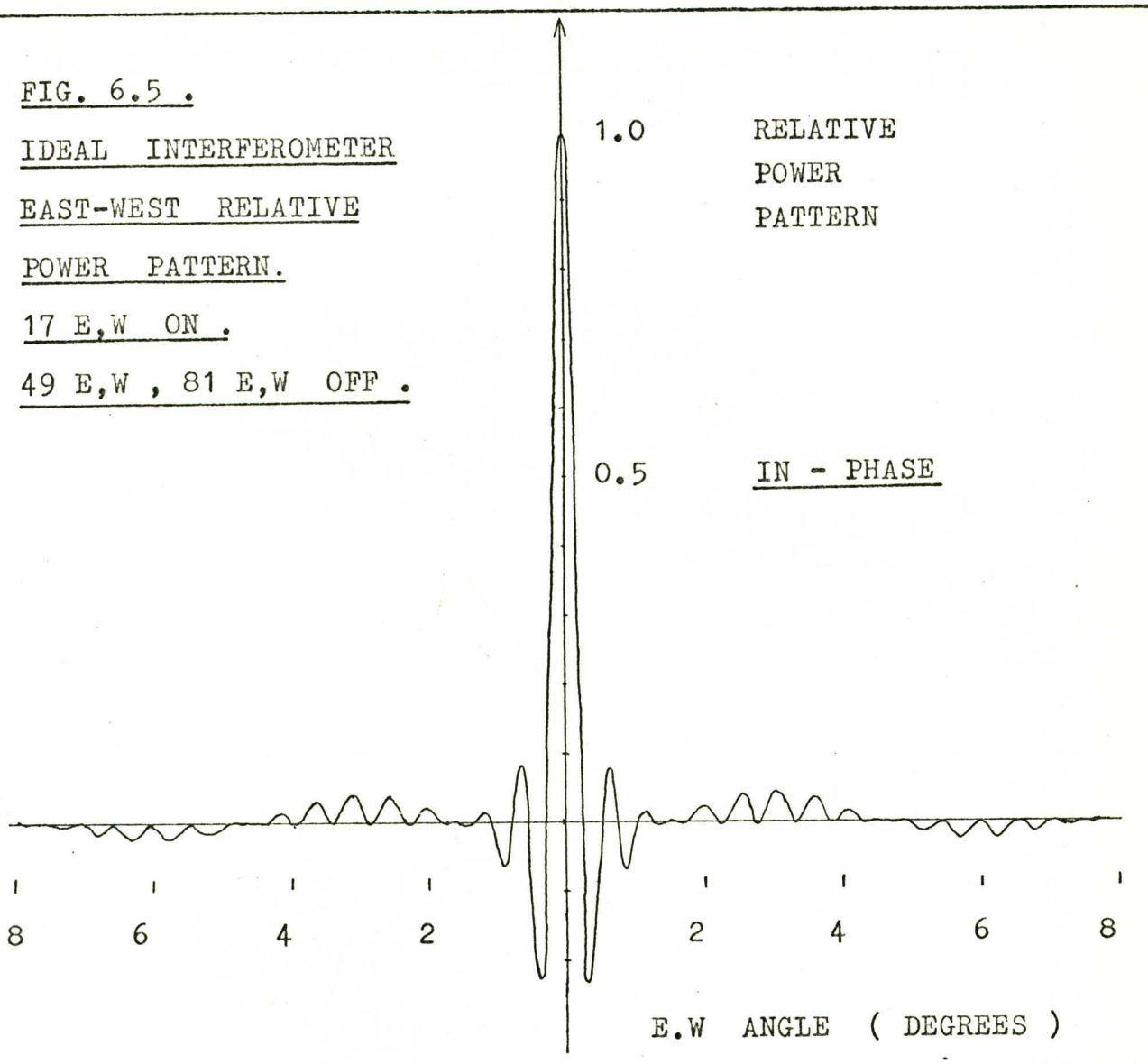

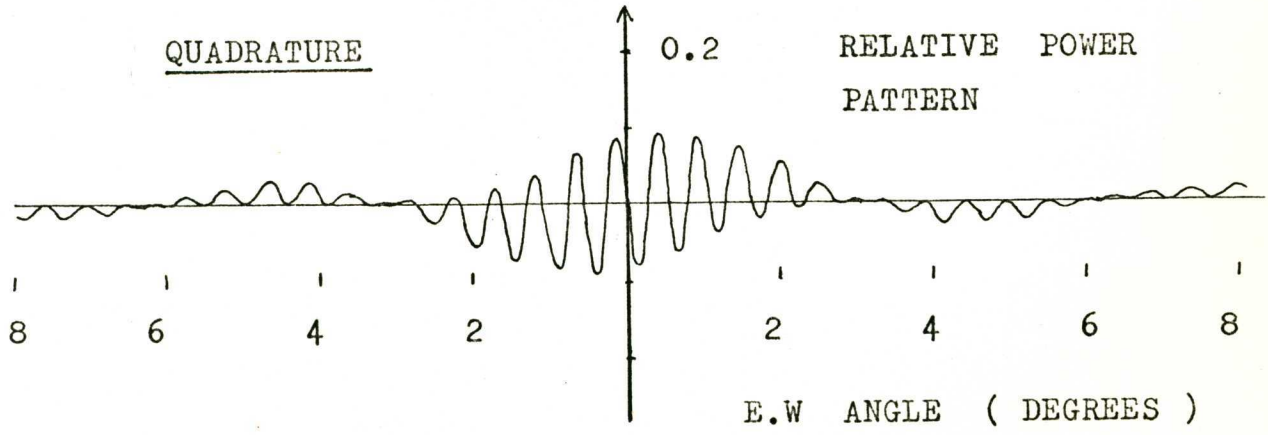

FIG. 6.6 . THE MEASURED NORTH-SOUTH POWER PATTERN OF THE EAST-WEST ARM OF THE MOLONGLO RADIOTELESCOPE AT 111.2 MHZ.

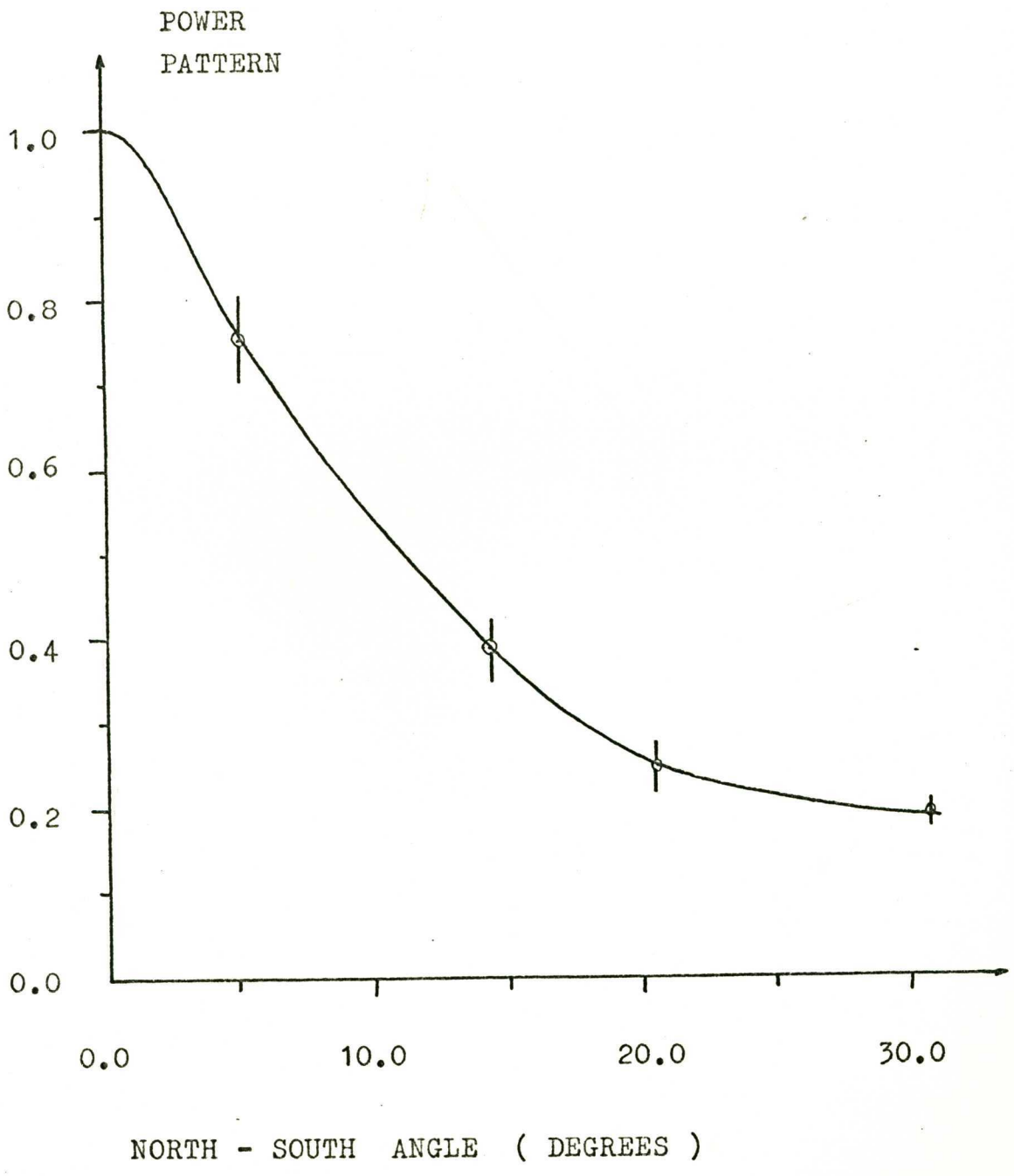

FIG. 6.7 .

0531+21

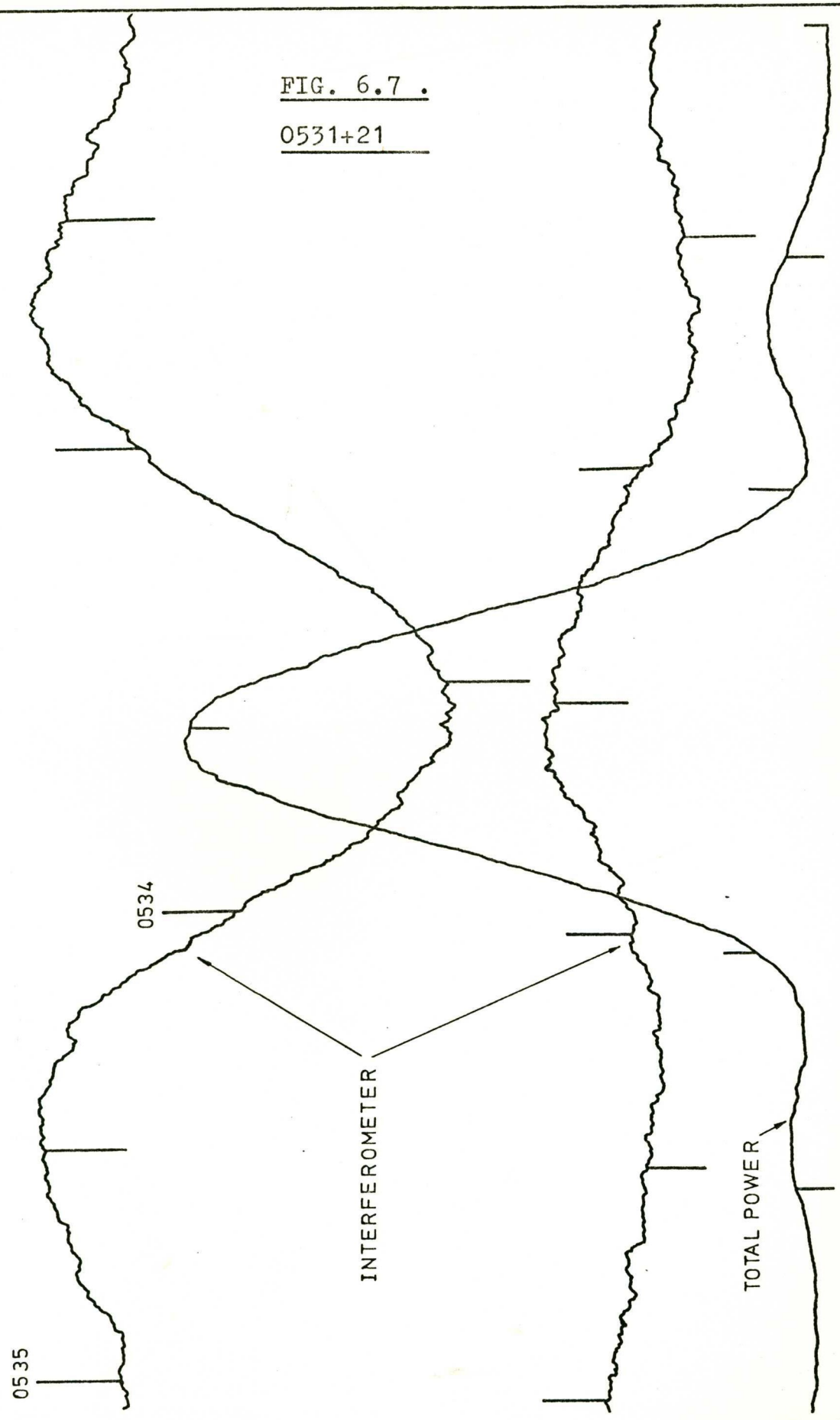

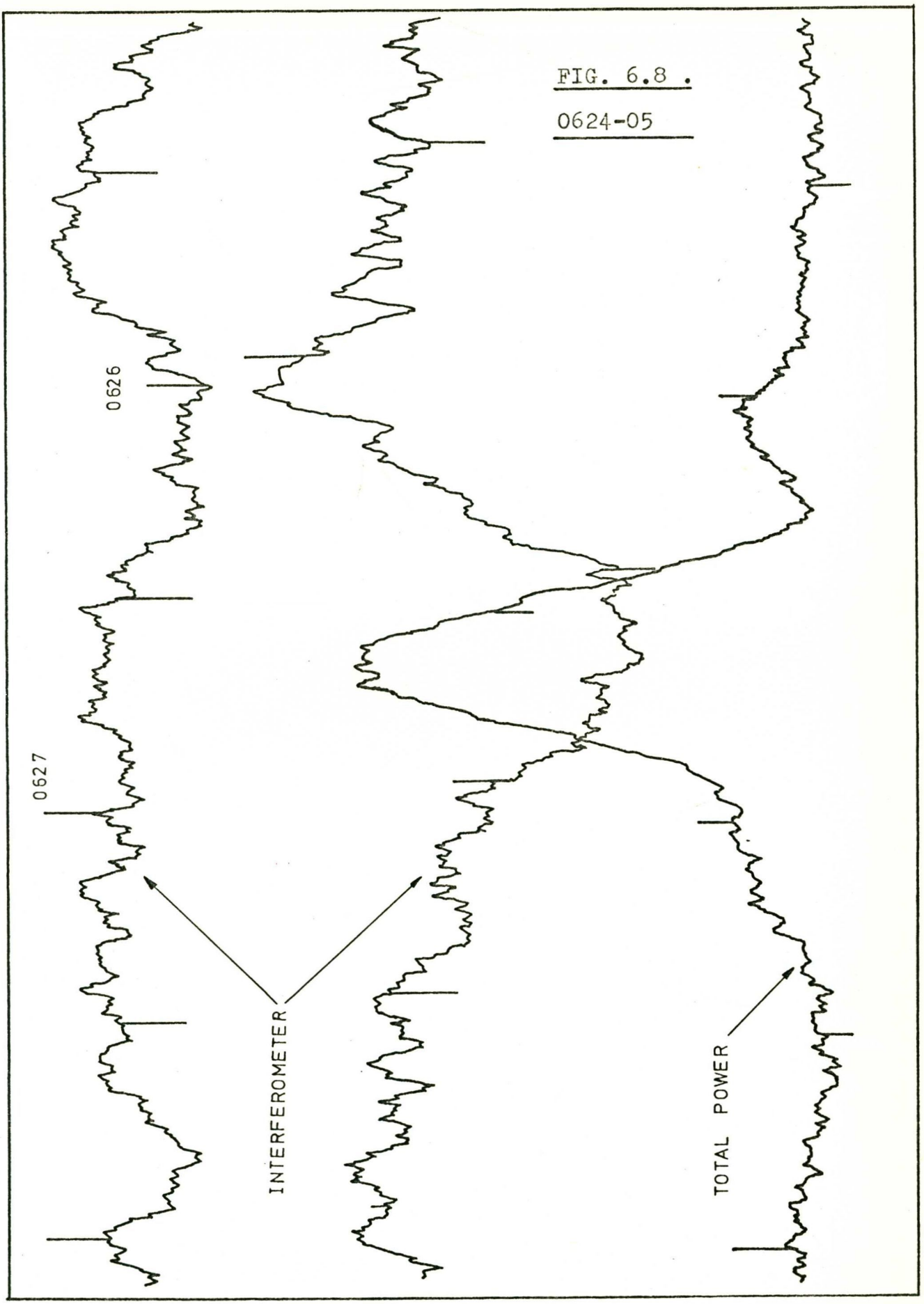

FIG. 6.8 .

0624-05

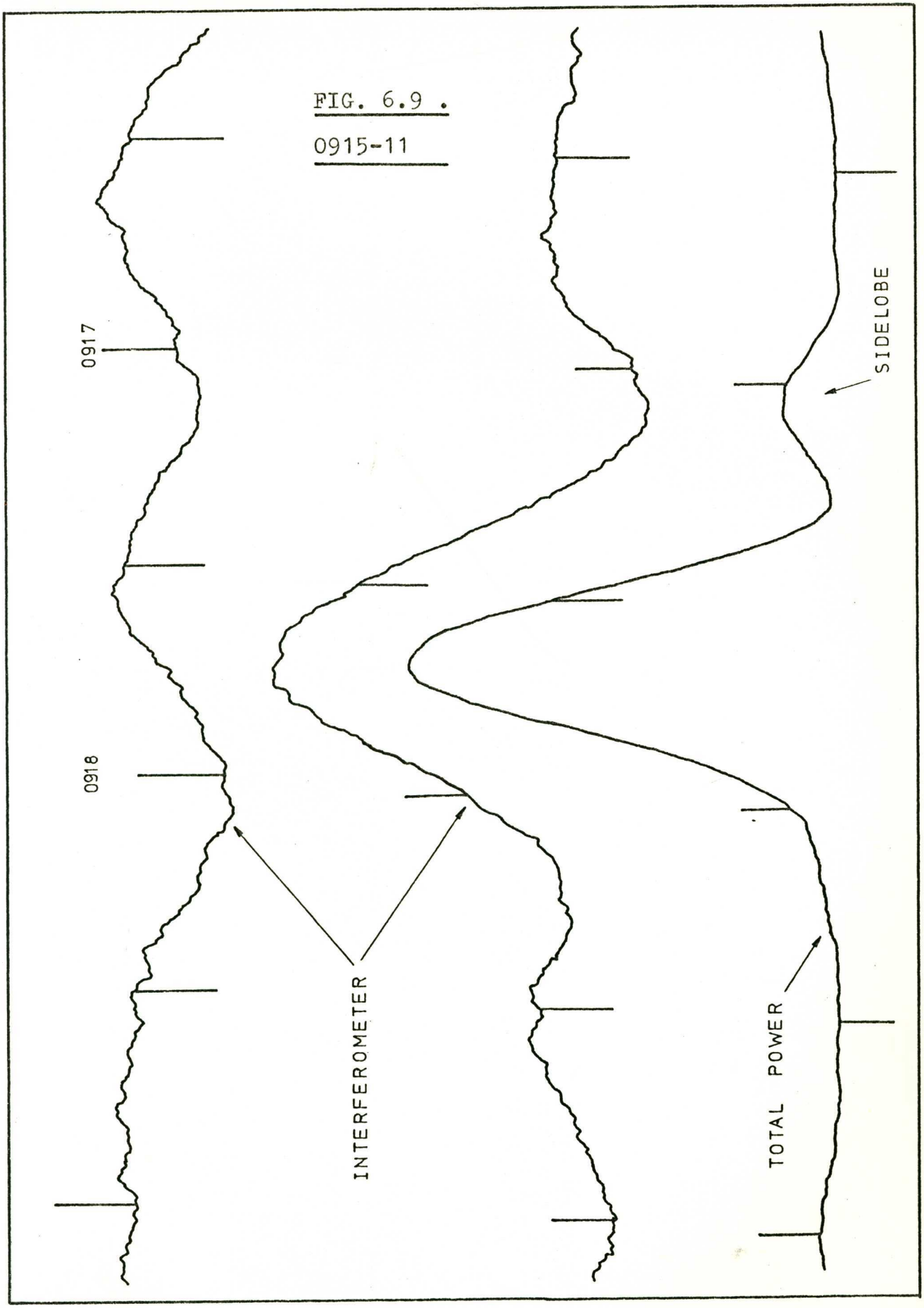

FIG. 6.9 .

0915-11

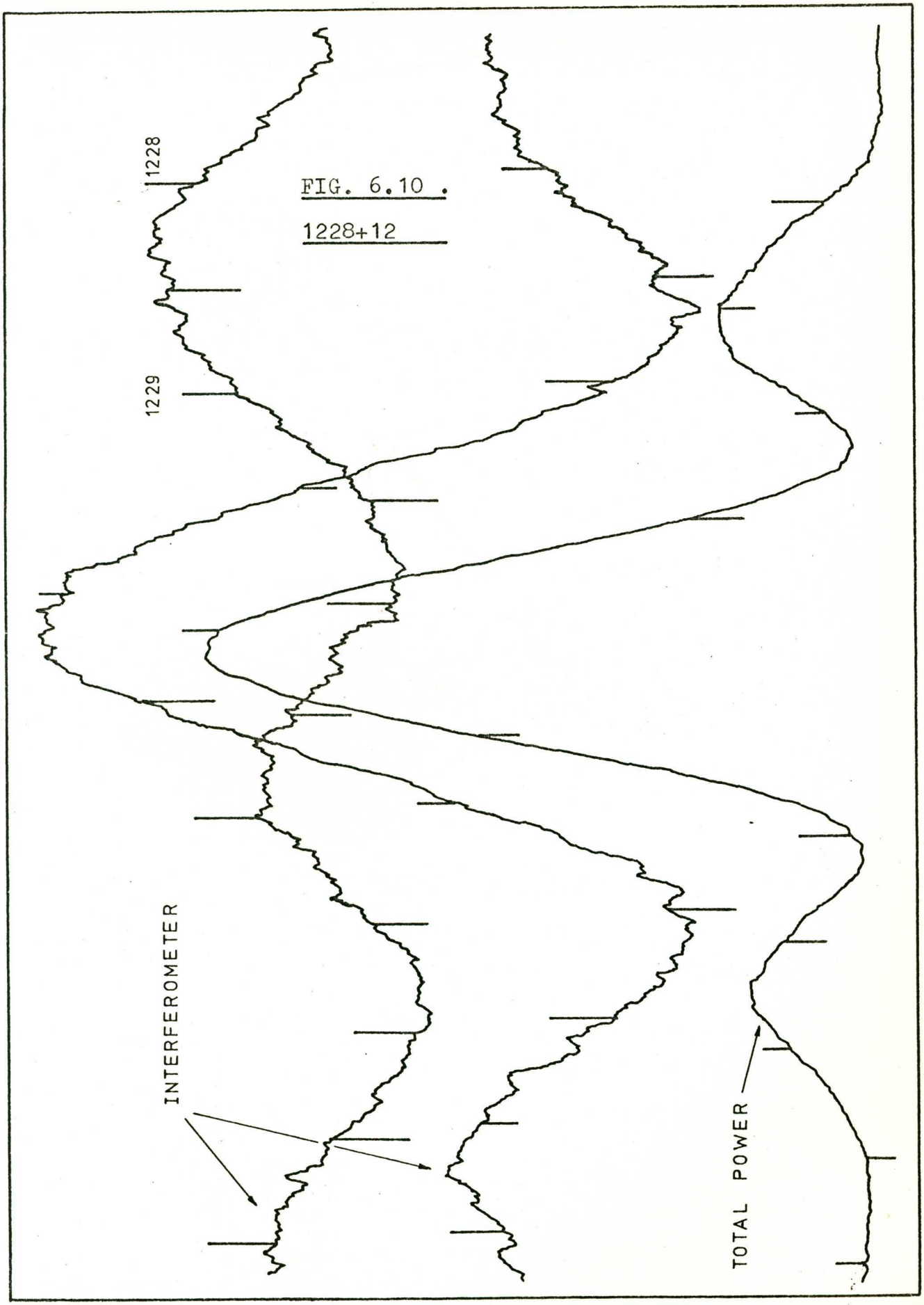

FIG. 6.10 .

1228+12

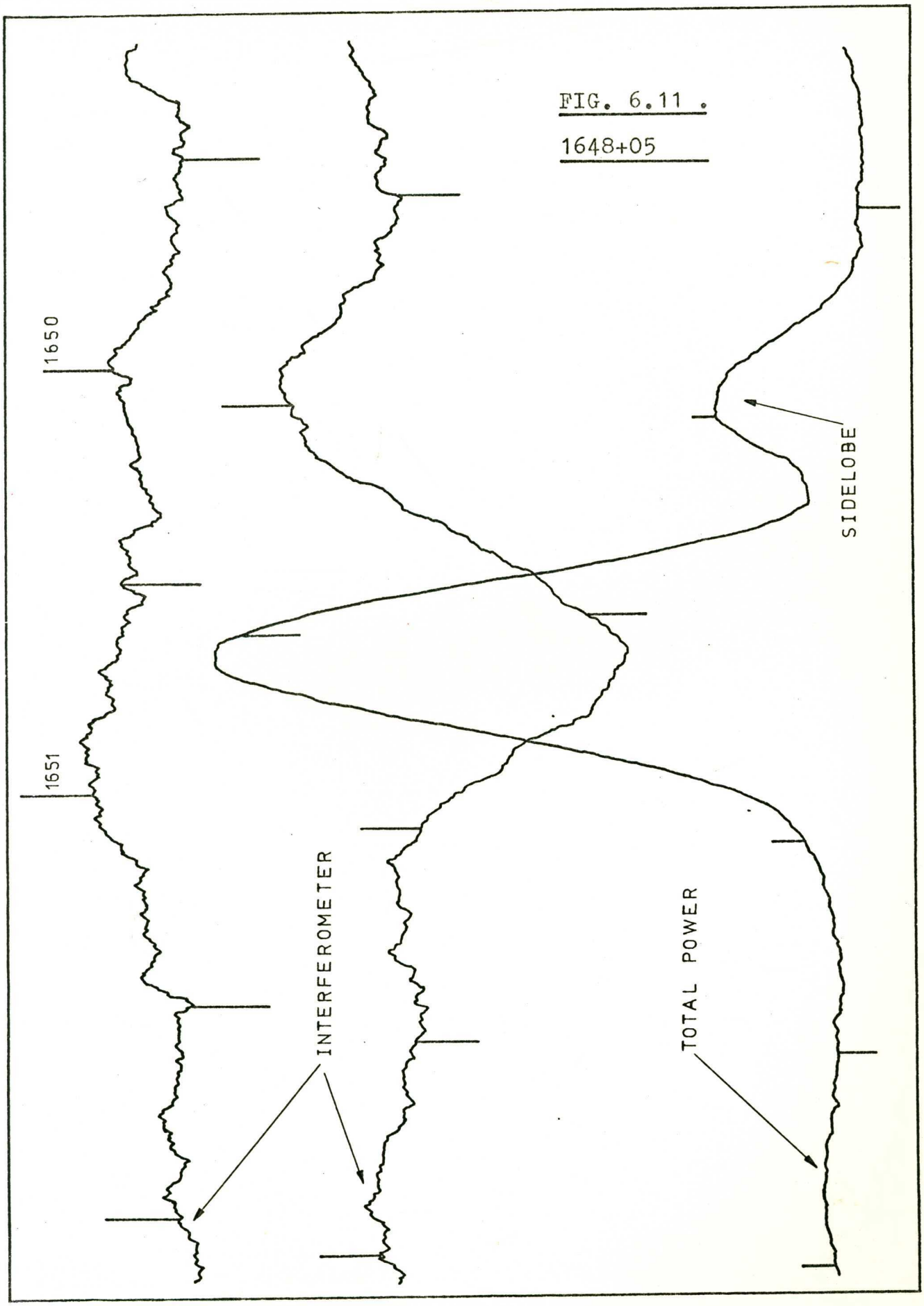

FIG. 6.11 .

1648+05

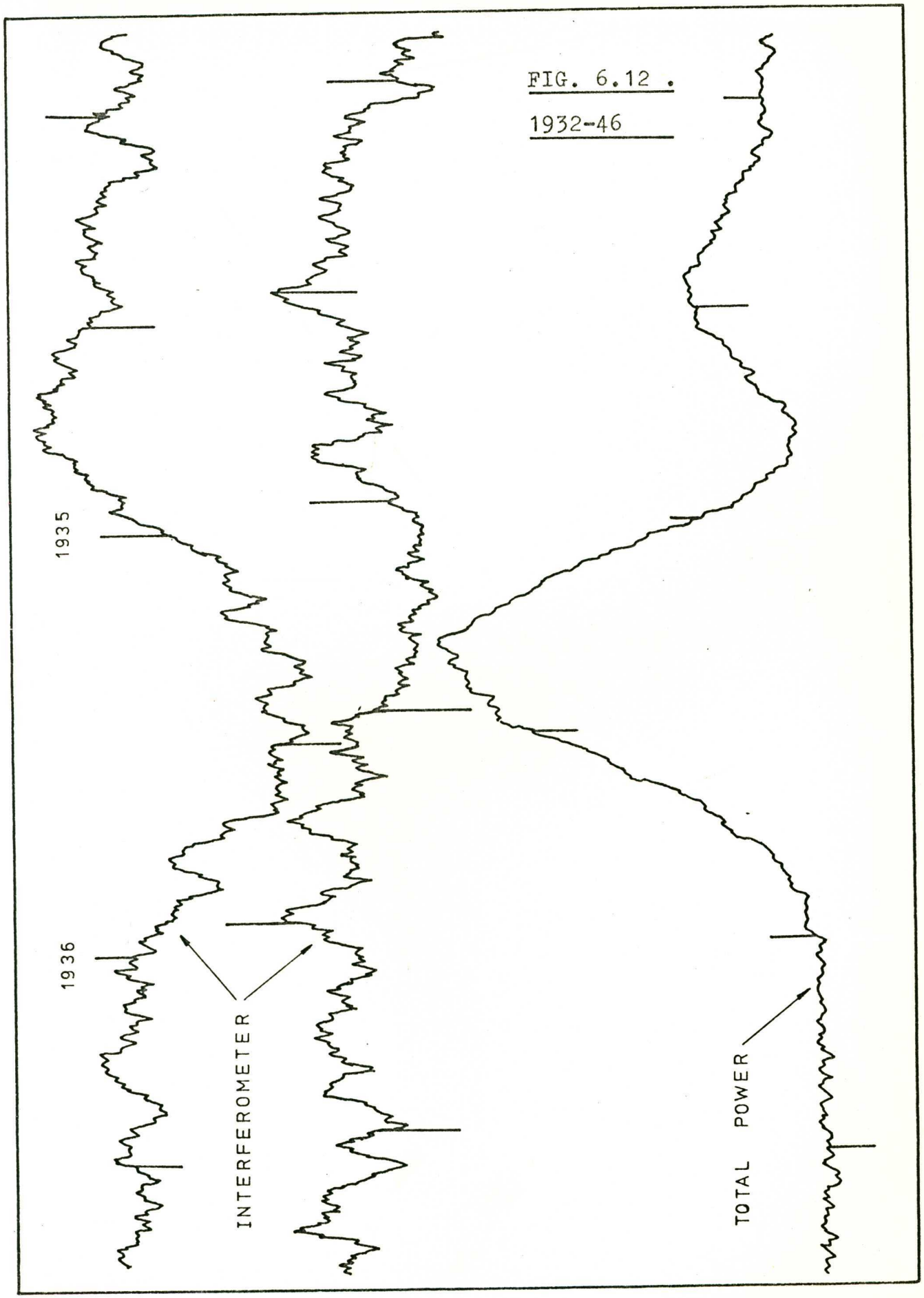

FIG. 6.12 .

1932-46

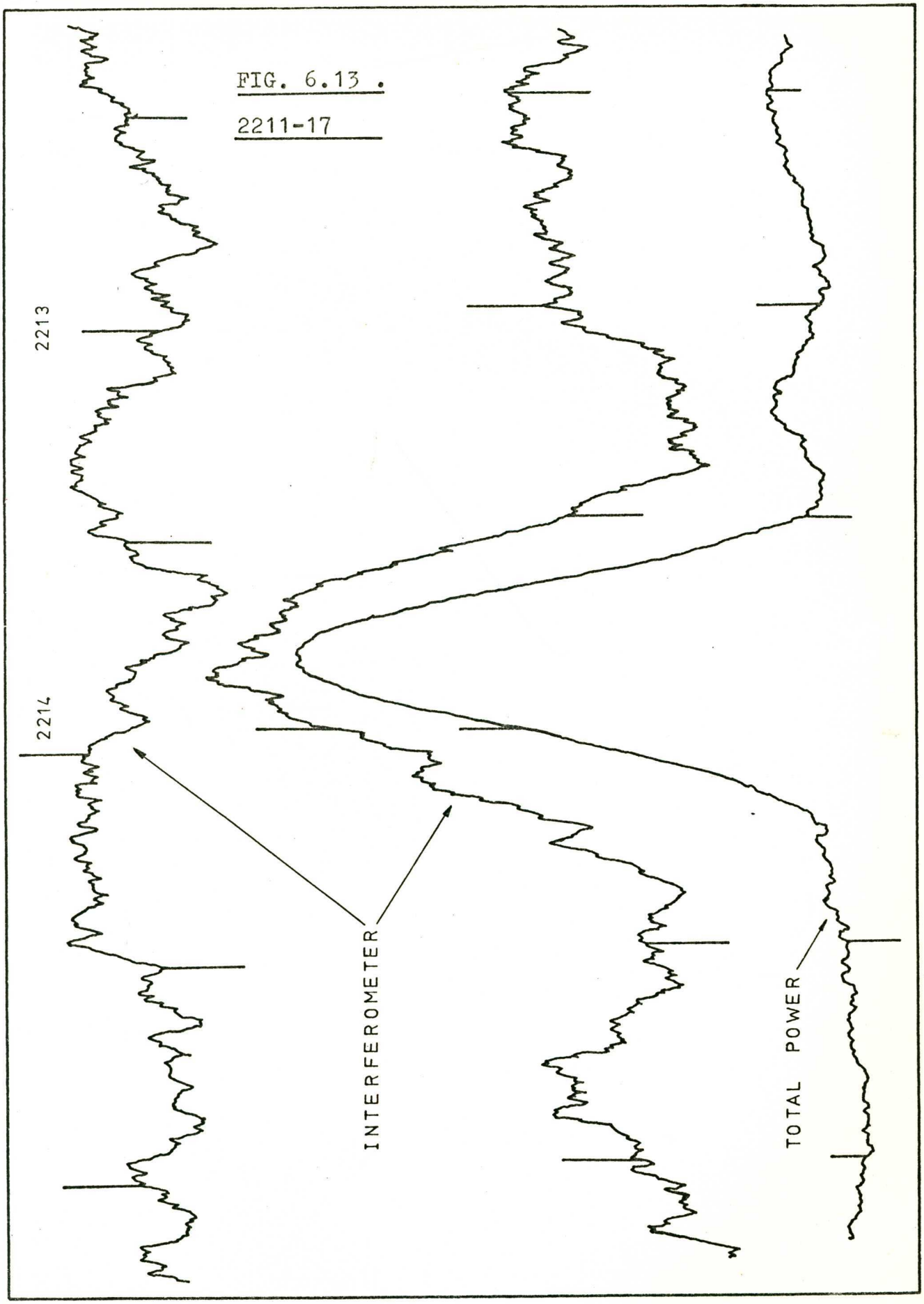

FIG. 6.13 .

2211-17

FIG. 6.14 .

(x,y) INTERFEROMETER RECORD DEFLECTION PLOT .

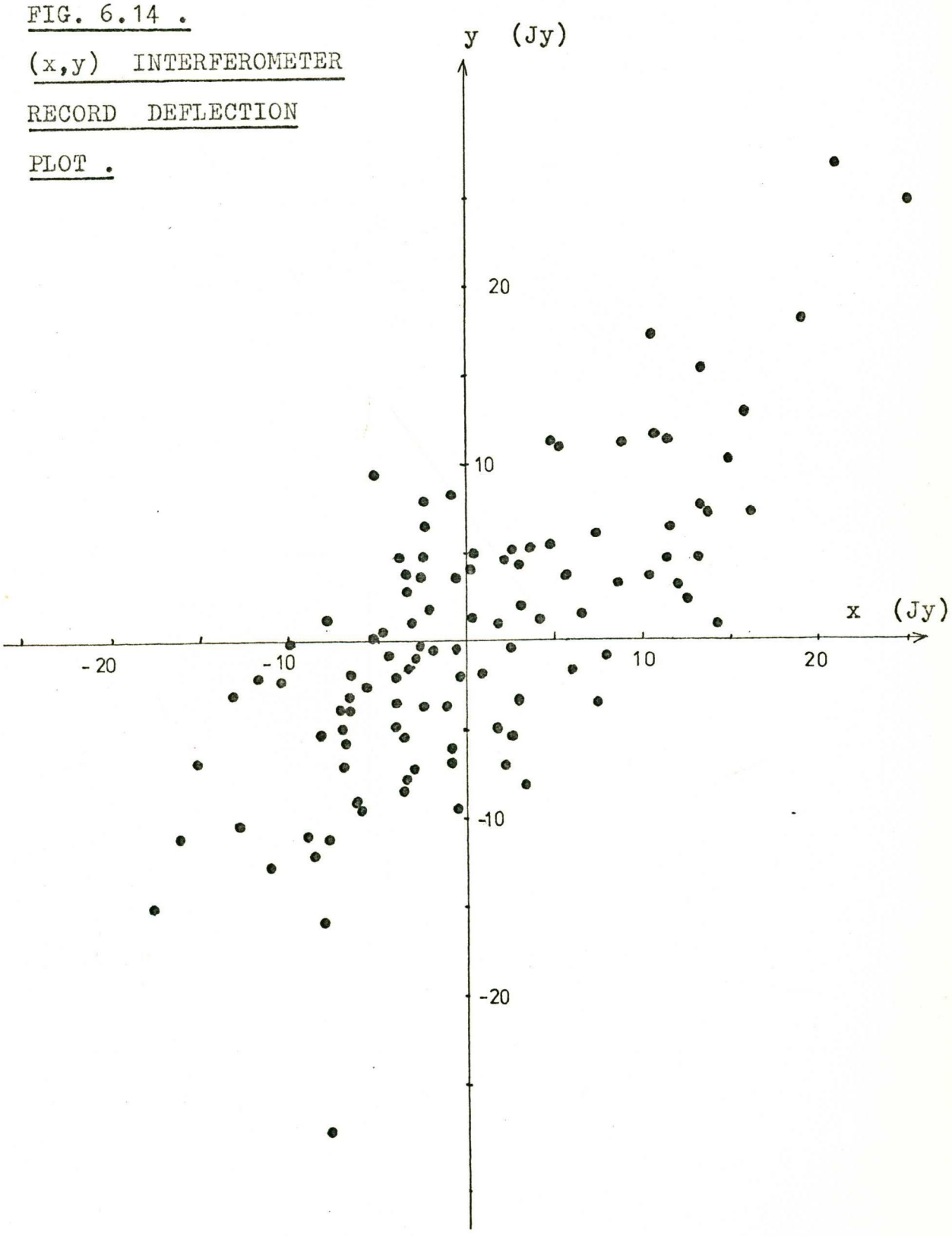

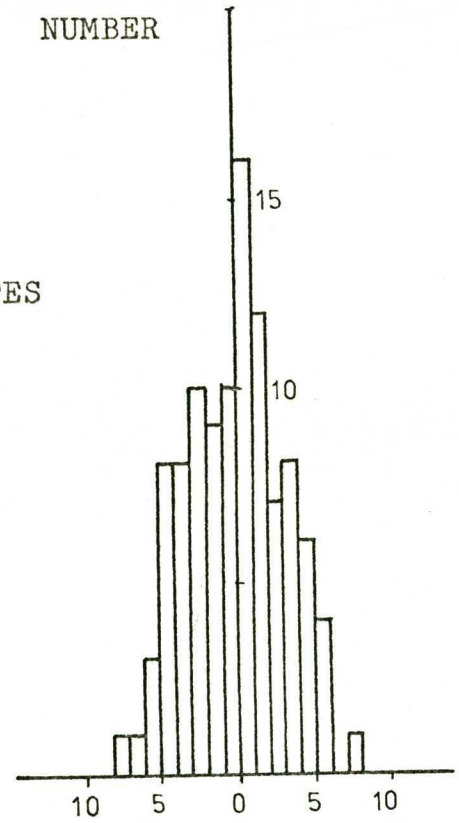

DATA POINT
Y CO-ORDINATES

FIG. 6.15 .
HISTOGRAMS OF THE DATA POINT X AND Y CO-ORDINATES OBTAINED FROM FIG. 14.

1 UNIT = 1.3 Jy

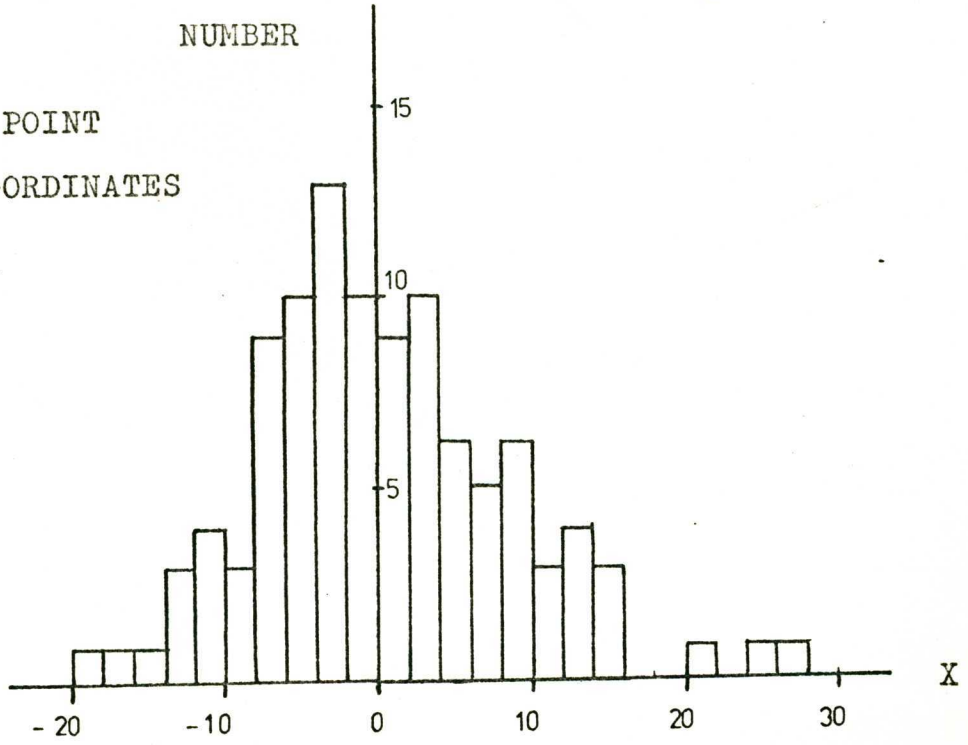

DATA POINT
X CO-ORDINATES

FIG. 6.16 .

HISTOGRAM OF THE TOTAL POWER RECORD DEFLECTIONS FOR THE FULL APERTURE EAST-WEST ARM OF THE MOLONGLO RADIOTELESCOPE AT 111.2 MHZ.

R.A. 0953.0 to 1121.0

DEC. - 11 DEGREES.

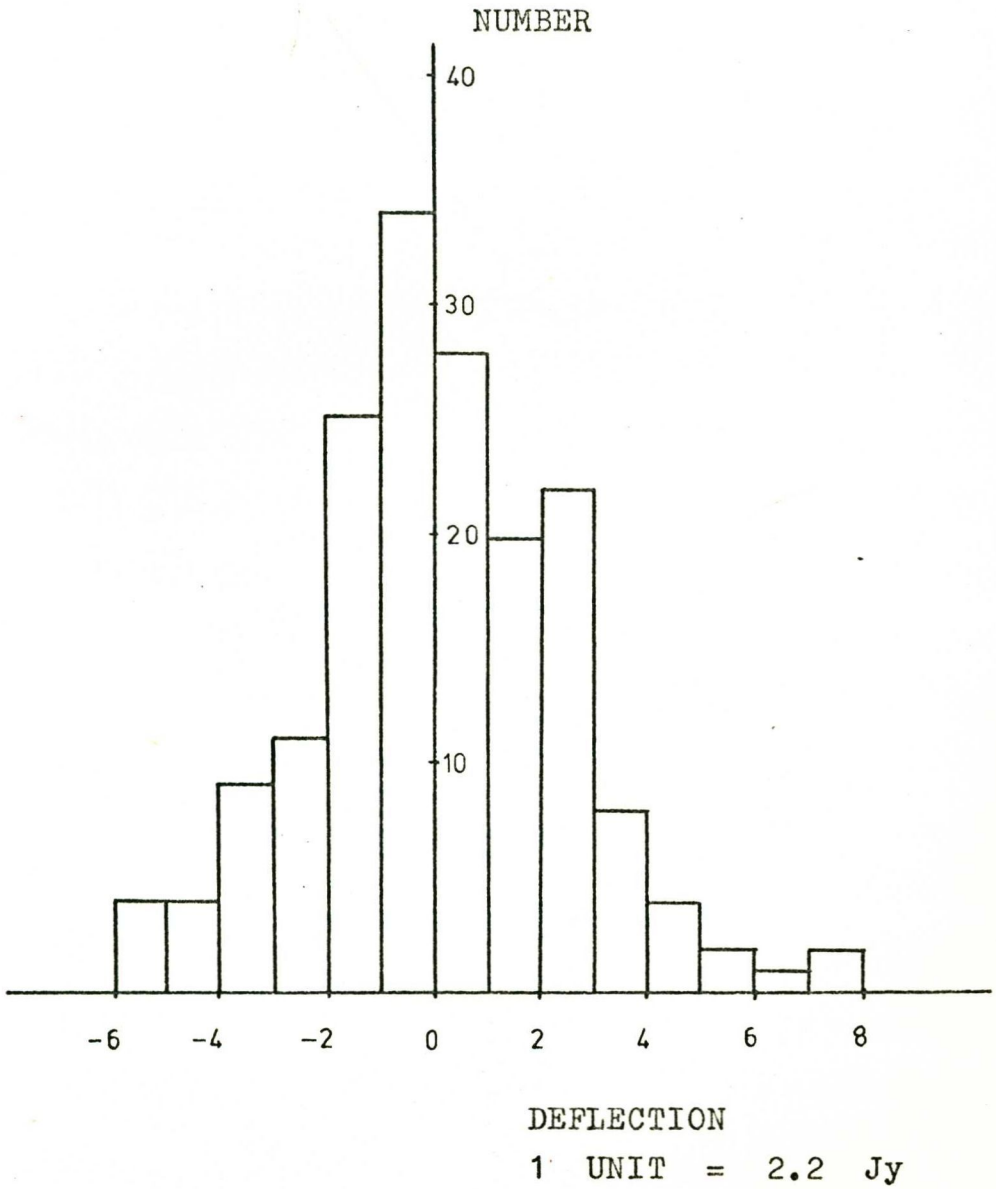

CHAPTER 7.

RELATIVE FLUX DENSITY MEASUREMENTS.

7.1 Introduction.

A set of relative flux density measurements between the absolute flux density calibrators may be derived from the East-West Aerial (hereafter abbreviated as E.W.A) total power records obtained for each absolute flux density observation.

The E.W.A total power record calibration was supplied by a diode noise source output connected to one of the 17E aerial section 111 MHz pre-amplifier inputs via an addition hybrid.

The noise diode direct current ON/OFF states produced a total power record deflection of approximately 100 Jy for a full aperture E.W.A observation.

E.W.A total power source observation uncertainties may arise from the following causes.

(a) The effect of the ground plane over which the E.W.A is erected upon the relative gain zenithal angle dependence of the E.W.A.

(b) Total power receiving system non-linearity.

(c) The E.W.A total power r.m.s confusion error.

(d) Partial resolution of sources having extended structure.

(e) The random error due to system noise, gain and phase instabilities, interference and ionospheric scintillation.

(f) Diurnal changes in the E.W.A parameters.

7.2 E.W.A Zenith Angle Relative Gain Dependence.

The resultant electric field at the E.W.A feed dipoles, received from a distant radiosource, is the vector sum of the component due to diffraction by the E.W.A's cylindrical parabola mesh surface of the plane wave propagating directly from the source and a component reflected from the ground in front of the E.W.A.

In the situation of the E.W.A directed towards a radiosource on the meridian at less than 45 degrees zenith angle the E.W.A mesh surface results in the feed dipoles lying within the geometrical optics shadow of the ground reflected ray. However, a ground reflected electric vector parallel to the feed dipoles results from diffraction of the ground reflected wave by the E.W.A mesh surface. Similarly for the E.W.A directed towards a radiosource on the meridian at greater than 45 degrees zenith angle the ground reflected feed dipole electric vector component is modified by diffraction due to the E.W.A mesh surface.

The ground reflected feed dipole electric vector is also modified in amplitude by the ground losses and in phase by both the phase change upon ground reflection and the phase angle due to the difference in length of the transmission paths of the two feed dipole electric vector components.

To examine the effect of the ground reflected wave upon the E.W.A zenith angle relative gain dependence a related, but greatly simplified, diffraction problem was considered.

In the case of the E.W.A directed towards a distant radiosource at zenith angle ϕ, the E.W.A mesh reflector surface is replaced by a perfectly conducting infinitely thin semi-infinite plane sheet. The boundary of the semi-infinite plane sheet is parallel to and contacts the lower edge of the E.W.A mesh reflector surface. The plane sheet is tangential to the cylindrical parabola mesh surface at the plane sheet boundary.

Fig 7.1 shows the North-South vertical plane cross-section of the E.W.A arm. The semi-infinite plane sheet replacing the cylindrical parabola mesh surface for the ground wave diffraction problem is also shown.

Fig 7.2 shows the co-ordinate system for the semi-infinite plane sheet diffraction problem.

The E.W.A feed dipoles are treated in this approximation as ideal thin half-wave dipoles.

The diffraction problem is to determine the total electric vector in the neighbourhood of the feed dipoles. The total electric vector is the vector sum of the electric vector of the incident field and the electric vector of the scattered field which arises from the induced current distribution on the semi-infinite plane surface such that the tangential component of the scattered field on the plane surface is minus that of the incident field.

In this problem only consider the electric vector component at the feed dipole due to the ground reflected plane wave.

In the co-ordinate system defined in Fig 7.2 the perfectly conducting half-plane is specified by

$$y = 0 , \quad x > 0$$

The polar co-ordinates r, θ ($0 \leq \theta \leq 2\pi$) of a field point P are related to x,y by the equations $x = r.\cos\theta$, $y = r.\sin\theta$.

The E.W.A feed dipoles are aligned in the vertical polarization plane. The incident plane wave propagation directions are restricted to the x,y plane. It is necessary only to consider the case of the incident plane wave magnetic field vector, denoted by H, polarized parallel to the semi-infinite sheet boundary direction (i.e H parallel to the z direction).

Specify the incident field for H-polarization by

$$H_z^{(i)} = e^{-jkr\cos(\theta - \alpha_o)} \tag{1}$$

where α_o is the angle between the propagation direction and the x-axis as shown in Fig 7.2 and k equals $2\pi/\lambda$.

Born and Wolf (1964) present the rigorous solution for the two dimensional diffraction of a H-polarized plane wave, as specified by equation (1), by a semi-infinite half-plane.

The E_x and E_y components of the total field at point P are specified by.

$$E_x = \frac{e^{-j\pi/4} \cdot e^{jkr}}{\sqrt{\pi}} \cdot \left\{ \sin\alpha_o \cdot (G(u) - G(v)) - j \cdot \left(\frac{2}{kr}\right)^{1/2} \cdot \cos\left(\frac{\alpha_o}{2}\right) \cdot \sin\left(\frac{\theta}{2}\right) \right\} \quad (2)$$

$$E_y = -\frac{e^{-j\pi/4} \cdot e^{jkr}}{\sqrt{\pi}} \cdot \left\{ \cos\alpha_o \cdot (G(u) + G(v)) - j \cdot \left(\frac{2}{kr}\right)^{1/2} \cdot \cos\left(\frac{\alpha_o}{2}\right) \cdot \cos\left(\frac{\theta}{2}\right) \right\}$$

where $u = -(2kr)^{1/2} \cdot \cos\left(\frac{\theta - \alpha_o}{2}\right)$

$$v = -(2kr)^{1/2} \cdot \cos\left(\frac{\theta + \alpha_o}{2}\right)$$

$$G(a) = e^{-ja^2} \cdot F(a)$$

$$F(a) = \int_a^{\infty} e^{j\mu^2} \, d\mu$$

In the feed dipole neighbourhood the amplitudes and phase angles of the E_x and E_y components were evaluated for values of α_o in the range $43.5^o \leq \alpha_o \leq 163.5^o$ which corresponds to the α_o range of the ground reflected plane wave for the E.W.A directed to radiosources in the zenith angle range $0^o \leq \phi \leq 60^o$.

The values of the integral F(a) were derived from tables of closely related integrals given by Rankin (1949).

The co-ordinate axis s has its origin at the centre of the half-wave feed dipole and is directed along the dipole arm as shown in Fig 7.2.

The electric vector defined as $E_s(s)$ is the vector sum of the components of the electric vectors E_x and E_y parallel to the dipole arms at the point s on the dipole arms. For a receiving dipole consider the case of a purely resistive impedance, denoted by Z, inserted at the s = 0 terminals.

The current in the load Z for an electric vector $E_s(s)$ parallel to the dipole arms is given by (Schelkunoff and Friis 1952),

$$(3) \qquad I = \frac{Z_A}{Z + Z_A} \int_{-\lambda/4}^{\lambda/4} E_s(s).Y(s;0)\, ds$$

where Z_A is the impedance of a transmitting half-wave dipole as seen from the terminals of the load and Y(s;0), termed the transfer admittance, is the current at $s = 0$ due to a unit impressed voltage at $s = s$. The reciprocity theorem provides that the transfer admittance is a symmetric function i.e

$$Y(s;0) = Y(0;s) \tag{4}$$

where $Y(0;s)$ is the current at $s = s$ per unit voltage at $s = 0$.

The transfer admittance for an ideal half-wave dipole is given by,

$$Y(0;s) = \frac{1}{73}. \cos(ks) \tag{5}$$

Hence the receiving dipole load current is given by,

$$I = \frac{1}{Z + 73}. \int_{-\lambda/4}^{\lambda/4} E_s(s) \cos(ks)\, ds \tag{6}$$

For α_o in the range $43.5^\circ \leq \alpha_o \leq 163.5^\circ$ the amplitudes and phase angles of the half-wave feed dipole load voltages

due to $E_s(s)$ may be determined.

So far, the voltage produced across a feed dipole load by a unit amplitude H-polarized plane wave incident upon a semi-infinite perfectly conducting plane sheet from a direction corresponding to the ground reflected wave has been determined.

It now remains to compare the feed dipole load voltage, denoted by $V_g(\phi)$, produced by the ground reflected wave from a distant radiosource (with the E.W.A cylindrical parabola wire mesh surface approximated by a perfectly conducting semi-infinite plane sheet) with the feed dipole load voltage, denoted by V_d, resulting from the electric vector due to the diffraction by the cylindrical parabola mesh surface (no longer approximated by a semi-infinite sheet) of the plane wave propagating directly from the radiosource.

In the present discussion the E.W.A is understood to be pointed directly at a distant radiosource situated on the meridian at zenith angle ϕ. A unit amplitude H-polarized plane wave transmitted from the source is assumed to be incident upon the E.W.A and the E.W.A's ground plane. Denote the resulting ground reflected electric vector component parallel to an E.W.A feed dipole at point s on the feed dipole arms under the semi-infinite plane sheet E.W.A cylindrical parabola mesh replacement approximation by $E_s^g(s,\phi)$.

Examine the following physical situations.

Case (a) Let the E.W.A be located in free space. A unit amplitude plane wave having the electric vector polarized parallel to the feed dipoles propagates at normal incidence upon the E.W.A aperture plane.

Case (b) The same situation as for case (a), with the difference that the cylindrical parabola mesh surface is removed i.e only the linear array of half-wave feed dipoles remains.

Case (c) The feed dipole array in free space, without the E.W.A reflecting mesh surface, in the presence of the electric vector field $E_s^g(s,\phi)$.

The ratio, denoted by R_1, of the power delivered to the load impedance across each feed dipole's terminals for case (a) divided by case (b) is given by,

$$R_1 = A_{EW}/A_F \tag{7}$$

where A_{EW} is the E.W.A maximun effective area and A_F is the maximun effective area of the feed dipole array in the absence of the E.W.A's reflecting mesh surface.

The ratio, denoted by $R_2(\phi)$, of the power delivered to the load impedance across each feed dipole's terminals for case (b) divided by case (c) is given by,

$$(8) \qquad R_2(\phi) = \frac{\left[\int_{-\lambda/4}^{\lambda/4} \cos(ks)\, ds \right]^2}{\left| \int_{-\lambda/4}^{\lambda/4} E_s^g(s,\phi)\cos(ks)\, ds \right|^2}$$

where equation (6) was used to calculate the load impedance currents.

The ratio of $|V_g(\phi)|$ to $|V_d|$, denoted by $R(\phi)$, is given by,

$$(9) \qquad R(\phi) = \frac{|V_g(\phi)|}{|V_d|}$$

$$= (R_1 R_2(\phi))^{-1/2}$$

The following expression for $R(\phi)$ results from the combination of equations (7), (8) and (9).

$$(10) \qquad R(\phi) = (A_F/A_{EW})^{1/2} \cdot \frac{\pi}{\lambda} \cdot \left| \int_{-\lambda/4}^{\lambda/4} E_s^g(s,\phi)\cos(ks)ds \right|$$

The equation (10) numerator integral is readily evaluated from the previously calculated integrals for the case of the unit amplitude H-polarized plane wave incident upon the semi-infinite plane. The amplitude of the incident ground reflected plane wave is reduced by the H-polarization ground reflection amplitude coefficient.

A_{EW} was determined from the relationship,

$$(11) \qquad A_{EW} = \frac{\lambda^2}{\iint_{4\pi} P_n \, d\Omega}$$

where P_n is the E.W.A normalized power pattern. The beam solid angle integral was evaluated by the solid angle integration of the observed E.W.A normalized power pattern.

A_F was evaluated theoretically for an array of ideal half-wave dipoles.

For the E.W.A at 111 MHz

$$\frac{\pi}{\lambda} \cdot \left(A_F / A_{EW} \right)^{1/2} \simeq 0.53$$

The phase difference between $V_g(\phi)$ and V_d is comprised of the following.

(a) The transmission path length difference between the plane wave directly incident upon the E.W.A feed dipoles from a distant radiosource on the meridian at zenith angle ϕ and the ground reflected wave incident upon the lower edge of the E.W.A mesh reflector surface.

(b) The phase delay of $V_g(\phi)$ relative to the phase angle of the ground reflected wave incident upon the lower edge of the E.W.A mesh reflector surface.

(c) The phase angle of the H-polarized ground plane reflection coefficient for zenith angle ϕ .

(d) The twice the E.W.A focal length phase delay and the 180 degree phase change upon reflection by the E.W.A mesh reflector surface of the directly received wave. The phase angle of the feed dipole electric vector component due to the diffraction by the E.W.A mesh reflector surface of the plane wave received directly from the source was assumed to remain constant along each feed dipole's arms.

The phase angle difference between $V_g(\phi)$ and V_d , denoted by δ degrees, is given by subtracting phase angle contribution (d) from the sum of phase angle contributions (a), (b) and (c).

The ground surface below the E.W.A may be treated as horizontal in the North-South direction. Along the East-West direction the ground below the E.W.A is at its lowest point at the central E.W.A gap. The ground slopes upwards

in both East and West directions with a gradient of approximately 33cm per kilometre. Approximating the ground surface by linear East and West slopes, the effect of the ground slope is to reduce $R(\phi)$ by a factor of not more than six percent, depending upon the zenith angle.

Define G as the E.W.A's zenith angle gain along the meridian in the presence of ground reflection effects.

Define G_o as the E.W.A's zenith angle gain along the meridian in the absence of ground reflection effects.

The ratio G/G_o is given by,

$$(12) \qquad G/G_o = 1 + R^2(\phi) + 2R(\phi)\cos\delta$$

The ratio G/G_o is plotted as a function of ϕ in Fig 7.3. The G/G_o ratio values were calculated for both wet and dry soil parameters (Table 4.1). For $\phi \leq 50$ degrees the G/G_o ratio varies periodically with ϕ in the range $0.94 \leq G/G_o \leq 1.07$.

The claim is not made that Fig 7.3 represents the actual E.W.A zenithal relative gain. The differences between the real E.W.A ground reflection problem and the simplified semi-infinite sheet ground wave diffraction approximation are sufficiently evident to remove the necessity of listing

the differences. The value of Fig 7.3 is the pointing towards reasonably expected approximate sizes of zenithal angle dependant variations in the real E.W.A meridional relative gain.

7.3 The Relative Flux Density Measurements.

The total power receiving system equipment, observation procedure and output record deflection measurement procedure were described in Chapters (2), (3) and (6).

The total power relative flux density measurements were restricted to the five Category I sources. Virgo A was excluded from the relative flux density measurements for the following reasons.

(a) Extended source structure.

(b) The ratio of the E.W.A 17 E, 17 W ON only effective area to the full aperture E.W.A effective area was not known to high accuracy.

Taurus A was excluded for the following reasons.

(a) The Northern declination limit of the E.W.A arms was $+18.7^{\circ}$. Consequently Taurus A transits 3.3 degrees North of the E.W.A power pattern maximun. The relative flux density measurements for all other observed sources were made for the source transiting through the E.W.A power pattern maximun. Uncertainty would be introduced in to the Taurus A relative flux density measurement due to the accuracy to

which the power pattern in declination is known for the E.W.A set at its Northern declination limit.

(b) Uncertainty in the ratio of the E.W.A 49 E, 17 E, 17 W and 49 W ON only effective area to the full aperture E.W.A effective area.

Both Taurus A and Virgo A are very strong sources at 111 MHz which introduces the possibility of excessive receiver non-linearity.

Table 7.1 lists the E.W.A total power source deflection/ E.W.A CAL ratios obtained from the March and April 1976 observing sessions. The quoted r.m.s errors are the random components of the SOURCE/CAL r.m.s errors assessed from the scatter of the SOURCE/CAL ratios.

The relative gains and phasing of the six component E.W.A sections display significant variations over a one month interval. The E.W.A CAL calibrates only the 17 E aerial signal path, commencing from one of the 17 E pre-amplifiers, to the E.W.A combiner. A diurnal or longer period gain or phase variation of the E.W.A sections relative to the 17 E section cannot be monitored by the E.W.A CAL. The unstable behaviour of the E.W.A results in the equivalent value in Jy's of the E.W.A CAL deflection having a different value for the March and April 1976 observing sessions.

For each source, the April SOURCE/CAL ratio was divided by the March SOURCE/CAL ratio. The weighted average of the resulting set of April/March SOURCE/CAL ratios was calculated

where each source's April/March SOURCE/CAL ratio was weighted inversely by its own variance. The resulting ratio of the equivalent flux density values of the E.W.A CAL for the March and April 1976 observing sessions was 0.756 $\pm$ 0.024 .

Table 7.2 lists the set of relative flux density measurements obtained from the combination of the March and April 1976 relative flux density measurements. The given relative flux densities are the weighted averages of the April and the corrected March SOURCE/CAL ratios for each source.

Table 7.1

Relative Flux Density Measurements.

1. March 1976.

Source	Number of Observations	SOURCE/CAL	R.M.S Error (Percent)
0624-05	7	0.837	5.6
0915-11	6	3.587	5.2
1648+05	7	5.003	4.4
1932-46	1	0.995	14.0
2211-17	2	1.134	10.0

Table 7.1 (continued)

2. April 1976.

Source	Number of Observations	SOURCE/CAL	R.M.S Error (Percent)
0624-05	8	0.709	3.7
0915-11	8	2.708	3.5
1648+05	9	3.517	4.3
1932-46	11	0.664	2.3
2211-17	11	0.908	3.5

Table 7.2

Combined March and April 1976 SOURCE/CAL Ratios (Referred to April Cal Value).

Source	SOURCE/CAL	R.M.S Error (Percent)
0624-05	0.686	3.1
0915-11	2.711	2.9
1648+05	3.648	3.1
1932-46	0.666	2.3
2211-17	0.903	3.3

7.4 E.W.A Total Power Receiving System Non-linearity.

The linearity characteristics of all the total power receiving system amplifiers located in the phasing hut were measured. The pad placement in the total power receiving system was selected to minimize the effects of non-linearity.

Non-linearity in the signal path from the hybrid 1 output to the total power recorder output was measured in the absolute flux density measurement non-linearity investigations (Chapter 6).

Fig 7.4 shows an experimental arrangement used to assist in the investigation of non-linearity in the E.W.A receiving system ahead of the E.W.A input to hybrid 1. The E.W.A CAL diode noise source was replaced by a 111 MHz hybrid which added the outputs from two diode noise sources, designated A and B. Both diode noise source output noise temperatures were remotely controllable from the control room. The outputs of both diode noise sources were unmodulated.

All of the absolute flux density calibration sources were observed over a one day session in the following manner.

a. For each source the E.W.A total power receiving system gains and pad arrangement were closely similar to the same conditions that applied for the absolute flux density observations. The E.W.A's total power output remained incorporated into the absolute flux density measurement receiving system (which was set in the observe mode).

The purpose of noise diode source A is to raise or lower the E.W.A system noise temperature as required. The diode current of diode noise source B was monitored in the control room. Turning the diode current ON/OFF for a fixed value of the diode noise source B direct current meter reading provided a repeatable calibration deflection. The source transit was recorded for the E.W.A directed at the source declination.

b. A diode noise source B calibration deflection comparable to the source deflection was recorded.

c. Noise was added from diode noise source A to create a new level on the chart recorder at approximately the same deflection relative to the source baseline as for the calibration deflection obtained in step (b).

d. A noise source B calibration deflection was placed on the newly created baseline.

Steps (b), (c) and (d) were repeated a sufficient number of times to enable the effect of random noise on the measurement of the calibration deflections to be reduced to insignificance. If ΔT is the increase in the E.W.A system noise temperature above the value applying for the source baseline then the total power record deflection measured from the source baseline due to ΔT can be approximately expressed by $D = C.(\Delta T)^{\alpha}$,where D is the deflection, C is a constant and α describes the linearity

characteristic. The measured α may be corrected for the known non-linearity present in the receiving system between the hybrid 1 and the total power chart recorder outputs.

If the hybrid 1 to the chart recorder output non-linearity fails to account entirely for the measured α then there exists three possibilities for the origin of the unaccounted non-linearity.

a. The non-linearity lies exclusively in the signal path from the 17 E pre-amplifier input to the location of combination of the E.W.A section voltages.

b. The non-linearity lies exclusively in the signal path from the location of E.W.A section voltage combination to the hybrid 1 input.

c. The non-linearity arises from both of the receiving system locations described in (a) and (b).

Assume possibility (b) is valid. For each flux density calibration source the following steps were carried out.

a. The source deflection was corrected for non-linearity using the measured value of α pertaining to that particular source. The measured value of α was left uncorrected for non-linearity between the hybrid 1 and the total power chart recorder outputs.

b. The deflection that would have been produced by the usual E.W.A CAL was calculated from the ratio of source deflection (uncorrected for non-linearity) to the E.W.A CAL deflection

(uncorrected for non-linearity) determined previously from the relative flux density measurements listed in Table 7.2. The E.W.A CAL corrected for non-linearity was determined for each source.

c. The information was now available to form the ratios of source deflection (corrected for non-linearity) to the E.W.A CAL deflection (corrected for non-linearity).

Table 7.3 lists for each Category I source the SOURCE/CAL ratio (corrected for non-linearity) divided by the SOURCE/CAL ratio (uncorrected for non-linearity).

The third column of Table 7.3 lists the above ratios (column 2 Table 7.3) after correction for the non-linearity present in the receiving system between hybrid 1 and the total power chart recorder output i.e column 3 represents the non-linearity present in the receiving system ahead of the E.W.A input to hybrid 1 under the non-linearity assumption (b).

Only 0915-11 and 1648+05 are significantly affected by non-linearity in the E.W.A receiving system ahead of the hybrid 1 input. If assumption (b) is valid then the column 2 Table 7.3 SOURCE/CAL non-linearity correction factors should be applied to the Table 7.2 SOURCE/CAL ratios. In practice the column 2 Table 7.3 SOURCE/CAL non-linearity correction factors were applied to the Table 7.2 SOURCE/CAL ratios. In the case of 0915-11 and 1648+05 the uncertainty in applying the column 3 Table 7.3 component of the column 2 SOURCE/CAL non-linearity correction factor is small in

comparison to other error sources affecting the relative flux density measurements.

In retrospect, an experiment involving the switching OFF of individual E.W.A section I.F noise contributions at the E.W.A combiner would have supplied the additional information necessary to distinguish between the non-linearity possibilities (a), (b) and (c).

Table 7.3

SOURCE/CAL Non-linearity Corrections.

(1) SOURCE	(2) SOURCE/CAL Ratio (Non-linearity corrected divided by non-linearity uncorrected)	(3) SOURCE/CAL Ratio (Column 2 ratio corrected for non-linearity between hybrid 1 and the chart recorder)
0624-05	0.997	----
0915-11	1.013	1.006
1648+05	1.025	1.016
1932-46	0.997	-----
2211-17	0.996	-----

7.5 E.W.A Confusion Error.

The total power r.m.s confusion error was measured for the full aperture E.W.A as 5.4 Jy (Chapter 6). The peak SOURCE/CAL ratio for 0624-05 was reduced by 1 percent due to confusion by 0625-35 (the correction was also applied to the absolute flux density measurement).

7.6 Uncertainty in the E.W.A Zenithal Relative Gain.

An r.m.s error of 4 percent was allowed for in the relative flux density measurements due to uncertainty in the zenith angle dependence of the E.W.A caused by ground reflections.

7.7 Partial Resolution Corrections.

The source 1648+05 is partially resolved by the full aperture E.W.A beam. A correction to the source peak flux density must be made to obtain the integrated flux density. The 1420 MHz brightness distribution model of Fomalont (1971) was used to calculate the partial resolution correction. The 1648+05 relative flux density measurement listed in Table 7.2 must be increased by 8 percent to correct for partial resolution. A 1 percent partial resolution correction was applied to the 0915-11 Table 7.2 relative flux density measurement.

7.8 Time Constant Correction.

Very slight corrections were applied to the Table 7.2

relative flux density measurements to correct for reductions in the peak source deflections due to the one second time constant.

7.9 E.W.A Diurnal Phase and Gain Variations.

A r.m.s error of 4 percent was assumed to result from diurnal variations of the relative gains and phasing of the six component sections of the E.W.A. These variations are not monitored by the E.W.A CAL.

7.10 Final Relative Flux Density Listing.

Table 7.4 lists the Table 7.2 SOURCE/CAL ratios after correction for non-linearity, partial resolution and time constant reductions.

The listed r.m.s error is the square root of the quadratic sum of the following r.m.s errors.

1. Confusion error.
2. Random error due to system noise, interference, scintillation and short term gain and phase instabilities.
3. Uncertainty in the E.W.A zenith angle relative gain.
4. Uncertainty in the non-linearity correction.
5. Uncertainty in the partial resolution corrections.
6. E.W.A diurnal phase and gain variations.

Table 7.4

Relative Flux Density Measurements.

Source	SOURCE/CAL	R.M.S Error (Percent)
0624-05	0.677	8.3
0915-11	2.774	6.6
1648+05	4.039	6.7
1932-46	0.664	8.1
2211-17	0.899	7.9

FIG. 7.1 . CROSS-SECTION OF THE E.W.A REFLECTING SURFACE.

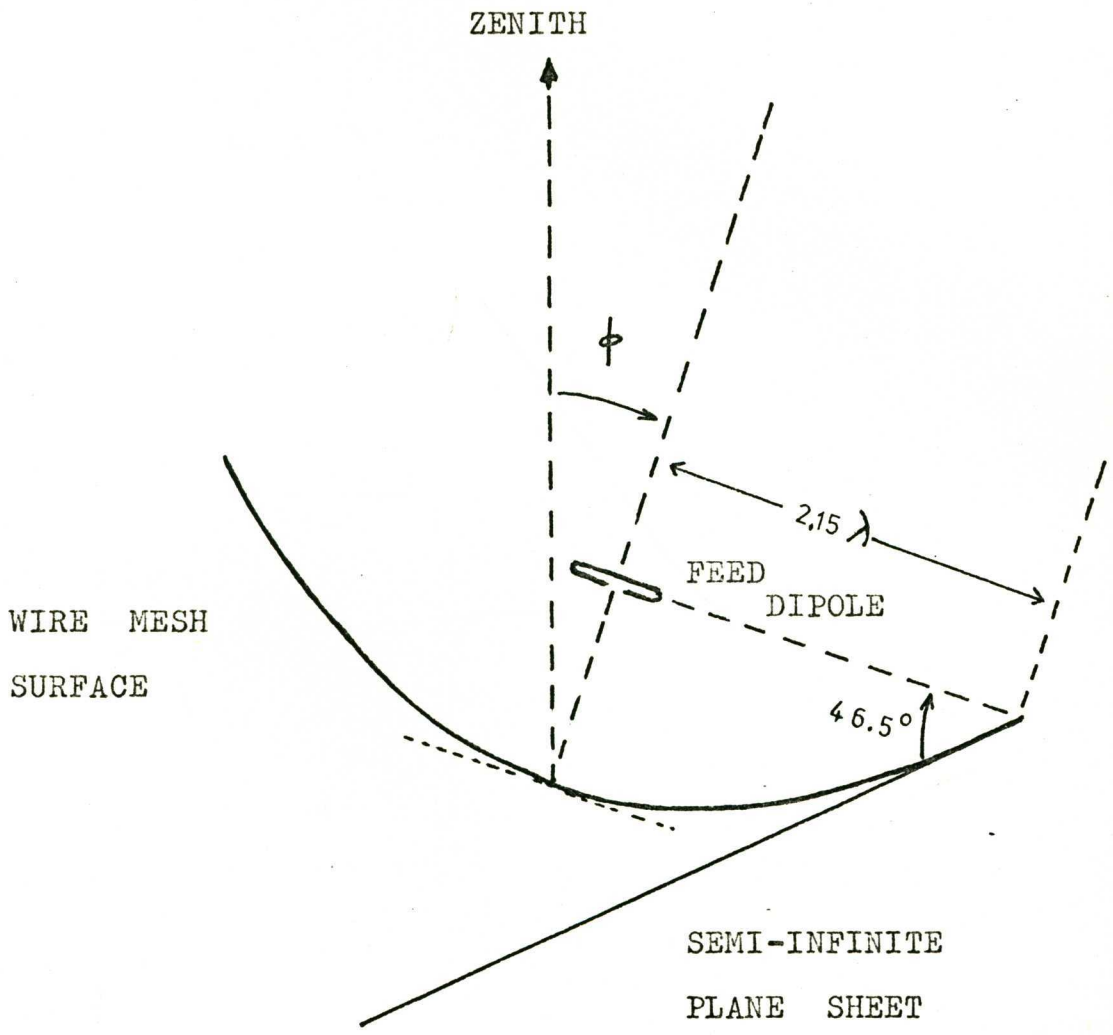

FIG. 7.2 . DIFFRACTION CALCULATION CO-ORDINATE SYSTEM .

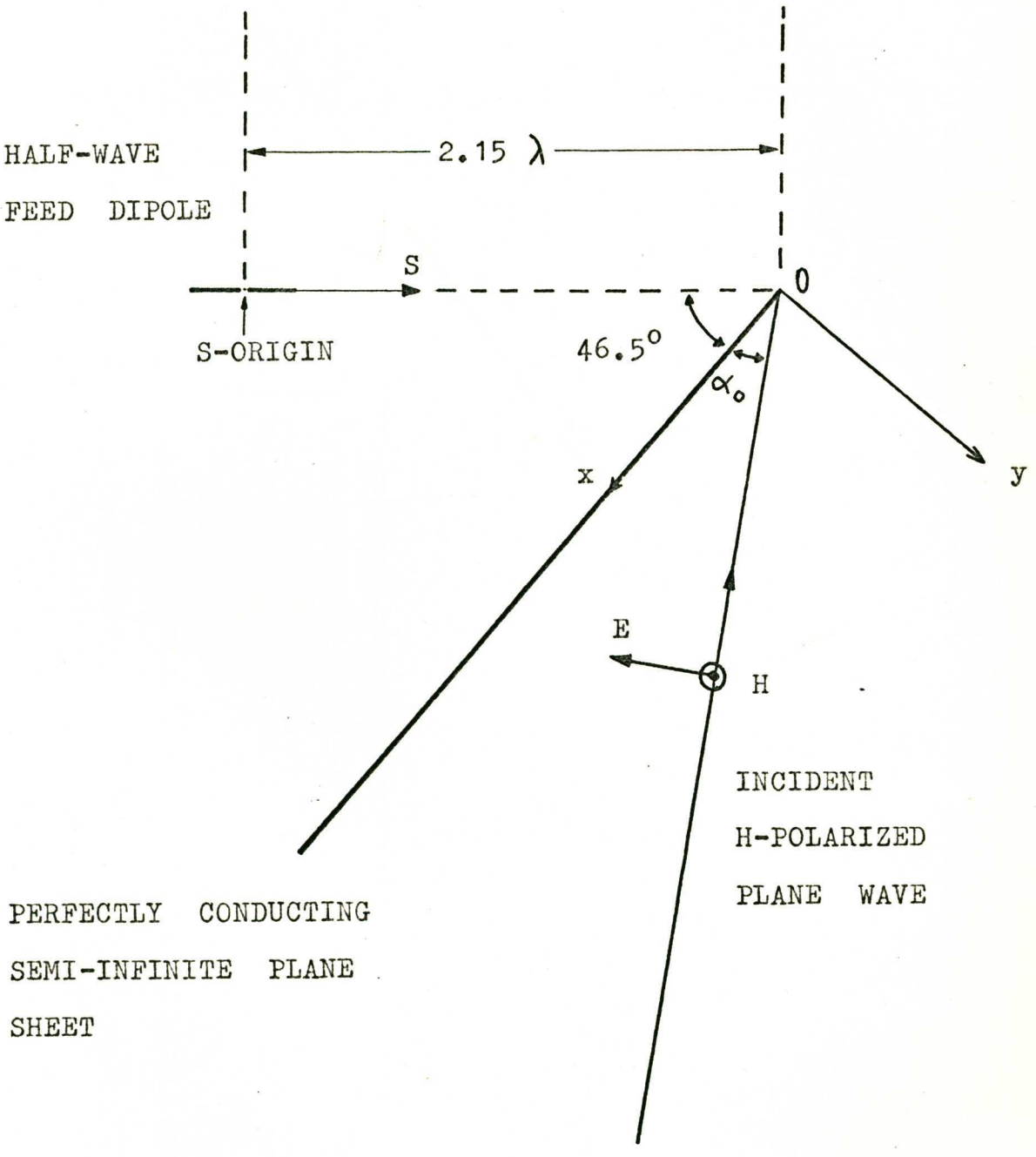

FIG. 7.3 . G/G_o AS A FUNCTION OF THE E.W.A ZENITHAL POINTING ANGLE.

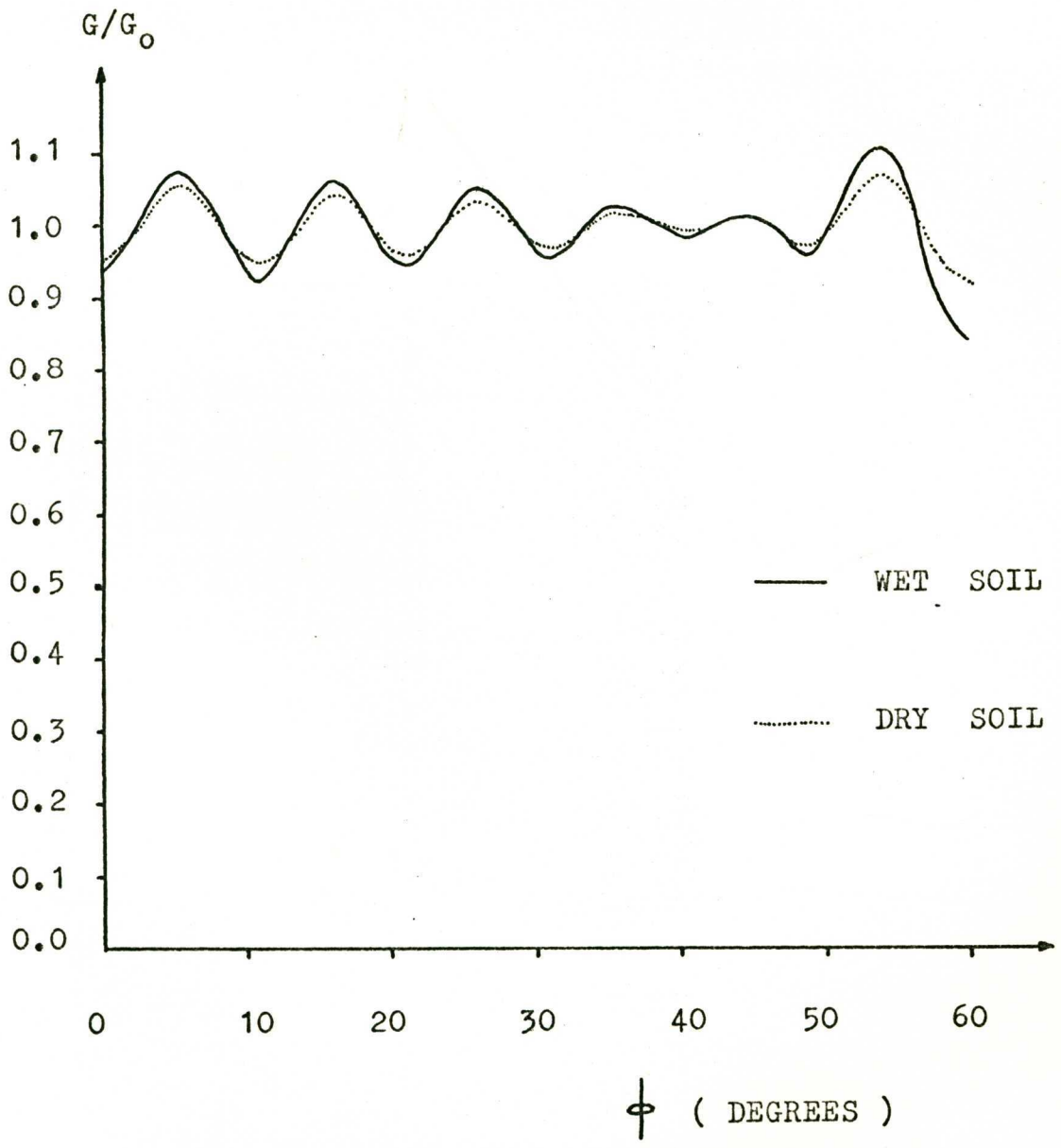

FIG. 7.4 . ARRANGEMENT FOR NON-LINEARITY EXAMINATION.

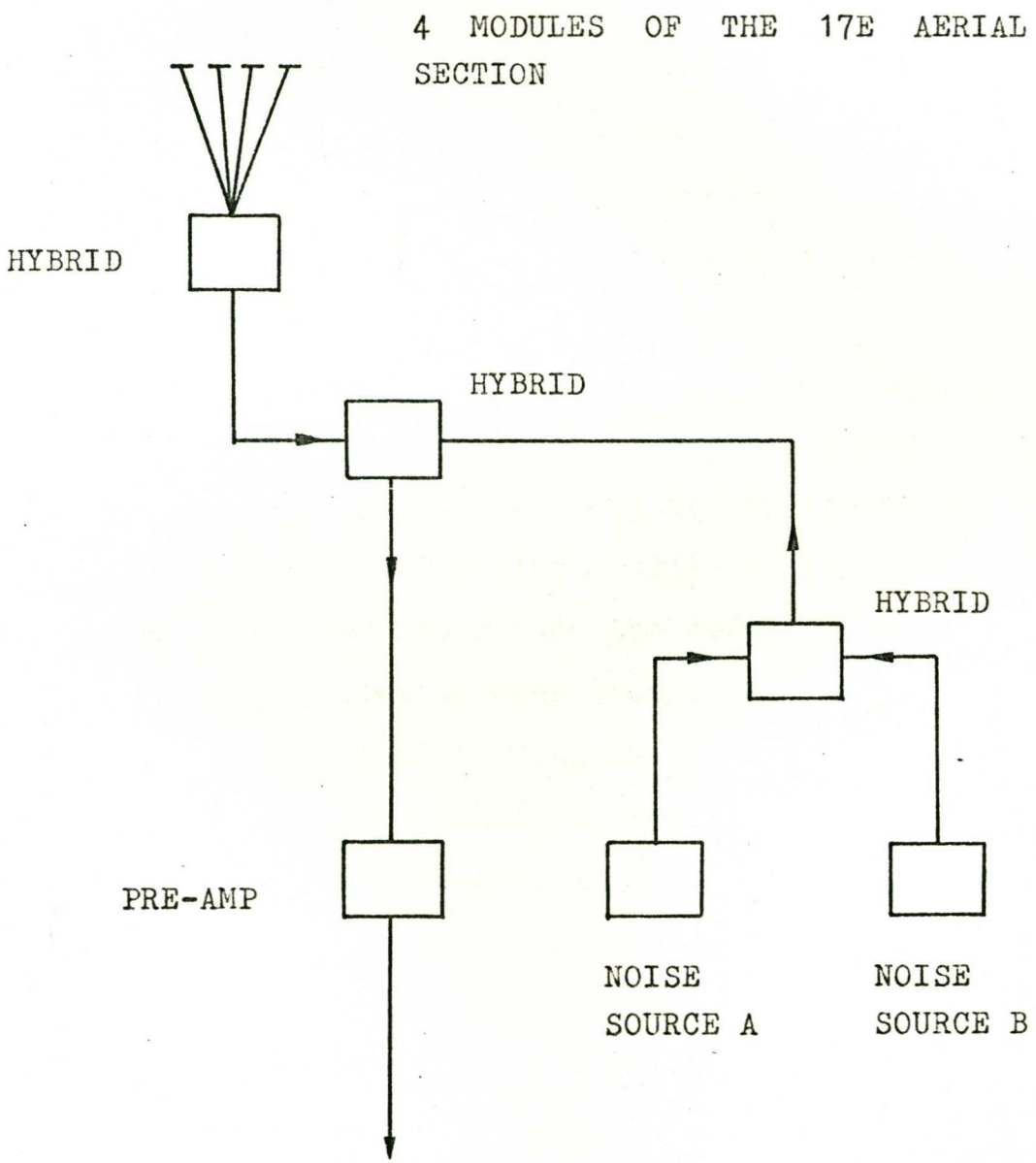

THE PRE-AMP OUTPUT CONNECTS TO THE OTHER SEVEN 17E PRE-AMPS AS SHOWN IN FIG. 2.1 .

CHAPTER 8.

DISCUSSION OF RESULTS.

8.1 Combination of Absolute and Relative Flux Density Measurements.

The absolute flux density measurements for the seven radiosources listed in Table 6.6 define the present 111 MHz flux density scale. The Table 6.6 flux densities are termed independent absolute flux densities and are re-listed in column 2 of Table 8.1.

The errors for the Table 6.6 flux densities are a compounding of the errors in the flux density scale common to all of the calibration sources and errors, peculiar to each source, relative to the flux density scale.

An attempt was made to reduce the effect of random and systematic error peculiar to each source by combining the Table 6.6 Category I absolute flux densities with the relative flux density measurements listed in Table 7.4.

The Category I flux density values (termed adjusted absolute flux densities) listed in column 3 of Table 8.1 satisfy the Table 7.4 relative flux density ratios and are chosen such that the mean ratio of this scale flux density (column 3) averaged over the five Category I sources to the independent absolute Category I flux densities listed in column 2 of Table 8.1 is unity.

Table 8.1

Independent and Adjusted Absolute Flux Densities.

(1)	(2)	(3)	(4)
	Absolute Flux Densities (Jy)		Ratio of Independent to Adjusted Flux Density.
Source	Independent	Adjusted	
0531+21	1633	-----	-----
0624-05	112.5	116.2	0.968
0915-11	465.3	476.3	0.977
1228+12	1696	-----	-----
1648+05	822.5	693.5	1.186
1932-46	118.5	113.9	1.040
2211-17	128.0	154.4	0.829

It is instructive to examine the dispersion of the ratios of the independently measured to the adjusted absolute flux densities for the Category I sources. The ratios are listed in column 4 of Table 8.1 and are shown in Fig 8.1. For a comparison, the ratios of independently measured to adjusted

absolute flux densities obtained from the Method II results of Wyllie at 408 MHz (which corresponds to the absolute flux density measurement method used at 111 MHz) for the five 408 MHz primary flux density calibration sources were calculated. The resulting distribution of ratios is shown in Fig 8.1.

For both the 111 MHz and 408 MHz Method II absolute flux density measurements the standard deviation of the distribution of ratios was 13 percent of the mean value.

The 111 MHz ratio value of 1.18 corresponds to the source 1648+05. This source has a r.m.s error for the independent absolute flux density measurement of 6.8 percent listed in Table 6.6. The estimated r.m.s error for the 1648+05 relative flux density measurement was 6.7 percent. It is probable that the lower values of r.m.s error listed for the Table 6.6 independent absolute flux densities are unrealistically low. The Table 6.6 r.m.s errors do not include estimates of the systematic errors, common to all sources, affecting the flux density scale or systematic errors peculiar to the individual source flux density measurements. Examination of Fig.8.1 suggests a minimun r.m.s error of 12 percent for the independent absolute flux density measurements listed in Table 6.6.

8.2 The RBC Flux Density Scale.

Roger, Bridle and Costain (1973), hereafter referred to as RBC, present what is claimed to be an internally consistent set of flux density scale revision factors for selected published flux densities in the range 10 MHz to 178 MHz. RBC derived the flux density scale revision factors by the following procedure.

(1) Measurements at 22.25 MHz due to Roger, Costain and Lacey (1969), hereafter referred to as RCL, measured with the 22 MHz T-array of the Dominion Radio Astronomy Observatory (described by Costain, Roger and Lacey 1969) were revised upwards by the factor 1.15. Additional and revised 22 MHz flux density measurements on the new scale are also listed in the RBC (1973) paper.

(2) RBC obtained a set of 38 spectra well fitted by a power-law relationship over the frequency range 22 MHz to 2695 MHz using the RBC and revised RCL 22 MHz measurements and the unrevised observations at the higher frequencies of 750, 1400 and 2695 MHz obtained from Kellermann, Pauliny-Toth and Williams (1969), hereafter referred to as KPW.

(3) RBC compared the 38 MHz (Williams, Kenderdine and Baldwin 1966) and the 178 MHz (Crowther and Clarke 1966, Clarke 1965, Wills and Parker 1966, Pilkington and Scott 1965, Gower, Scott and Wills 1967) flux density scales used by KPW with the flux densities interpolated from the power-law spectra

described in step(2) to derive the flux density scale revision factors.

(4) RBC define as primary data "recently published" (circa. 1973) flux density lists which were reasonably complete to the 3C flux density limit. The 86 MHz measurements of Artyukh, Vitkevich, Dagkesamanski and Kozhukhov (1969), hereafter referred to as AVDK, were used by RBC as primary data. A scale revision factor of 0.94 ± 0.03 to the RBC flux density scaling was determined by RBC for the AVDK flux densities.

The 85.5 MHz measurements of Mills, Slee and Hill (1958), hereafter referred to as MSH, were listed as secondary data. The MSH flux densities are listed as not requiring revision for consistency with the RBC flux density scale. RBC compared the AVDK flux densities with those measured by MSH over the declination ranges $0^\circ < \delta < +10^\circ$ and $-6^\circ < \delta < 0^\circ$.

The present 111 MHz flux density measurements include several 3C sources South of declination -6°. A comparison was made of the flux densities of sources common to the ADVK and MSH source flux density lists.

The AVDK instrument (described by Artyukh, Vitkevich and Dagkesamanski 1968) was the East-West array of a cross-type radiotelescope. The angular distance between the maximun and minimun of the telescope power pattern was 11 min arc in right ascension. The half-power width of the radiation pattern in declination was 4.7 degrees. For sources having angular diameters less than 10 min arc AVDK corrected their flux

densities for the effects of partial resolution. AVDK applied no corrections for partial resolution to sources having angular diameters greater than 10 min arc, these extended sources were excluded from the comparison of the MSH and AVDK flux density scales.

Sources listed in the MSH survey as possibly extended were also excluded from the AVDK/MSH flux density scale comparison.

Fig 8.2 shows the AVDK to MSH flux density ratios plotted as a function of MSH flux density. The ADVK/MSH mean flux density ratio clearly increases for the MSH flux density less than 50 Jy region of the Fig 8.2 plot. The mean ADVK/MSH flux density ratio for MSH flux density less than 50 Jy was 1.04 ± 0.04 (39 sources). The mean ADVK/MSH flux density ratio for MSH flux density greater than 50 Jy was 0.88 ± 0.04 (21 sources).

The present 111 MHz absolute flux density calibration sources are all strong sources. Consequently it is of interest to examine in more detail the AVDK/MSH flux density ratios for MSH flux density greater than 50 Jy.

Fig 8.3 shows the AVDK/MSH flux density ratios for MSH flux density greater than 50 Jy plotted as a function of declination. The number of data points is very limited (21 sources). The mean ADVK/MSH flux density ratios for the Fig 8.1 data points for the declination zones $0^\circ < \delta < +10^\circ$, $-10^\circ < \delta < 0^\circ$ and $\delta < -10^\circ$ are listed in Table 8.2.

Table 8.2

Mean AVDK/MSH Flux Density Ratios for Sources having MSH Flux Density greater than 50 Jy.

Declination Zone.	ADVK/MSH Ratio	Standard Error	Number of Sources
$0^\circ < \delta <_+ 10^\circ$	0.87	0.02	9
$-10^\circ < \delta < 0^\circ$	0.79	0.06	6
$\delta <- 10^\circ$	1.00	0.09	6

The mean AVDK/MSH flux density ratios for sources having MSH flux density greater than 50 Jy are lower than the listed RBC mean AVDK/MSH flux density ratios for the corresponding declination zones.

(5) The remaining RBC primary data source lists are the revised 10.03 MHz flux density measurements of Bridle and Purton (1968) obtained with the 10 MHz array of the Dominion Radio Astronomy Observatory, additional and revised 10.03 MHz flux densities listed by RBC (1973) and the 1400 MHz measurements by Bridle, Davis, Fomalont and Lequeux (1972). The secondary data source lists are listed in the RBC (1973) paper.

8.3 Comparison of the Molonglo 111 MHz Flux Density Scale to the RBC Flux Density Scale.

The source flux density $S(\nu)$ is related to the spectral index $\alpha(\nu)$ and the frequency ν by

$$S(\nu) = S_o \nu^{-\alpha(\nu)} \quad (1)$$

where S_o is a constant.

The calibration source flux density values on the RBC flux density scale were derived from the RBC revised primary and secondary source lists by the following procedure.

(1) The secondary data Parkes 408 MHz, 1410 MHz and 2650 MHz flux density measurements were taken from the original zone catalogues i.e Bolton et al. (1964), Price and Milne (1965), Day et al. (1966) and Shimmins et al. (1966). The zone scaling factors used to convert the flux density values from the original zone catalogues to the combined Parkes Catalogue (1969) were not applied.

(2) The RBC flux density revision factor of 0.94 was applied to the AVDK flux density measurements. Revision factors as listed by RBC were applied to the remaining primary and secondary source lists.

(3) Four of the 111 MHz absolute flux density calibration sources i.e 0915-11, 1228+12, 1648+05 and 2211-17 are

classified by RBC as having power-law spectra i.e spectral index constant for ν less than 2000 MHz.

For each of the four power-law (RBC classified) sources the revised flux density data on a log S - log ν plot was fitted with a straight line by the method of least squares in which each flux density was weighted inversely to the square of its standard error. The standard error was a compounding of the listed flux density standard error and the RBC revision factor standard error. The listed AVDK flux density errors are the standard errors due to the random scatter of the measurements. The standard error used in the weighting of the AVDK flux densities was a compounding of the quoted 3 percent standard error in the zenith angle dependence of the AVDK aerial effective area, a 3 percent standard error due to non-linearity uncertainty, a 3 percent standard error in the flux density calibration, a 3 percent standard error in the RBC revision factor, a r.m.s confusion error quoted by AVDK of 2 Jy and the random standard error. The standard error of the MSH flux densities was taken as 10 percent.

The source 0531+21 is classified by RBC as having a constant spectral index for ν greater than 200 MHz and as having the second derivative of the spectrum positive for ν less than 200 MHz on the log S - log ν plane. A power-law was fitted to the flux density data points for ν greater than or equal to 178 MHz. For ν less than 178 MHz a curve was drawn by eye through the data points on the log S - log ν

plane continuous with the higher frequency power-law relationship.

The source 0624-05 spectrum is classified by RBC as power-law for ν less than 1000 MHz and curved on the log S - log ν plane for ν greater than 1000 MHz. A power-law was fitted to the 0624-05 flux density data points for ν less than 1000 MHz.

The source 1932-46 spectrum's second derivative is negative on the log S - log ν plane. A curve was drawn by eye through the log S - log ν data points.

The 111.17 MHz interpolated flux densities derived from the flux density calibration source spectra constructed in accordance with the RBC flux density scale revision factors are listed in Table 8.3.

Table 8.3

Interpolated 111.17 MHz Flux Densities.

(RBC Flux Density Scale Revision Factors).

Source	Interpolated Flux Density (Jy)
0531+21	1816
0624-05	105.7
0915-11	455.8
1228+12	1581
1648+05	578.1
1932-46	117
2211-17	117.4

The 111 MHz interpolated flux density value for 1932-46 was not as well defined as for the other six calibration source interpolated flux densities for the following reasons.

a. The strong curvature of the source spectrum on the log S - log v plane.

b. The large Southern declination of 1932-46 results in the complete lack of RBC primary data flux densities. The 1932-46 interpolated 111.17 MHz flux density depends heavily on the MSH 85.5 MHz flux density which has a standard error of at least 10 percent.

The 85.5 MHz flux densities for 0531+21 and 1228+12 were obtained from the measurements by Little (1958), which formed part of the MSH absolute flux density scale calibration.

Suggestions of variability of the 0624-05 and 2211-17 flux densities at 80 MHz result from the observations of Slee and Higgins (1975). Slee and Higgins made a comparison of the 80 MHz flux density measurements of 100 strong sources common to the Culgoora-I (Slee and Higgins 1973) and the Culgoora-II (Slee and Higgins 1975) source lists. Both source lists were compiled from observations using the Culgoora radioheliograph. An interval of approximately three years separated the Culgoora-I and Culgoora-II observations.

The flux density measurements for 0624-05 and 2211-17 were reported as 25 and 13 percent higher for the Culgoora-II list as compared to the Culgoora-I list. A test of the hypothesis that the Culgoora-I and the Culgoora-II 0624-05 and 2211-17 measurements come from the same population respectively indicates that there is a probability of less

than 1 percent and 6 percent of the 0624-05 and 2211-17 flux density measurement differences between the Culgoora-I and Culgoora-II lists arising by chance respectively.

If the observed flux density variations for 0624-05 and 2211-17 at 80 MHz are shown conclusively as being intrinsic to the sources then the suitability of 0624-05 and 2211-17 as low frequency flux density calibrators is questionable.

Table 8.4 lists the ratios of the independent absolute flux density and the adjusted absolute flux density to the interpolated 111.17 MHz RBC flux density for each calibration source.

The mean of the independent absolute flux density to the RBC 111.17 MHz interpolated flux density ratios and the mean of the adjusted absolute flux density to the RBC 111.17 MHz interpolated flux density ratios, averaged over the calibration sources, was calculated for the following weighting schemes.

Case (1). The flux density ratio for each source given equal weight.

Case (2). The mean of the equally weighted flux density ratios for the four very strong sources only i.e 0531+21, 0915-11, 1228+12 and 1648+05.

Case (3). Possible variable sources 0624-05 and 2211-17 excluded. The remaining five sources equally weighted.

Case (4). Sources 0624-05, 1932-46 and 2211-17 given half the weighting of the very strong sources.

Table 8.4

Comparison of the Independent and Adjusted Absolute Flux Densities with the RBC 111.17 MHz Interpolated Flux Densities.

Source	Ratio of Independent Absolute to RBC Flux Density.	Ratio of Adjusted Absolute to RBC Flux Density.
0531+21	0.899	-----
0624-05	1.064	1.100
0915-11	1.021	1.045
1228+12	1.073	-----
1648+05	1.423	1.200
1932-46	1.013	0.974.
2211-17	1.090	1.315

Case (5). 1932-46 given half-weighting of the other six calibration sources.

Table 8.5 column 2 lists the mean values of the independent absolute flux density to the RBC interpolated flux density ratios, averaged over the seven calibration

Table 8.5

Comparison of the Molonglo 111 MHz Flux Density Scale to the RBC Flux Density Scale.

Weighting Case	Category I and II Independent Absolute to RBC Flux Density Mean Ratios.		Category I Adjusted and Category II Independent Absolute to RBC Flux Density Mean Ratios.	
	Mean	Standard Error	Mean	Standard Error
(1)	1.08	0.06	1.09	0.05
(2)	1.10	0.11	1.05	0.06
(3)	1.09	0.09	1.04	0.05
(4)	1.09	0.07	1.07	0.06
(5)	1.09	0.06	1.10	0.05
Mean	1.09 ± 0.08		1.07 ± 0.06	

sources, for Cases (1) to (5).

Table 8.5 column 3 lists the mean values of the combined

Category I adjusted absolute flux density and the Category II independent absolute flux density to the RBC interpolated flux density ratios for Cases (1) to (5).

The sample standard deviation of the seven independent absolute flux density to RBC interpolated flux density ratios was 16.3 percent of the mean value. The sample standard deviations of the independent and the adjusted Category I absolute flux density to the RBC interpolated flux density ratios, for the five Category I sources, were 17.1 and 13.4 percent of the mean values respectively.

As a consequence of the small improvement in the sample standard deviation of the adjusted absolute Category I flux density to RBC interpolated flux density ratios in comparison to the sample standard deviation of the independent Category I and II absolute flux density to RBC interpolated flux density ratios a weighting scheme favouring the Category I adjusted absolute flux density measurements was not devised for the comparison of the Molonglo 111.17 MHz absolute flux density scale with the RBC flux density scale.

The ratio of the Molonglo 111.17 MHz absolute flux density scale to the RBC flux density scale, resulting from the combination of the mean flux density scale ratios of columns 2 and 3 of Table 8.5, is 1.08 ± 0.07 .

The quoted standard error for the flux density scale comparison arises from the scatter of the flux density ratios within each weighting scheme considered. There is an additional

standard error of 5 percent in the absolute calibration of the 111.17 MHz Molonglo flux density scale resulting from the 3 percent standard error in the thermal calibration of the scale and the 4 percent standard error in the reference aerial effective area calculation.

8.4 Discussion.

The Molonglo 111.17 MHz absolute flux density scale, defined by the absolute flux density measurements obtained for seven sources, is 8 $\pm$ 9 percent higher than a flux density scale defined by interpolated 111.17 MHz flux densities, for the same seven sources, derived from spectra constructed in accordance with the RBC flux density scale revision factors.

The Molonglo 111.17 MHz absolute flux density measurements listed in Table 8.1 do not provide high accuracy flux densities for the individual calibration sources. The standard error pertaining to the individual source flux density measurements was estimated approximately at 12 percent. Collectively the seven source absolute flux density measurements define a 111.17 MHz absolute flux density scale having a standard error of 7 percent. The 7 percent flux density scale standard error is compounded from the following error sources. Firstly, a 5 percent standard error in the thermal calibration of the absolute flux density scale and the reference aerial effective area calculation. Secondly, a 5 percent standard error arising from the scatter of the seven calibration source flux density measurements relative to the absolute flux density scale.

The calibration source spectra constructed in accordance with the RBC flux density scale revision factors are shown in Figs 8.4 to 8.6 . The plotted 111.17 MHz flux density measurements are the adjusted Category I and the independent Category II absolute flux density measurements.

Notes on Individual Calibration Sources.

(a) 1648+05 The adjusted absolute flux density is 20.0 percent above the interpolated RBC flux density. The independent absolute flux density is 42.3 percent above the interpolated RBC flux density. This measurement displays the

largest difference of either the independent or adjusted absolute flux density , for any of the calibration sources, in comparison to the RBC interpolated flux density. In common with 2211-17, 1648+05 exhibits the largest difference between the independent and adjusted absolute flux densities.

During the March and April 1976 observing sessions the calibration source independent absolute flux densities were approximately calculated as a check upon the progress of the observations. In the case of 1648+05 the relative phase angle of the multiplied source voltages was altered significantly during the course of each of the observing sessions to examine whether the high flux density value of 1648+05 in comparison to the interpolated RBC flux density was due to a phase error present in the observe receiving system mode. No significant dependence of the measured 1648+05 flux density upon the relative phase of the multiplied source voltages was found.

The majority of the March 1976 observations of 1648+05 were obtained for an ambient temperature of + 11 ^{o}C. The ambient temperature for the majority of the April 1976 observations was approximately - 4 ^{o}C. The March and April 1976 absolute flux density measurements do not display a difference that could be attributed to the ambient temperature difference for 1648+05 between the two observing sessions.

Possible causes producing the large difference between the independent absolute flux density measurement and the interpolated RBC flux density for 1648+05, apart from a gross underestimation of the 111.17 MHz flux density for 1648+05 on

the RBC flux density scale, are as follows.

a. Diffraction by fixed objects in the proximity of the reference aerial e.g wire fences and the North-South arm of the Molonglo Cross.

b. Reflection and re-radiation from the Western arm of the Molonglo Cross. This possibility was not eliminated for 1648+05 by the Western arm reflection and re-radiation experiment.

c. Diffraction due to the major discontinuity in the TM reflection coefficient amplitude across the reference aerial highly conducting ground screen/soil boundary. No attempt was made to calculate the consequences of the reference aerial ground screen boundary diffraction upon the reference aerial effective area calculation. Consequently the possibility remains that a major contribution to the differences between the independent absolute flux densities and the interpolated RBC flux densities for each of the seven calibration sources is due to the effects of the reference aerial ground screen boundary diffraction. Since the calibration sources are spread over a 70 degree range of meridional angle the assumption is made (in the absence of firm experimental or theoretical justification) that the net effect of diffraction from fixed objects in the proximity of the reference aerial and of diffraction due to the TM reflection coefficient amplitude discontinuity upon the Molonglo 111.17 MHz flux density scale is negligible due to the assumed large changes in the relative

phase angles of the direct and diffracted electric fields as a function of the calibration source declination.

d. Deviation of the real dipole and ground screen radiation pattern from the idealized dipole and ground screen radiation pattern assumed for the reference aerial effective area calculation.

e. The possible presence of confusing sources.

(b) 2211-17 The adjusted absolute flux density is 31.5 percent above the interpolated RBC flux density. Possible causes producing the large difference between the adjusted absolute flux density measurement and the interpolated RBC flux density for 2211-17 are as follows.

a. The interpolated RBC flux density may be an underestimation of the true 111.17 MHz flux density.

b. The relative gain of the East-West aerial at the pointing declination of 2211-17 may be significantly above unity due to ground reflections which may result in the overestimation of the flux density of 2211-17 relative to the other Category I source flux densities measured by the East-West aerial.

c. The source flux density may be variable at 111.17 MHz.

8.5 The CKL/K/KPW Flux Density Scales.

A number of papers present evidence that the flux density scales established by Conway, Kellermann and Long (1963), hereafter abbreviated as CKL, and its revision by Kellermann, Pauliny-Toth and Williams (KPW 1969) are systematically low at frequencies below 750 MHz.

The CKL/KPW flux density scales are based ultimately upon absolute flux density measurements made upon the primary calibration source Cas A.

Cas A is so much more powerful than most other sources that non-linearity in the receiver response can cause problems in the direct comparisons with weak sources.

The flux density scaling at each of the frequencies of the CKL and KPW scales was defined by the spectra of a small number of moderately strong secondary calibration sources, which were selected as having simple power-law spectra.

Kellermann (1964b), hereafter occasionally abbreviated as K, using a modified procedure for relating the intensity of weaker sources to those determined absolutely indicated that the CKL scale might be low by 8 percent at 38 MHz and 178 MHz.

Scott and Shakeshaft (1971) list the flux densities at 81.5 MHz of 13 radiosources measured relative to Cas A and Cyg A. The absolute flux density values adopted by Scott

and Shakeshaft for Cas A and Cyg A were obtained from the absolute measurements by Parker (1968). The Scott and Shakeshaft measurements show consistency with interpolated KPW flux densities for flux densities greater than about 400 Jy. The Scott and Shakeshaft flux densities are in excess of the KPW flux density scale by about 22 ± 5 percent for their flux densities below about 300 Jy.

Scott and Shakeshaft cite the unpublished measurements of Collins (1968) at Cambridge of the relative flux densities of Cas A and weaker sources that suggested that the KPW scale was 12 ± 6 percent low at 240 MHz.

Wyllie (1969a) made a comparison of the 408 MHz flux densities of sources common to the corrected CKL flux density scale source catalogue of Kellermann (1964b) and the Wyllie complete set of calibration sources, that consisted of the five primary calibration sources used for the absolute flux density scale established by Wyllie at 408 MHz and 37 secondary flux density calibration sources on the same scale (Wyllie 1969b).

Wyllie obtained the result that the Molonglo flux densities at 408 MHz are on the average 9 ± 3 percent higher than those listed in Kellermann's catalogue.

Wyllie also compared the 408 MHz flux densities of sources common to the CKL catalogue and the Wyllie complete set of calibration sources. The Molonglo 408 MHz flux densities were found to be 11 percent higher than the interpolated CKL 408 MHz flux densities on average. Wyllie concluded that the

CKL and K scales which are based mainly on Northern hemisphere sources either contain a systematic effect dependent upon declination or are systematically low by about 10 percent at 408 MHz.

Munro and Conway (1972) made a comparison between two sets of flux density measurements of 40 radiosources at 408 MHz. The first set of flux density measurements used the pencil beams of the Molonglo radiotelescope and was calibrated using the absolute flux density scale established by Wyllie. The second set of measurements was made using an interferometer at Jodrell Bank and was calibrated on the CKL scale. The result of the comparison was that to be consistent with the Wyllie scale the CKL flux densities should be increased by 1.087 ± 0.028 .

Neill and Jauncey (1971) at Arecibo found the KPW scale to be 12 ± 3 percent lower at 430 MHz than that of Wyllie.

The 38 MHz flux density scale used for the KPW catalogue is close to the 38 MHz scale used for the CKL catalogue. At 178 MHz the KPW flux density scale was based on CKL. The KPW 750 and 1400 MHz flux density scales were based on the scale established by Kellermann (1964 a, b), which is close to the CKL scale at these frequencies.

The KPW 38 MHz flux densities required an upward revision of 18 percent for consistency with the RBC flux density scale for KPW flux densities less than 550 Jy. RBC list no revision for consistency with the RBC flux density scale for KPW flux

densities greater than 550 Jy. At 178 MHz RBC list an upward revision of 9 percent for KPW flux densities less than 160 Jy and no revision for KPW flux densities greater than 160 Jy for consistency with the RBC scale.

Braude et al. (1970) constructed standard spectra for 57 sources having simple power-law spectra in the frequency range 12.6 to 5000 MHz. The standard spectra were constructed from absolute measurements at the frequencies 12.6, 14.7, 16.7, 20.0 and 26.0 MHz (Braude et al. 1969 a, c), NRAO measurements at 750, 1400, 2650 and 5000 MHz (Kellermann et al. 1969, Pauliny-Toth et al. 1966, Pauliny-Toth and Kellermann 1968, Kellermann et al. 1968), Parkes measurements at 408, 1400 and 2695 MHz (Day et al. 1966, Shimmins et al. 1968) and the Wyllie 408 MHz measurements (Wyllie 1969 a, b).

Braude et al. found that the CKL flux densities were low by 28 percent and 8 percent in comparison to the interpolated standard spectra flux densities at 38 and 178 MHz respectively.

The accuracy of defining flux density scales relative to the primary calibration source Cas A is limited by the inaccuracy of flux density measurements relative to Cas A and also by uncertainty in the absolute spectrum of Cas A and the rate of the Cas A secular flux density decrease.

Baars and Hartsuijker (1972) present an analysis of the absolute spectrum of Cas A using all available absolute measurements up to 1971. The resulting spectrum was steeper than that obtained by KPW, having a 3.8 percent increase (epoch 1965.0) in comparison with KPW of the computed flux density

at 1000 MHz. Baars and Hartsuijker comment that the flux density scales of CKL, K and KPW at 408 MHz are based on Cas A flux densities of 5746, 6046 and 6090 Jy (epoch 1965.0) respectively. These values are low by 11, 6 and 6 percent respectively with respect to the Cas A 408 MHz flux density (epoch 1965.0) determined from the Baars and Hartsuijker spectrum. On the Wyllie scale the Cas A 408 MHz flux density (epoch 1965.0) is 1.6 percent above the Baars and Hartsuijker value.

The corrections to bring the CKL, K and KPW 178 MHz flux density scales to the 178 MHz scale based on the absolute spectrum of Cas A determined by Baars and Hartsuijker were upward revisions of 14, 7 and 8 percent respectively.

Wills (1973) investigated all absolute flux density measurements of Cas A in the frequency range 38 MHz to 16 GHz available by early 1972. Following a revision of the spectrum of Cas A Wills suggested that the KPW flux density scale is low by 24, 22 and 7 percent at 38, 178 and 1400 MHz respectively.

The varied investigations described by the papers listed previously present considerable evidence for the existence of a depression in the CKL/K/KPW scales for frequencies below about 750 MHz.

There also exists evidence, presented in most detail by Scott and Shakeshaft at 81.5 MHz and in less explicit form by RBC at 38 and 178 MHz, that the scaling factor to correct the KPW scale at the lower frequencies has a dependence upon the strength of the sources.

8.6 Comparison of the Molonglo 111.17 MHz Flux Density Scale to the CKL/K/KPW Flux Density Scales.

The Category I flux densities used in the flux density scale comparisons were the averages of the independent and adjusted absolute flux densities.

A comparison was made of the 111.17 MHz flux densities of the six sources common to the CKL catalogue and the set of Molonglo 111.17 MHz absolute flux density calibrators.

The interpolated 111.17 MHz CKL flux densities are listed in Table 8.6. Also listed is the ratio of the 111.17 MHz Molonglo flux density to the interpolated CKL flux density for each source.

The mean ratio for the six comparison sources, where the ratio for each source was equally weighted, of the 111.17 MHz Molonglo absolute flux density to the CKL flux density was 1.25 ± 0.12 .

Caution must be applied to the interpretation of the mean flux density ratio of the two scales for the following reasons.

(1) A very limited number of sources were used in the flux density scale comparison. Scatter of the individual CKL flux densities relative to the CKL scale introduces uncertainty to the mean flux density ratio for the two sets of flux density estimates.

(2) All of the comparison sources are South of declination + 21^{o}. Declination dependent effects may be present in the flux density scales.

(3) The CKL flux density values used in the comparison of the two sets of flux density estimates range from 1738 to 85 Jy i.e a range of 20 to 1 in source strength. If there exists a source strength dependence in the CKL flux density scale at 111.17 MHz then the large flux density range of the comparison sources complicates the interpretation of the mean flux density ratio for the two sets of flux density estimates.

(4) The CKL spectra for the very strong sources 0531+21, 1228+12 and Cyg A were based upon flux density measurements relative to Cas A i.e the spectra were not measured on the flux density scale based upon the average spectrum of the seven secondary CKL calibration sources. Conway et al. note that because of the different scaling procedure the spectra of 0531+21, 1228+12 and Cyg A cannot be strictly compared to the spectra of the remaining sources listed in the CKL catalogue.

Table 8.7 lists the 111.17 MHz interpolated flux densities on the scale of Kellermann (1964 b) for the six sources common to the Kellermann (1964 b) catalogue and to the set of Molonglo 111.17 MHz absolute flux density calibrators. Listed also is the ratio of the 111.17 MHz Molonglo flux density to the K flux density for each source.

The mean ratio for the six sources, where the ratio for each source was equally weighted, of the 111.17 MHz Molonglo

absolute flux density to the K flux density was 1.22 ± 0.11 .

The comparison of the 111.17 MHz Molonglo flux density scale to the KPW scale was very restricted for the following reasons.

(1) There are only four sources common to the KPW catalogue and the set of Molonglo 111.17 MHz absolute flux density calibrators.

(2) The four common sources are either strong or very strong sources. The two Southern weaker sources (0624-05 and 2211-17) used in the comparison of the 111.17 MHz Molonglo scale to the CKL and K scales are not included in the KPW catalogue. If there exists a source strength dependence in the KPW scale of the form claimed by Scott and Shakeshaft then the mean ratio of the 111.17 MHz Molonglo to KPW flux densities will be biased downwards.

Table 8.8 lists the 111.17 MHz interpolated KPW flux density and the ratio of the 111.17 MHz Molonglo flux density to the KPW flux density for each comparison source.

The mean ratio for the four comparison sources, where the ratio for each source was equally weighted, of the 111.17 MHz Molonglo absolute flux density to the KPW flux density was 1.11 ± 0.10 .

Table 8.6

Comparison of 111.17 MHz Molonglo and CKL Flux Density Scales.

Source	S_{CKL} (Jy)	$\frac{S_{Molonglo}}{S_{CKL}}$
0531+21	1738	0.940
0624-05	85.3	1.341
0915-11	405.2	1.162
1228+12	1679	1.010
1648+05	506.6	1.496
2211-17	89.6	1.576

Mean $S_{Molonglo} / S_{CKL}$ Ratio = 1.25 ± 0.11

Table 8.7

Comparison of 111.17 MHz Molonglo and K Flux Density Scales.

Source	S_K (Jy)	$\frac{S_{Molonglo}}{S_K}$
0531+21	1674	0.976
0624-05	90.6	1.263
0915-11	450.7	1.045
1228+12	1595	1.063
1648+05	533.1	1.422
2211-17	89.8	1.572

Mean $S_{Molonglo} / S_K$ Ratio = 1.22 $\pm$ 0.10

Table 8.8

Comparison of 111.17 MHz Molonglo and KPW Flux Density Scales.

Source	S_{KPW} (Jy)	$\frac{S_{Molonglo}}{S_{KPW}}$
0531+21	1800	0.907
0915-11	428	1.100
1228+12	1542	1.100
1648+05	564	1.344

Mean $S_{Molonglo} / S_{KPW}$ Ratio = 1.11 $\pm$ 0.09

Table 8.9

Comparison of MSH/Little 85.5 MHz Flux Densities with 85.5 MHz RBC Flux Densities.

Source	S_{RBC} (Jy)	$S_{MSH/Little}$ (Jy)	$\frac{S_{MSH/Little}}{S_{RBC}}$
0531+21	1950	2300*	1.179
0624-05	122.8	120	0.977
0915-11	586.7	690	1.176
1228+12	1951	2430*	1.246
1648+05	755.1	890	1.179
1932-46	141†	141	1.000
2211-17	154.3	127	0.823

Mean $S_{MSH/Little} / S_{RBC}$ Ratio = 1.08 $\pm$ 0.06

* Little (1958)

† Large uncertainty

Table 8.9 lists the 85.5 MHz flux densities for the seven 111 MHz calibration sources interpolated from the spectra constructed in accordance with the RBC revision factors.

The ratio of the 85.5 MHz MSH and Little (1958) flux density to RBC flux density for each source is listed in Table 8.9.

The mean ratio for the seven comparison sources, where the ratio for each source was equally weighted, of the 85.5 MHz MSH/Little to 85.5 MHz RBC flux density was 1.08 $\pm$ 0.06 .

8.7 Conclusion.

The 111.17 MHz Molonglo absolute flux densities, averaged over six comparison sources, were 25 $\pm$ 12 and 22 $\pm$ 11 percent above the flux densities defined on the CKL and K scales respectively and , averaged over four comparison sources, were 11 $\pm$ 10 percent above the flux densities defined on the KPW scale.

The 111.17 MHz Molonglo absolute flux densities, averaged over seven comparison sources, were 8 $\pm$ 9 percent above the flux densities defined on the RBC scale.

The flux density scale ratios need to be treated cautiously for reasons already elaborated. The number of 111.17 MHz Molonglo absolute flux density measurements is insufficient to allow investigation of the dependence of the flux scale ratios upon declination or source strength.

The 111.17 MHz Molonglo flux density measurements are of limited value for the following reasons.

(1) An approximate calculation (Chapter 7) suggested that ground reflections cause significant variations at 111.17 MHz of the E.W.A's gain. The variations in the E.W.A's gain are a function of the E.W.A pointing zenith angle. Consequently, at 111.17 MHz accurate relative flux density measurements are not available. The availability of accurate relative flux density measurements would have resulted in accurate individual absolute flux density measurements for the Category I sources on the 111.17 MHz Molonglo scale.

(2) The effect of diffraction at the reference aerial ground screen boundary may contribute a significant systematic error to the individual independent absolute flux density measurements and systematically raise or lower the overall scale.

Figs 11.12 and 11.13 contained in Born and Wolf which show a two-dimensional representation of the diffraction of a normally incident H-polarized plane wave by a perfectly conducting half-plane support the suggestion of significant ground screen boundary diffraction.

FIG. 8.1 . RATIOS OF THE INDEPENDENT TO THE ADJUSTED ABSOLUTE FLUX DENSITIES.

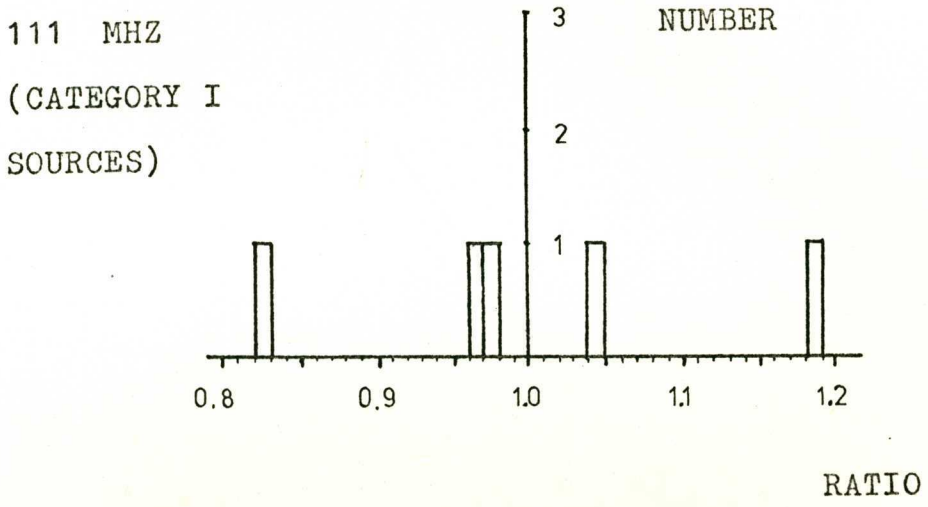

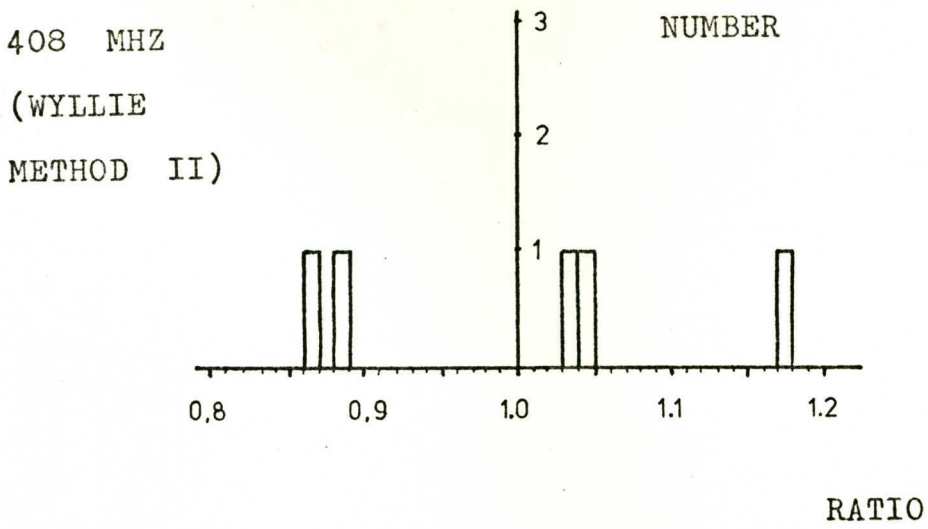

FIG. 8.2 . COMPARISON OF AVDK AND MSH FLUX DENSITIES.

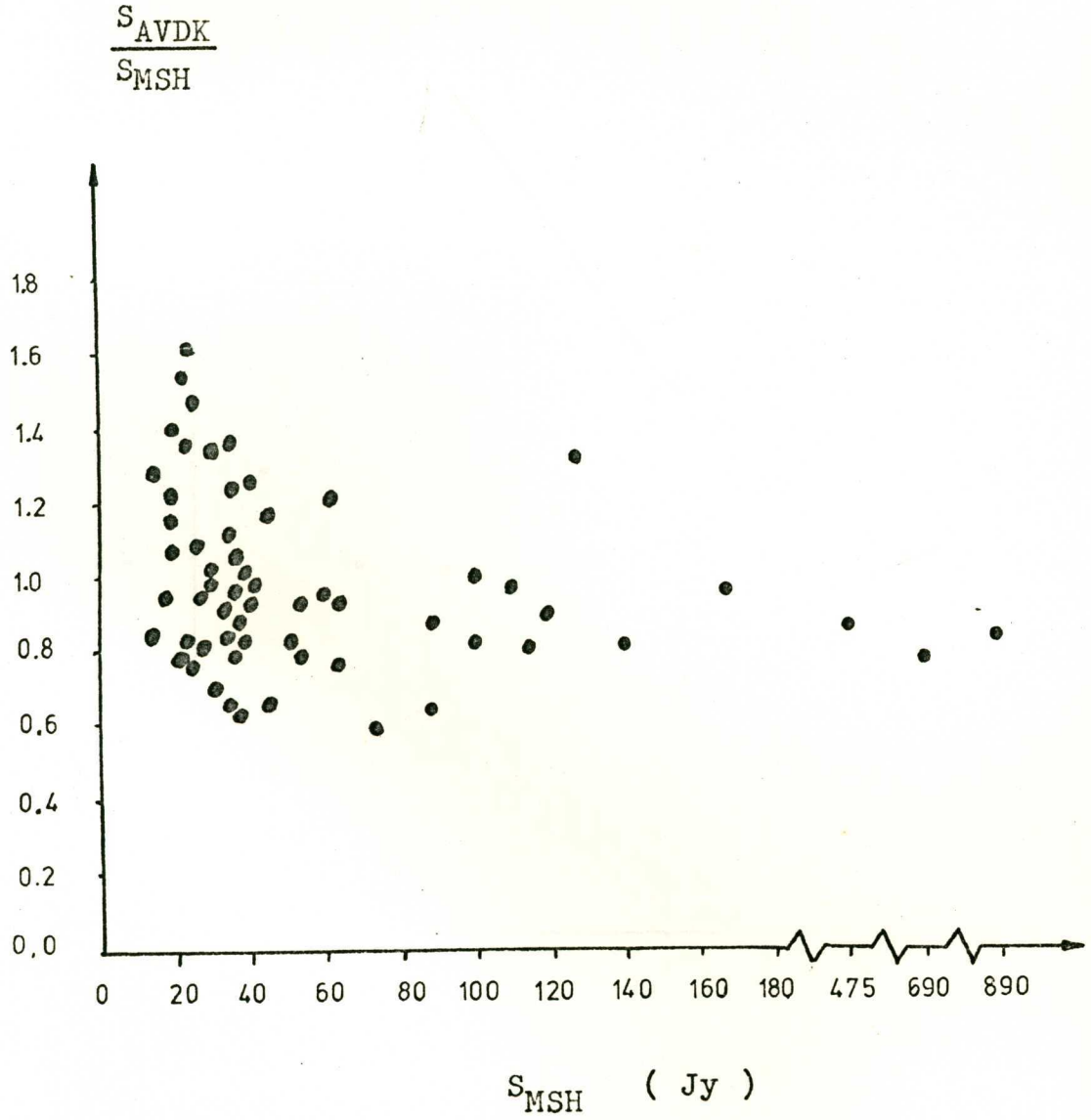

FIG. 8.3 . AVDK/MSH FLUX DENSITY RATIOS FOR MSH FLUX DENSITIES GREATER THAN 50 Jy PLOTTED AS A FUNCTION OF DECLINATION.

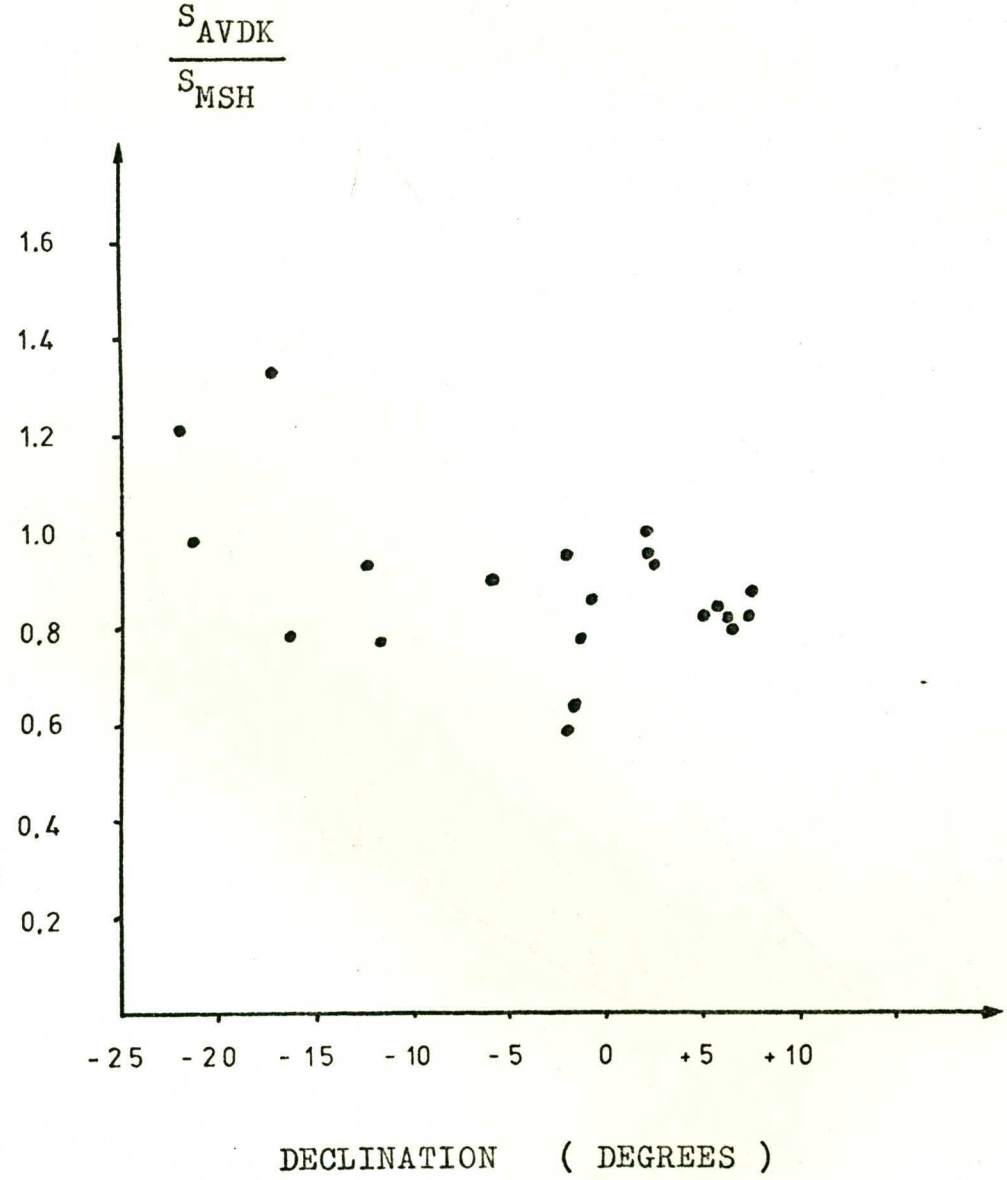

FIG. 8.4 . SPECTRA OF 0531+21, 0624-05 AND 1932-46 . THE MOLONGLO 111 MHZ MEASUREMENTS ARE INDICATED BY AN ARROW .

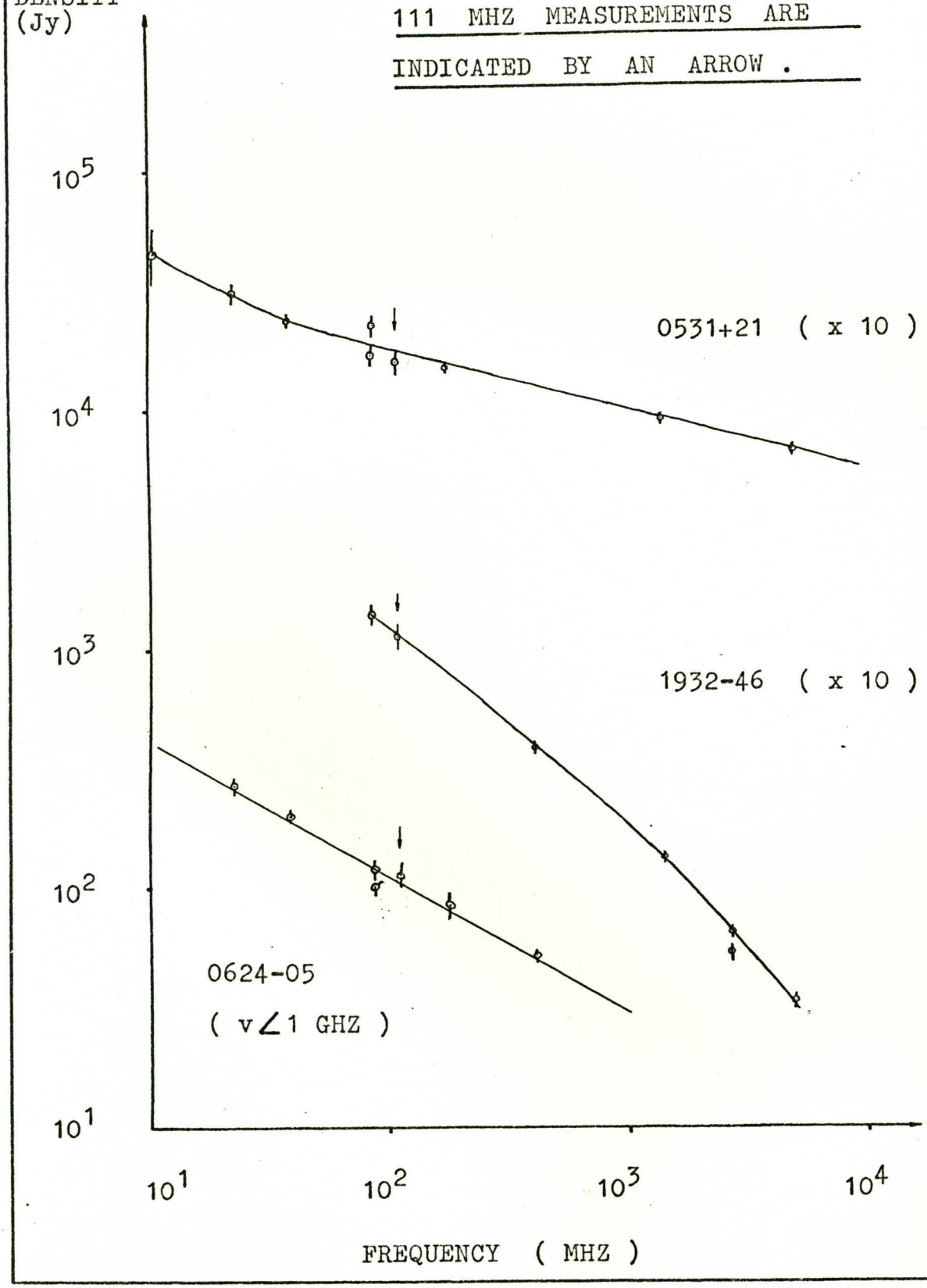

FIG. 8.5 . SPECTRA OF 0915-11 AND 1228+12 .

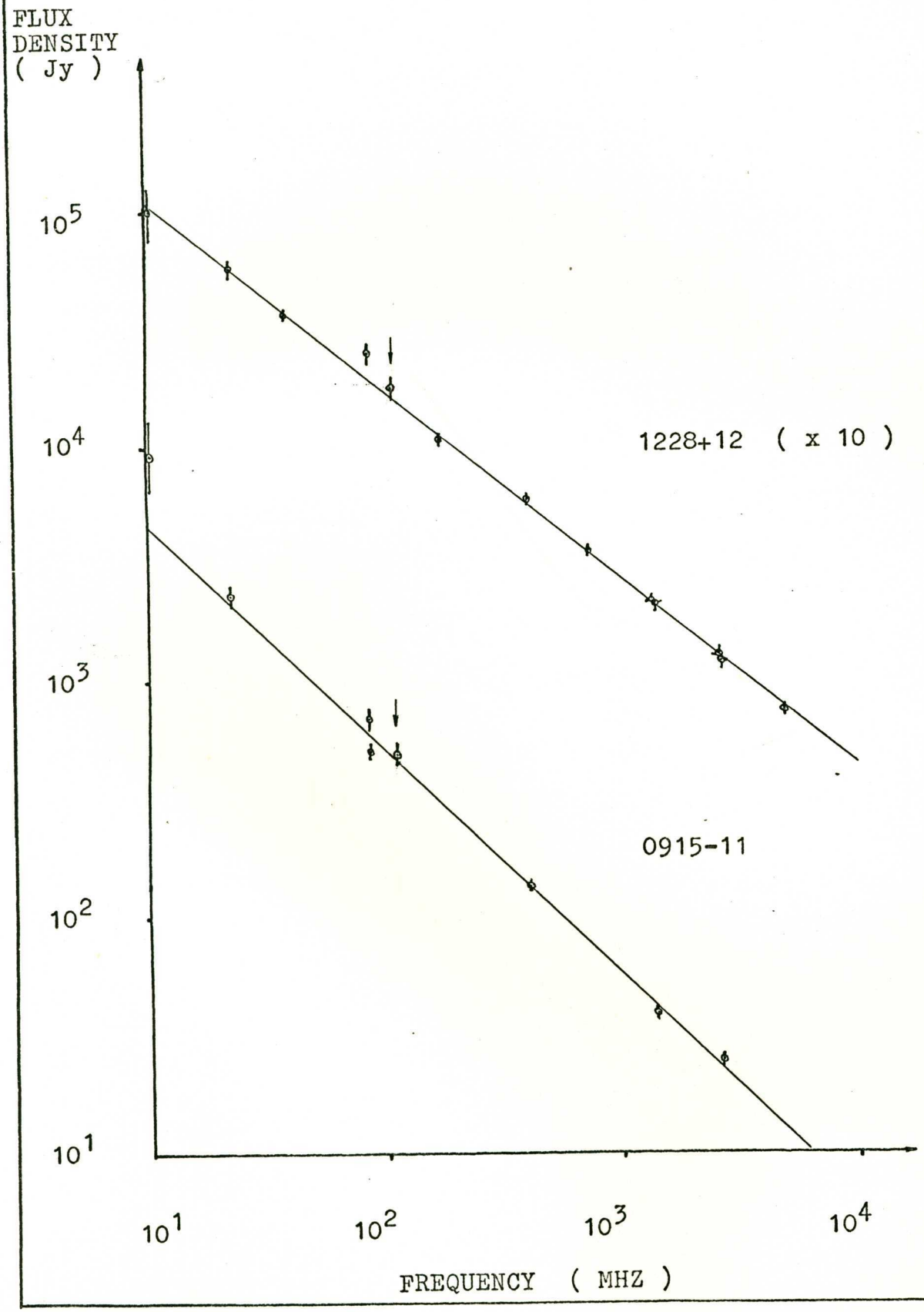

FIG. 8.6 . SPECTRA OF 1648+05 AND 2211-17 .

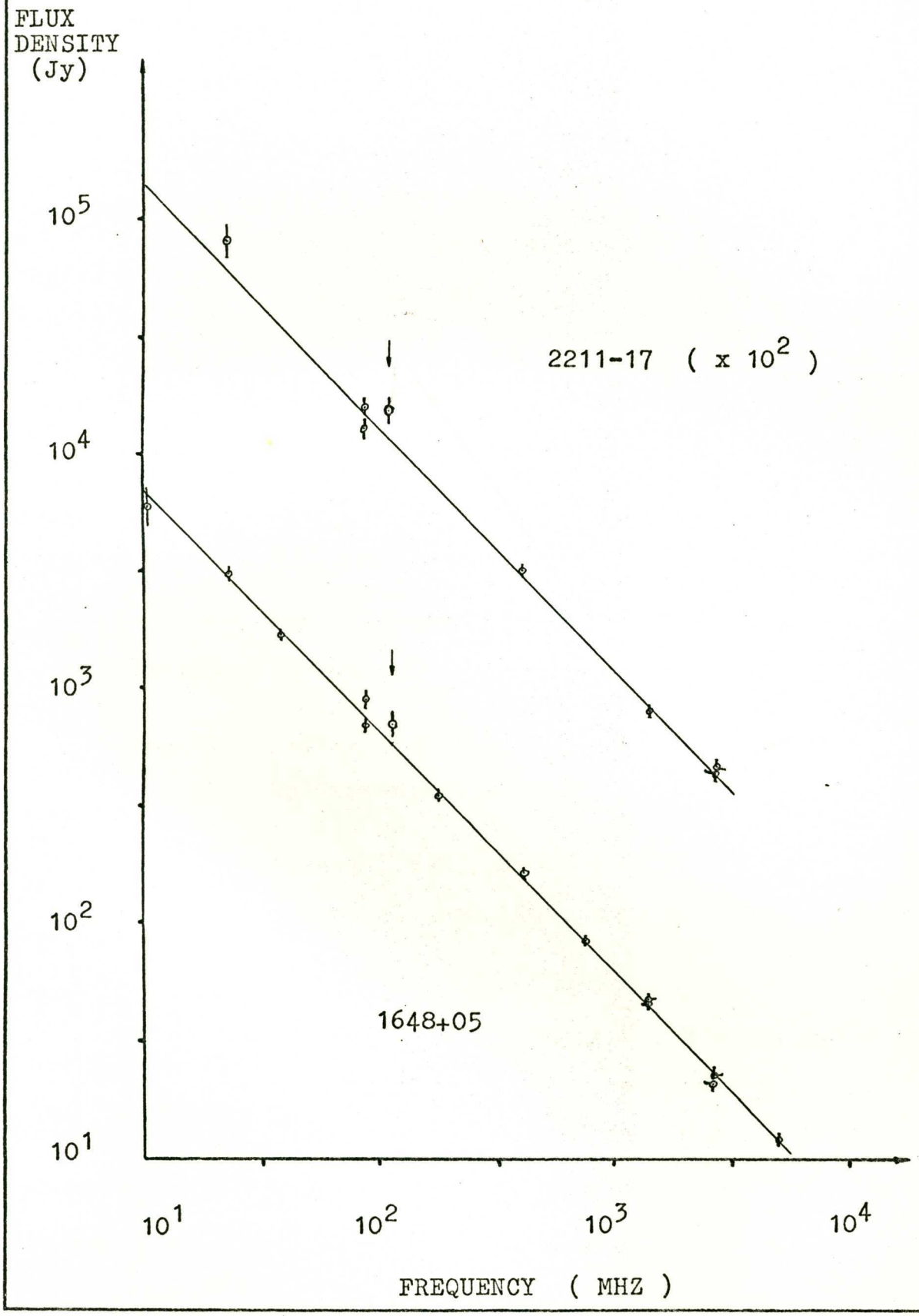

REFERENCES.

Artyukh, V.S., Vitkevich, V.V., and Dagkesamanskii, R.D. 1968. Soviet Astron. A.J. 11 , 792.

Artyukh, V.S., Vitkevich, V.V., Dagkesamanskii, R.D., and Kozhukhov, V.N. 1969. Soviet Astron. A.J. 12 , 567.

Baars, J.W.M., and Hartsuijker, A.P. 1972. Astron. and Astrophys. 17 , 172.

Bolton, J.G., Gardner, F.F., and Mackey, M.B. 1964. Aust.J.Phys. 17 , 340.

Born, M., and Wolf, E. 1964. "Principles of Optics". The Macmillan Company, New York.

Bracewell, R.N. 1965. "The Fourier Transform and its Applications". Mc.Graw-Hill, New York.

Braude, S.Ya., Lebedeva, O.M., Megn, A.V., Ryabov, B.P., and Zhouck, I.N. 1969a. Mon. Not. Roy. Astron. Soc. 143 , 289.

Braude, S.Ya., Lebedeva, O.M., Megn, A.V., Ryabov, B.P., and Zhouck, I.N. 1969c. Astrophys. Letters. 5 , 129.

Braude, S.Ya., Megn, A.V., Ryabov, B.P., and Zhouck, I.N. 1970. Astrophys. Space. Sci. 8 , 275.

Bridle, A.H., and Purton, C.R. 1968. Astron.J. 73 , 717.

Bridle, A.H., Davis, M.M., Fomalont, E.B., and Lequeux, J. 1972. Astron.J. 77 , 405.

Burgess, R.E. 1949. Wireless Engr. 26 , 133.

Cameron, M.J. 1971. Mon. Not. R. Astr. Soc. 152 , 439.

Christiansen, W.N., and Högbom, J.A. 1969. "Radiotelescopes". Cambridge University Press.

Clarke, M.E. 1965. Observatory. 85 , 67.

Collins, R.A. 1968. Ph.D. Thesis, Univ. of Cambridge., (result quoted by Scott and Shakeshaft 1971).

Condon, J.J., Niell, A.E., and Jauncey, D.L. 1971. Bull. Am. Astron. Soc. 3 , 23.

Conway, R.G., Kellermann, K.I., and Long, R.J. 1963. Mon. Not. R. Astron. Soc. 125 , 261.

Costain, C.H., Roger, R.S., and Lacey, J.D. 1969. I.E.E.E. Trans. Ant. Prop. AP-17 , 162.

Costain, C.H., Higgs, L.A., MacLeod, J.M., and Roger, R.S. 1976. Astron.J. 81 , 1.

Cottony, H.V., and Wilson, A.C. 1960. I.E.E.E. Trans. Ant. Prop. AP-8 , 144.

Croom, D.C. 1964. Proc. Instn. Electr. Engrs. III , 967.

Crowther, J.H., and Clarke, R.W. 1966. Mon. Not. R. Astr. Soc. 132 , 405.

Day, G.A., Shimmins, A.J., Ekers, R.D., and Cole, D.J. 1966. Aust.J.Phys. 19 , 35.

Ekers, R.D. 1969. Aust.J.Phys., Astrophys. Suppl., No.6.

Findlay, J.W. 1966. Ann. Rev. Astron. and Astrophys. 4 , 77.

FitzGerrel, R.G. 1965. I.E.E.E. Trans. Ant. Prop. AP-13 , 326.

Fomalont, E.B. 1971. Astron.J. 76 , 513.

Fomalont, E.B., and Moffet, A.T. 1971. Astron.J. 76 , 5.

Gower, J.F.R., Scott, P.F., and Wills, D. 1967. Mem. R. Astr. Soc. 71 , 49.

Hogg, D.C. 1959. J.App.Phys. 30 , 1417.

Howell, T.F., and Shakeshaft, J.R. 1967. J. atmos. terr. Phys. 29 , 1559.

Johnston, V.J. 1961. "Properties of Materials at Low Temperatures (Phase I)." Pergamon Press, London.

Jordan, E.C. 1950. "Electromagnetic Waves and Radiating Systems". Prentice-Hall, New York.

Kellermann, K.I. 1964a. Astron.J. 69 , 205.

Kellermann, K.I. 1964b. Ap.J. 140 , 969.

Kellermann, K.I., Pauliny-Toth, I.I.K., and Tyler, W.C. 1968. Astron.J. 73 , 298.

Kellermann, K.I., Pauliny-Toth, I.I.K., and Williams, P.J.S. 1969. Ap.J. 157 , 1.

Kraus, J.D. 1950. "Antennas". McGraw-Hill. New York.

Kraus, J.D. 1966. "Radio Astronomy". McGraw-Hill. New. York.

Little, A.G. 1958. Aust.J.Phys. 11 , 70.

Lockhardt, I. 1971. Ph.D. Thesis. Australian. National. Univ., (result quoted by Costain et al. 1976).

Maltby, P., and Moffet, A.T. 1962. Ap.J. Suppl. Ser. 7 , 141.

Mills, B.Y. 1953. Aust.J.Phys. 6 , 452.

Mills, B.Y., and Slee, O.B. 1957. Aust.J.Phys. 10 , 162.

Mills, B.Y., Slee, O.B., and Hill, E.R. 1958. Aust.J.Phys. 11 , 360.

Mills, B.Y., Slee, O.B., and Hill, E.R. 1960. Aust.J.Phys. 13 , 676.

Mills, B.Y., Slee, O.B., and Hill, E.R. 1961. Aust.J.Phys. 14 , 497.

Mills, B.Y., Aitchison, R.E., Little, A.G., and McAdam, W.B. 1963. Proc. I.R.E. (Aust). 24 , 156.

Munro, R.E.B., and Conway, R.G. 1972. Mon. Not. R. Astr. Soc. 159 , 21P.

Niell, A.E., and Jauncey, D.L. 1971. Bull. Am. Astr. Soc. 3 , 25.

Parker, E.A. 1968. Mon. Not. R. Astr. Soc. 138 , 393.

Pauliny-Toth, I.I.K., Wade, C.M., and Heeschen, D.S. 1966. Ap.J. Suppl. 13 , 65.

Pauliny-Toth, I.I.K., and Kellermann, K.I. 1968. Astron.J. 73 , 953.

Pilkington, J.D.H., and Scott, P.F. 1965. Mem. R. Astr. Soc. 69 , 183.

Price, R.M., and Milne, D.K. 1965. Aust.J.Phys. 18 , 329.

Rankin, R.A. 1949. Phil. Trans. R. Soc. A. 241 , 457.

Robertson, J.G. 1973. Aust.J.Phys. 26 , 403.

Roger, R.S., Costain, C.H., and Lacey, J.D. 1969. Astron.J. 74 , 366.

Roger, R.S., Bridle, A.H., and Costain, C.H. 1973. Astron.J. 78 , 1030.

Salomonovich, A.E., and Kuz'min, A.D. 1966. "Radioastronomical Methods of Antenna Measurement". Academic Press. New York.

Schelkunoff, S.A., and Friis, H.T. 1952. "Antennas : Theory and Practice". Wiley. New York.

Scott, P.F., and Shakeshaft, J.R. 1971. Mon. Not. R. Astr. Soc. 155 , 19P.

Shimmins, A.J., Day, G.A., Ekers, R.D., and Cole, D.J. 1966. Aust.J.Phys. 19 , 837.

Shimmins, A.J., and Day, G.A. 1968. Aust.J.Phys. 21 , 377.

Slee, O.B., and Higgins, C.S. 1973. Aust.J.Phys. Astrophys. Suppl. No. 27.

Slee, O.B., and Higgins, C.S. 1975. Aust.J.Phys. Astrophys. Suppl. No. 36.

Staff of Radiophysics Division, C.S.I.R.O. 1969. Aust.J.Phys. Astrophys. Suppl. No. 7.

Stelzried, C.T. 1965. I.E.E.E. Trans. Microwave Theory Tech. MTT-13 , 128.

Westman, H.P. 1968. "Reference Data for Radio Engineers". I.T.T. New York.

Williams, P.J.S., Dewhirst, D.W., and Leslie, P.R.R. 1961. Observatory. 81 , 64.

Williams, P.J.S., Kenderdine, S., and Baldwin, J.E. 1966. Mem. R. Astr. Soc. 70 , 53.

Wills, D., and Parker, E.A. 1966. Mon. Not. R. Astr. Soc. 131 , 503.

Wills, B.J. 1973. Ap.J. 180 , 335.

Wyllie, D.V. 1968. Ph.D. Thesis. Univ. of Sydney.

Wyllie, D.V. 1969a. Mon. Not. R. Astr. Soc. 142 , 229.

Wyllie, D.V. 1969b. Proc. Astr. Soc. Aust. 1 , 235.